FINAL REPORT

Development and Optimization of Targeted Nanoscale Iron Delivery Methods for Treatment of NAPL Source Zones

SERDP Project ER-1487

APRIL 2011

Linda Abriola
Andrea Ramsburg
Kurt Pennell
Tufts University

This document has been cleared for public release

SERDP
DOD ▪ EPA ▪ DOE

Report Documentation Page

1. REPORT DATE	2. REPORT TYPE	3. DATES COVERED
APR 2011	**N/A**	**-**

4. TITLE AND SUBTITLE	5a. CONTRACT NUMBER
Development and Optimization of Targeted Nanoscale Iron Delivery Methods for Treatment of NAPL Source Zones	5b. GRANT NUMBER
	5c. PROGRAM ELEMENT NUMBER

6. AUTHOR(S)	5d. PROJECT NUMBER
	5e. TASK NUMBER
	5f. WORK UNIT NUMBER

7. PERFORMING ORGANIZATION NAME(S) AND ADDRESS(ES)	8. PERFORMING ORGANIZATION REPORT NUMBER
Tufts University	

9. SPONSORING/MONITORING AGENCY NAME(S) AND ADDRESS(ES)	10. SPONSOR/MONITOR'S ACRONYM(S)
	11. SPONSOR/MONITOR'S REPORT NUMBER(S)

12. DISTRIBUTION/AVAILABILITY STATEMENT
Approved for public release, distribution unlimited

13. SUPPLEMENTARY NOTES
The original document contains color images.

14. ABSTRACT
This project was designed to develop and evaluate innovative nanoscale zero valent iron (nZVI) technologies for application to the treatment of dense nonaqueous phase liquid (DNAPL) source zones. An integrated research program, that combined multi-scale laboratory experiments with mathematical modeling, was undertaken: to investigate the transport and reactivity properties of commercially available nZVI systems; to develop and refine novel nZVI encapsulation formations with superior potential for source zone remediation; and to develop laboratoryvalidated mathematical models for prediction of the delivery and effectiveness of these nZVI systems for DNAPL source zone treatment. A number of processes were identified which will tend to limit the effectiveness of aqueous slurry nZVI injection for in situ DNAPL mass transformation, even under the most favorable conditions. These processes include pore clogging (and associated injection pressure increases), groundwater flow bypassing of the treated zone, DNAPL mobilization, unfavorable iron to DNAPL mass ratios, and reaction limitations due to dissolution mass transfer. Column transport experiments demonstrated the superior injection and mobility performance of biodegradable micro-emulsion nZVI formulations. However, reactivity studies suggest that emulsification will tend to slow aqueous phase reactions and to promote contaminant solubilization. Controlled emulsion partitioning to the NAPL may offer promise for sustained in situ reaction, but further research is needed to address reaction limitations due to low water solubility in the DNAPL. The trapping number concept and a model based upon modified clean bed filtration theory were successfully implemented to reproduce experimental observations of nZVI injection, transport, and reaction.

15. SUBJECT TERMS

16. SECURITY CLASSIFICATION OF:			17. LIMITATION OF ABSTRACT	18. NUMBER OF PAGES	19a. NAME OF RESPONSIBLE PERSON
a. REPORT **unclassified**	b. ABSTRACT **unclassified**	c. THIS PAGE **unclassified**	**SAR**	**132**	

Table of Contents

List of Figures

vii

List of Tables

List of Acronyms

1D	One Dimensional
BET	Brunauer-Emmett-Teller
BH	Borohydride
CFT	Clean Bed Filtration Theory
cis-DCE	cis-1,2-dichloroethene
CMC	Critical Micelle Concentration
CTRW	Continuous Time Random Walk
DLS	Dynamic Light Scattering
DLVO	Derjaguin-Landau-Verwey-Overbeek
DNAPL	Dense Non-aqueous Phase Liquid
FID	Flame Ionization Detector
GA	Gum Arabic
HLB	Hydrophobic Lipophilic Balance
IFT	Interfacial Tension
MISER	Michigan Soil-Vapor Extraction Remediation model
mRNIP	Modified Reactive Nanoscale Iron Particles
MTI	MTI Corporation - Nanoscale iron particles manufactured via PVD
NAPL	Non-aqueous Phase Liquid
nZVI	Nanoscale Zero Valent Iron
PCE	Tetrachloroethene
PVD	Plasma Vapor Deposition
RNIP	Reactive Nanoscale Iron Particles
SEM	Scanning Electron Microscopy
TCD	Thermal Conductivity Detector
TCE	Trichloroethene
TEI	Transformation Efficiency Index
VC	Vinyl Chloride
XRD	X-ray Diffraction
ZVI	Zero Valent Iron

Acknowledgements

Abstract

This project was designed to develop and evaluate innovative nanoscale zero valent iron (nZVI) technologies for application to the treatment of dense nonaqueous phase liquid (DNAPL) source zones. An integrated research program, that combined multi-scale laboratory experiments with mathematical modeling, was undertaken: to investigate the transport and reactivity properties of commercially available nZVI systems; to develop and refine novel nZVI encapsulation formations with superior potential for source zone remediation; and to develop laboratory-validated mathematical models for prediction of the delivery and effectiveness of these nZVI systems for DNAPL source zone treatment. A number of processes were identified which will tend to limit the effectiveness of aqueous slurry nZVI injection for *in situ* DNAPL mass transformation, even under the most favorable conditions. These processes include pore clogging (and associated injection pressure increases), groundwater flow bypassing of the treated zone, DNAPL mobilization, unfavorable iron to DNAPL mass ratios, and reaction limitations due to dissolution mass transfer. Column transport experiments demonstrated the superior injection and mobility performance of biodegradable micro-emulsion nZVI formulations. However, reactivity studies suggest that emulsification will tend to slow aqueous phase reactions and to promote contaminant solubilization. Controlled emulsion partitioning to the NAPL may offer promise for sustained *in situ* reaction, but further research is needed to address reaction limitations due to low water solubility in the DNAPL. The trapping number concept and a model based upon modified clean bed filtration theory were successfully implemented to reproduce experimental observations of nZVI injection, transport, and reaction.

Objectives

SERDP project ER-1487 integrated a combination of batch, column, and aquifer cell experiments with mathematical modeling to explore the application of novel zero valent iron (ZVI) delivery systems for effective treatment of dense nonaqueous phase liquid (DNAPL) source zones. The primary objective of this research was to develop and evaluate nanoscale ZVI systems that increase chloroethene destruction through targeted delivery to the DNAPL. In addition, transport and reaction behavior was assessed for these systems, leading to the development of application guidelines for optimizing nanoscale ZVI treatment of heterogeneous DNAPL source zones. These goals were accomplished by: (1) developing novel nanoscale ZVI encapsulation formations that increase chemical reactivity with chloroethene NAPLs while minimizing reactions with non-target compounds, (2) investigating the transport and reactivity of nanoscale ZVI using various delivery methods in natural porous media containing DNAPL, and (3) incorporating descriptions of nanoscale ZVI transport and reaction processes into a multiphase, multicomponent simulators for accurate prediction of ZVI delivery and reactivity within NAPL source zones. The research is intended to provide site managers and regulatory agency officials with a more complete and fundamental understanding of effective options for targeted treatment of NAPLs using nanoscale ZVI. Products of the research include: a) novel ZVI encapsulation formulations that directly target NAPLs for effective in situ destruction, b) an improved understanding of nanoscale ZVI transport and chemical reactivity in aquifer systems, c) a multiphase, multicomponent numerical simulation modules capable of predicting ZVI delivery, reactivity and effects on NAPL mobilization, and d) operational guidelines for treatment of NAPL source zones with nanoscale ZVI.

I. Background

Chloroethenes, such as trichloroethene (TCE) and tetrachloroethene (PCE), are commonly encountered groundwater contaminants at industrial facilities, dry cleaners, and military installations. The majority of chloroethene plumes emanate from aquifer formations contaminated by DNAPLs. These DNAPL source zones are often comprised of regions containing immobile NAPL ganglia and high-saturation pools overlying layers or lenses of low permeability media. Due to a combination of their low aqueous-phase solubility and limited mass transfer during dissolution, chloroethene NAPLs can persist in the subsurface for decades or centuries, thereby serving as long-term sources of groundwater contamination.

Although significant effort has been directed toward improving methods for recovering NAPL from the subsurface, it is now generally accepted that these remediation technologies (e.g., surfactant and cosolvent flushing) will not achieve complete mass removal and may, in fact, increase dissolved phase plume concentrations in the short term. Hence, treatment technologies that are capable of *in situ* mass destruction offer unique opportunities to effectively treat persistent NAPL source zone contamination. Although substantial advances have been realized in the area of NAPL bioremediation, even under ideal conditions enhancements in rates of contaminant mass transfer are anticipated to be less than a factor of 10. In contrast, abiotic chemical oxidants and reductants are characterized by relatively rapid reactions with dissolved phase DNAPL constituents, with the added benefit of minimal accumulation of toxic intermediates (e.g., vinyl chloride).

One promising chemical remediation technology involves the *in situ* application of nanoscale ZVI to treat DNAPL source zones. The conceptual basis for this approach is derived in large part from knowledge gained during the development and implementation of permeable reactive barrier walls for treatment of dissolved phase chloroethene plumes [e.g., *Matheson and Tratnyek*, 1994; *Orth and Gillham*, 1996; *Johnson et al.*, 1996; *Arnold and Roberts*, 2000]. Recent advances in the field of nanotechnology, however, provide the ability to control or tune ZVI particle sizes offering new possibilities for ZVI injection and transport within NAPL source zones [*Elliot and Zhang*, 2001]. Although the reaction of chlorinated ethenes with nanoscale iron has been the subject of a number of studies, few detailed investigations have been designed to elucidate and control mass transport during ZVI nanoparticle injection. The transport of ZVI nanoparticles, chemical reactivity, presence of NAPL, and application velocities and pressures render the mass transfer processes occurring during ZVI nanoparticle injection significantly different from those known to occur in permeable barriers.

Two strategies have been developed for ZVI delivery for treatment of NAPL source zones. The first process involves direct injection of a suspension of bimetallic nanoscale iron particles [*Elliot and Zhang*, 2001], while the second employs a liquid membrane to encapsulate the reactive ZVI [*Quinn et al.,* 2005]. Although direct injection of nanoscale iron particles can be accomplished through gravity feed, non-specific chemical reactions on the surface of the ZVI or Pd catalyst may result in inactivation of sites. Consumption of ZVI through the sorption of non-target solutes or dissolved minerals is a serious concern because ZVI particles are exposed to aqueous and solid-phase constituents throughout the injection and transport process [*Tratnyek et al.*, 2001; *Támara and Butler*, 2004; *Nurmi et al.*, 2005; *Köber et al.*, 2002; *Wilkin et al.*, 2003].

When ZVI is modified with Pd, common groundwater constituents such as sulfate, carbonate, and chloride may become less problematic than oxygen and nitrate, which quickly oxidize and inactivate reactive sites on the particle surface [*Schreier and Reinhard*, 1994; *Lowry and Reinhard*, 2000].

As the interest in treating contaminated groundwater with ZVI has increased, so too have the types of iron available for implementation. Most of the ZVI studies to date have been conducted with electrolytic iron powders or cast iron aggregates in the absence of a noble metal catalyst (i.e., unmodified ZVI). To reduce impurities, ZVI may be acid washed or reduced with molecular hydrogen prior to use, yet carbon based impurities (e.g., graphite) appear to facilitate sorption and possibly increase conversion of some chlorinated solvents [*Támara and Butler*, 2004; *Burris et al.*, 1998]. In addition, the surface pretreatments of micro- or nanoscale ZVI may influence the reaction pathway and rate [*Su and Puls*, 1999; *Li and Farrell*, 2000; *Ruiz et al.*, 2000; *Wang and Farrell*, 2003; *Lin and Lo*, 2005; *Nurmi et al.*, 2005]. There are a number of preparations which yield various particle sizes. Direct comparisons between preparation methods suggest ZVI particles produced (or subsequently treated) via reduction with molecular hydrogen (ZVI-H) may have superior sorption and reaction characteristics [*Lowry*, 2004; *Lin and Lo*, 2005; *Nurmi et al.*, 2005]. Faster contaminant degradation is contrasted against the potential for using smaller size fractions (produced from precipitation of the nanoparticles - ZVI-B) in the design of delivery vehicles for subsurface treatment [*Schrick et al.*, 2004]. While noble metal catalysts are more frequently used in conjunction with the ZVI-B particles to form bimetallic particles (ZVI-P), it is conceivable that similar treatments could be applied to ZVI produced through electrolytic or H2-based reduction [*Wang and Zhang*, 1997; *Lien and Zhang*, 2001].

The use of aqueous suspensions of ZVI nanoparticles relies upon contaminant mass transfer through the aqueous phase prior to contaminant transformation on the surface of the ZVI nanoparticle. In the case of bimetallic particles a hydrogen donor is also required. In this type of system NAPL constituents (e.g. chloroethenes) must (i) dissolve into the aqueous phase, (ii) transport to the nanoparticle surface, (iii) adsorb onto the nanoparticle surface, and (iv) undergo chemical reaction. The resulting degradation products must (v) desorb from the nanoparticle surface, and (vi) transport away from the nanoparticle surface. Any of these steps may control the overall rate of treatment. The ZVI nanoparticle residence time and relative rates of contaminant transport and reaction (i.e., Damkohler numbers) are therefore important design considerations. The addition of nonpolar or amphiphilic functional groups to ZVI nanoparticles enhances hydrophobicity and increases reaction specificity by increasing sorption selectivity [*Li et al.*, 1999; *Alessi and Li*, 2001; *Loraine*, 2001; *Zhang et al.*, 2002; *Lowry*, 2004]. These approaches may protect the iron particle from pacification reactions with inorganic solutes, but interactions with even limited amounts of natural organic matter may be problematic [*Tratneyk et al.*, 2001]. In addition, the presence of functionalized nanoparticles at the NAPL-water interface may have unintended consequences on NAPL mobility. Molecular and colloidal accumulation at fluid interfaces is known to reduce interfacial tension [*Adamson and Gast*, 1997; *Kralchevsky and Nagayama*, 2000; *Binks and Fletcher*, 2001]. In contrast, nanoparticle accumulation may act to mechanically stabilize the liquid-liquid interface [*Kralchevsky and Nagayama*, 2000; *Binks and Fletcher*, 2001]. Hence, the potential for NAPL mobilization and the potential for gravity plunging of nanoscale ZVI suspensions remain open questions that require further study.

An alternative delivery approach involves the use of a water-in-oil-inwater macroemulsion [*Quinn et al*., 2005]. These macroemulsions have been reported to have droplet diameters of approximately 10-15 µm, and reduce the likelihood of non-target reactions by necessitating solute diffusion through a liquid membrane system [*Geiger et al*. 2003; *Quinn et al*., 2005]. Increased reaction specificity has been shown to increase the overall degradation of TCE in batch systems [*Clausen et al*., 2002]. Introduction of the microscale or nanoscale iron into the macroemulsion, however, resulted in the formation of an extremely viscous fluid (~2000 cP) that required substantial injection pressures for subsurface delivery [*Quinn et al*., 2004; *Quinn et al.*, 2005]. Experience from field-scale injections in heterogeneous media suggests that non-uniform distribution of ZVI particles resulted from unstable flows (i.e., high viscosity fingering) [*Quinn et al*., 2004]. Injection of high viscosity fluids or coalescence of the emulsion and NAPL could also result in undesired mobilization of residual NAPL, based upon the total trapping number concept developed by *Pennell et al*. [1996].

Based upon the above discussion, the most critical issues that currently limit the advancement of nanoscale ZVI injection as an effective NAPL source zone treatment are: a lack of understanding of the processes that control transport of ZVI particles within a NAPL source zone; our inability to target NAPLs for treatment; and our limited knowledge of and ability to predict the processes controlling reaction rates *in situ*. Therefore, this research was designed to investigate the transport and delivery of ZVI nanoparticles in heterogeneous porous media containing DNAPL and to assess chemical reaction pathways and rates for ZVI particles in contact with chloroethene liquid phases.

II. Materials and Methods

The research plan was organized around four tasks: (1) Development, characterization and refinement of nanoscale iron delivery systems; (2) Transport and reaction of nanoscale iron in a representative porous medium; (3) Contaminant mass reduction in heterogeneous media; and (4) mathematical modeling of ZVI delivery and reactivity in NAPL source zones. Materials and methods associated with each Task are described below.

II.1. DEVELOPMENT, CHARACTERIZATION, AND REFINEMENT OF NANOSCALE IRON DELIVERY SYSTEMS

Evaluation of the kinetic stability of iron-in-oil suspensions is a necessary prerequisite for successful particle encapsulation. Suspension stability (iron particles within soybean oil) was analyzed by interpreting settling curves to determine the time to destabilization and the time-constant for sedimentation. These metrics provide a quantitative basis for selecting an iron-in-oil suspension to use in experiments related to encapsulation and transport.

II.1.1. Irons

RNIP is a commercially-available product of iron particles that are between 40 and 60 nm at the time of manufacturing [*Liu et al*., 2005]. These iron particles represent a Fe^0 core surrounded by an iron oxide (Fe_3O_4) shell, and are shipped as an aqueous slurry (pH between 10 - 12) having a solids content of approximately 26% wt. RNIP was dried for 24 hr at 105 ^{o}C under argon, and subsequently ground (using a mortar and pestle) to a fine powder prior to use in the reactors.

The specific surface area of the dried and ground iron particles was determined to be 11 m^2/g via N_2-BET analysis (Particle Technology Labs, Ltd.). Dried RNIP contained 26% Fe^0, with XRD spectra confirming the presence of Fe^0 and magnetite.

Nanoscale iron particles manufactured via plasma vapor deposition (PVD) under vacuum were acquired from MTI Corporation, Inc (MTI Corporation, Inc., 2009). The particles are shipped as a powder and are reported by the manufacturer to have an average particle size of 50 nm and a specific surface area of approximately 40 m^2/g. MTI iron particles were found to contain 90+ % Fe^0 (measured via H_2 production during HCl digestion). This high degree of purity is consistent with x-ray diffraction (XRD) spectra that suggest MTI iron particles are nearly pure Fe^0 and contain only small quantities of amorphous iron.

Borohydride reduced iron (referred to as BH) was synthesized by reducing an aqueous-phase ferrous iron with sodium borohydride to produce 30-40 nm size particles (following the procedures described by *Liu et al.* [2005]. Synthesized BH particles were dried for 24 hr at 105 ^{o}C under argon, and subsequently ground (using a mortar and pestle) to a fine powder prior to use in the reactors. The specific surface area of the dried and ground BH particles was determined to be 8 m^2/g via N_2-BET analysis (Particle Technology Labs, Ltd.). Dried BH particles contained 80% Fe^0, which is supported by XRD spectra that are indicative of Fe^0 and amorphous iron.

During the summer of 2008, Toda Americas Inc. announced that it would no longer supply small quantities of the commercial RNIP (current minimum order is a 55 gallon drum). To address this issue in the short term, Dr. Greg Lowry (Carnegie Mellon University, SERDP Project 1491) graciously provided an additional small quantity of RNIP (100 mL) to complete ongoing experiments. In addition, we initiated a program to synthesize different types of nZVI including bimetallic (Pd and Ni) nanoscale iron particles, with the intent of enhancing reactivity with the PCE-DNAPL. Previous studies have reported that the chlorinated ethenes (20 mg/L) were completely reduced within 90 min with a Pd/Fe bimetallic metal loading of 5 g per liter (*Lien and Zhang*, 2001). Ethene was the primary product from these reactions, accounting for 60-90% of the total carbon mass. These materials were subsequently evaluated in batch reactor experiments and in column reactivity studies.

Z-Loy is a commercially available iron product that contains Fe^0 supported on an aluminum ceramic core. The manufacturer (On Materials, LLC) suggests that the median size of Z-Loy particles is 200 nm, and the surface area is 15 m^2/g. Z-Loy comprises a two part system (i) particles shipped in glycol and (ii) a proprietary dispersant. Due to the non-aqueous nature of the product, aggregation is limited (improves subsurface mobility) and more reactive metal compositions may be used on the surface (little to no toxic daughter products are produced). While not necessary, Z-Loy suspensions were prepared under argon. Use of argon establishes a uniform procedure for working with the iron particles and ensures Z-Loy reactivity remains high by avoiding exposure to oxygen. Analysis suggests that of the iron present on the Z-Loy particles, approximately 33% is ZVI.

II.1.2. Chemicals

Soybean oil (MP Biomedicals, LLC) was used as the non-polar phase in all emulsions. At 20 ^{o}C this soybean oil has a density of 0.9 g/mL and viscosity (at 20 sec^{-1}) of 60 mPa·s. Ferrous sulfate

(FeSO$_4$·7H2O), hydrochloric acid (HCl) (37%), sodium hydroxide (NaOH), methanol (99.9%), oleic acid and trichloroethylene (TCE) (99.9%) were supplied by Fischer Scientific. Sodium borohydride (NaBH4) (98+%) and Gum Arabic were supplied by Acros Organics. Purified water (resistivity > 18.2 mΩ/cm and total organic carbon (TOC) <10 ppb) was obtained from a MilliQ Gradient A-10 station (Millipore Inc.). Tween 20 (polyoxyethylene (20) sorbitan monolaurate) and Span 80 (sorbitan monooleate) were obtained from Fisher Scientific, Inc. and Ruger Chemical Co., Inc., respectively. Tween 20 (HLB of 16.7) and Span 80 (HLB of 4.3) are non-ionic, food-grade, readily degradable surfactants that have a synergistic emulsifying relationship [*Ramsburg et al.*, 2003]. Pluronic® F108 (methyl-oxirane polymer with oxirane) was obtained from BASF. Pluronic® F108 (HLB of >24) is a difunctional block copolymer surfactant commonly used in cosmetic and pharmaceutical applications. Aerosol MA-80I (sodium di(1,3-dimethylbuyl) sulfosuccinate) and Aerosol OT (sodium di(2-ethylhexyl) sulfosuccinate) are anionic surfactants obtained from Cytec Industries and Fisher Scientific, Inc., respectively. Aerosol MA-80I (MA) consists of 80% active ingredient (with the balance comprised mainly of water and 2-propanol). Aerosol OT (AOT) is more hydrophobic (water solubility is 15 g/L) than Aerosol MA (water solubility is 343 g/L). Oleic acid (OA) (Fisher Scientific, Inc.) and is an oil-soluble surfactant having an HLB of 1.

II.1.3. Reactivity Screening

II.1.3.1. RNIP and Synthesized Bimetallic Nano Iron in Aqueous Phase

To compare the reactivity of different nZVI materials, a series of batch reactor experiments was conducted at a nominal aqueous phase PCE concentration of 75 mg/L in 10 mM bicarbonate with HEPES (4-(2-hydroxyethyl)-1-piperazineethanesulfonic acid) buffer addition to adjust the pH of the solution to ~ pH 7.7. Unmodified RNIP from Toda Americas was prepared by adding 40 mL of RNIP in 1L of degassed deionized water to obtain a 10 g/L RNIP suspension. The batch reactors were gently mixed on a shaker table at 100 rpm for 2 days. The aqueous phase concentration of PCE and anticipated reaction products such as vinyl chloride were analyzed using a Model 6890 Hewlett-Packard gas chromatograph (GC) equipped with a Tekmar® HT3 headspace autosampler (Teledyne Technologies, Inc.) and a 30 m long by 0.25 mm outside diameter (OD) DB-5 column (Agilent) with 0.25 µm film thickness connected to a flame ionization detector (FID).

II.1.3.2. MTI Iron in Aqueous Phase

For MTI iron, batch experiments were performed in 120 mL serum bottles capped by Teflon Mininert valves. All reactors were prepared in an anaerobic glove box so the reactor headspace was filled with argon. All experiments contained excess iron (0.05 g). 50 mL of TCE solution at an initial concentration of 100 mg/L was added to each reactor. The aqueous phase was buffered using 0.1 M HEPES buffer (pK$_a$ = 7.66) to maintain a pH of 7. A total of 11 batch reactors were set up, including two control experiments, one containing iron suspended in 50 mL of Milli-Q water and another containing 50 mL of the 100 mg/L TCE solution in the absence of MTI iron. The reactors were mixed by end-over-end rotation at 30 rpm (T = 20°C).

Destructive sampling of each reactor was performed at selected intervals. At each sampling interval the headspace pressure was determined using a Digital Test Gauge purchased from Crystal Engineering Corporation. 0.4 mL of headspace sample was withdrawn from the reactors

using a gas syringe and this was analyzed for hydrogen, TCE, and TCE reduced products (see below).

II.1.3.3. Z-Loy Iron in Aqueous Phase

For Z-Loy, batch reactor experiments were performed in 120 mL serum bottles capped by Teflon Mininert valves. These reactors were constructed in an argon filled glove box to maintain anoxic conditions. 70 mL of 500 mg/l TCE aqueous solution were added to each reactor, leaving 50 ml of argon-filled headspace. Then, the appropriate amounts of Z-Loy slurry and a dispersant provided by OnMaterials (which contains a hydrogenation catalyst) were added to each reactor to yield a final Z-Loy suspension concentration of 5 mg/L. The batch reactions conducted in this experiment contained excess TCE, which is then able to use all available iron in the system. For each experiment, one batch reactor was created as described above, as well as two control reactors, one with TCE and no Z-Loy suspension, and one with Z-Loy suspension and no TCE.

Headspace pressure within each reactor was measured using a Digital Test Gauge purchased from Crystal Engineering Corporation. After pressure measurements, 0.4 mL headspace samples were taken for each reactor using a gastight syringe and analyzed via GC. The reactors were then placed on an end over end rotator at 30 rpm until the next sample was taken. Destructive sampling then ensued at 30 minute intervals at the start of the experiment, and then increased after the first two hours.

Details of the analytical methods employed for TCE and degradation product analysis in both MTI reactivity experiments may be found in *Crocker et al*. [2008], *Berge and Ramsburg* [2009], and *Berge and Ramsburg* [2010]. In brief, concentrations were quantified using headspace analyses and a gas chromatograph equipped with either/both flame ionization detector (FID) and thermal conductivity detector (TCD). Where multiple detectors were employed, the sample path was split to two columns: an HP-MOLSIV (30m length, 0.53mm inner diameter, 50µm film thickness) leading to the TCD, and an HP-PLOTQ (30m length, 0.53mm inner diameter, 40µm film thickness) leading to the FID. Instruments were calibrated on each day of use with a minimum of a five-point standard curve. Specifically for Z-Loy reactivity, a modified version of the ferrozine method was developed (fully described in *Viollier et al*. [2000]). The modified method was designed for measuring the total Fe concentration of filtered Z-Loy samples digested in concentrated (12N) hydrochloric acid. Ferrozine forms very strong complexes with iron ions which have a purple color. The digested Z-Loy samples, once undergoing the ferrozine process, were analyzed by UV/Vis at a wavelength of 562nm.

II.1.4. Emulsion Formulation and Property Characterization

II.1.4.1. Emulsion Formulation

Details of the design, formulation and construction of all surfactant stabilized emulsions can be found in *Crocker et al*. [2008], and Berge and Ramsburg [2009]. In brief, phase inversion techniques were employed under constant mixing (5,000 rpm, GLH high-shear homogenizer, Omni, Inc.). Temperature during emulsification was maintained between 20 ^{o}C and 30 ^{o}C. A phase inversion procedure was employed because it has been documented to produce emulsions with smaller droplets (at lower energies) and consequently greater kinetic stability than is typically achieved using other emulsification techniques [e.g., *Fernandez et al*., 2004]. The

continuous-phase of all emulsions produced using this procedure consisted of Milli-Q water and water soluble surfactant. The dispersed-phase comprised oil, and often, oil-soluble surfactant + RNIP particles. Surfactant concentrations were selected to maintain emulsion HLB between 12 and 15; a range documented to be suitable to promote stability of oil-in-water emulsions [*Becher*, 2001].

Gum Arabic stabilized emulsions 20g of $FeSO_4 \cdot 7H_2O$ were dissolved in 1 liter of 30% (v) methanol solution by stirring with stand-mixer under 400 rpm (Ika RW-20). Then 10 mL of 5 N NaOH solution was added drop wise to the continuously stirred (400 rpm) ferrous solution to adjust the pH to 10. 6 g of $NaBH_4$ was dissolved in 50ml water, and was added at a rate of 2 drops per second (from a 250 mL separatory funnel) to the ferrous solution which was vigorously mixed (600 rpm). After adding all the $NaBH_4$ solution, mixing continued for 20 minutes to facilitate the reaction and liberation of hydrogen gas. The suspension was allowed to settle before decanting the majority of the aqueous phase. The remaining iron containing liquid was centrifuged in a Beckman-Coulter Avanti J-25 centrifuge at 6000 rpm for 10 min at a temperature of 22 deg C. The subsequent supernatant was discarded yielding an iron paste. A sample of the iron paste was dried under N_2 for 12 hr at 120^oC to determine the iron content in the paste.

Oleic acid is commonly employed to stabilize ferro-fluids and used here to suspend the iron for transfer to the soybean oil [e.g., *Bashtovoy and Berkovsky*, 1987]. 10 mL of oleic acid was added to the iron paste obtained from the synthesis and vortexed for 1 min (Fisher Vortex Genie 2). The iron-containing oleic acid was subsequently added to 40 mL of soybean oil, the major components of which are lioleic acid (53% wt) and oleic acid (23% wt) [*Gunstone*, 2004], and was sonicated with an ultrasonic dismembrator (Fisher Scientific Model 500) for 1.5 min at 100% output (400W) to evenly disperse the nZVI particles in oil. The resulting iron containing oil (subsequently referred to as iron oil) was subsequently mixed with 160 g water and 200 g of 20% GA solution, and blended at room temperature for 6 minutes with a homogenizer (Omni International General Lab Homogenizer) at maximum output (700W). The 20% GA solution was prepared by dissolving GA powder in water under mild stirring (~120 rpm) over night, to ensure GA was fully hydrated.

II.1.4.2. Physical Property Measurement

Densities were measured at room temperature (22±2 deg C) using 25 mL glass pycnometers that were calibrated with MilliQ water prior to each use. Viscosity was measured of a range of shear rates (0.4-100 s^{-1}) using an AR-G2 rheometer (TA Instruments) with a stainless steel concentric cylinder geometry. Interfacial tension (IFT) between emulsion and TCE was quantified after 60 sec of contact using a drop shape analyzer (IT-Concept., Inc.). Bright field microscope pictures were taken with a Zeiss Axiovert S100 inverted microscope equipped with a 32x objective to confirm the droplet size and morphology.

II.1.4.3. Iron Analysis

For the surfactant stabilized emulsion, iron particles contained within the oil droplets were magnetically extracted after solubilizing emulsion samples in acetone. Iron particles were subsequently removed and digested in concentrated (12 N) hydrochloric acid for 24 hr prior to quantification of iron concentration via flame atomic adsorption (Solar Thermo AA,

ThermoFisher, Inc.). GA stabilized emulsion was directly digested and analyzed. ZVI content of the total iron was assessed by measuring the hydrogen concentration in the headspace of the batch reactors used for acid digestion with gas chromatography. Analytical methods are described below.

II.1.4.4. Emulsion Stability

Emulsion stability was evaluated using a traditional phase separation technique (a.k.a. time to first visible coalescence) in which approximately 10 mL of emulsion were placed in undisturbed graduated vessels and visually observed over time for physical changes (i.e., iron settling, creaming). Droplet size distributions were obtained by imaging with light microscopy or cryogenic scanning electron microscopy (SEM) and subsequent image analysis using Metamorph software (Molecular Devices v. 7.0, Inc.). A Zeiss inverted microscope with a Sony digital camera (0.43 megapixel) was used to acquire 9 images for each sample (triplicate imaging of triplicate subsamples). Cryogenic SEM (Zeiss, Supra55VP) was employed to explore emulsion droplet sizes that may be below detection using the light microscope. Samples were prepared for SEM analysis by freezing the sample in liquid nitrogen prior to slicing and gold plating in a vacuum chamber (10^{-6} torr and -188 ^{o}C). Droplet size distributions obtained via the light microscopy procedure which had a detection limit of 0.96 μm (due to the limited sensitivity of the camera). In addition, droplet size distributions at 1000x dilution were quantified via dynamic light scattering (DLS) using a Zetasizer NanoZS analyzer (Malvern). Dynamic light scattering measurements were accomplished at 633nm, 173 deg. Zeta potential was measured with laser Doppler velocimetry (LDV) at 1000x dilution using the same Zetasizer NanoZS analyzer.

II.1.4.5. Emulsion Reactivity Screening

Emulsion (~40 g) was added to a series of 120 mL glass serum bottles inside an argon filled glove box. All batch experiments were performed in triplicate with iron controls constructed using the blank emulsion. Subsequent to the addition of ~15 mmol of TCE (save TCE control systems) reactors were sealed and rotated on LabQuake end-to-end shakers at 8 RPM. Headspace gas in the reactors were sampled successively, and analyzed for hydrogen, TCE, acetylene, ethene, and ethane. Phases were assumed to be in equilibrium given the large surface area represented by the emulsion droplets, and the rapid partitioning reported for completely mixed reactors [*Gossett*, 1987]. Observed degradation rates were adjusted for the presence of headspace.

II.2.TRANSPORT AND REACTION OF NANOSCALE IRON IN A REPRESENTATIVE POROUS MEDIUM

II.2.1. Evaluation of the Transport of Nanoscale Iron Delivery Systems

One objective of this task was to quantify the transport of nanoscale iron delivery systems in water-saturated porous media. Reactive Nanoscale Iron Particles (RNIP) were obtained from Toda American Inc. (Schaumberg, IL), and served as the baseline material for comparison to the other delivery systems being developed in Task 1, and for validation of transport models developed in Task 4. One-dimensional flow experiments were conducted in glass columns packed with 20-30 mesh Ottawa and Federal Fine sand (U.S. Silica Co.) to determine the number

of pore volumes required for iron to elute from the water-saturated columns (i.e., breakthrough) and the distribution of iron retained within the packed bed.

II.2.1.1. Column Experiments for RNIP Transport

Four experiments were performed to determine the distance RNIP would travel in water-saturated columns as a function of flow rate and grain diameter. The experimental system, shown in Fig. II-1, consisted of a 2 L carboy containing 2 g/L RNIP suspension that was continuously sparged with nitrogen gas at a flow rate of 1 L/min to keep the suspension well mixed and oxygen free. A 2 g/L RNIP suspension, which also contained 4 mM of calcium chloride and 11 mM of sodium carbonate as background electrolytes, was then passed through a custom-made glass enclosure that contained a half-inch diameter sonifier probe operated at 45 W (i.e., sonifier cell). The purpose of the sonication was to break apart the RNIP particles, which rapidly aggregate in aqueous solution. After passing through the sonifier cell, the solution entered a peristaltic pump head that controlled the delivery rate of the suspension. The iron particle suspension was then introduced into the packed column (2.5 cm inside diameter and 15 cm in length), and the column effluent was collected continuously in 8 mL glass vials. The mass of each vial was monitored along with the vial collection time, and was used to compute the average flow rate during the experiment. The iron content of each vial was determined using the Ferrozine method after dissolving the iron particles with 0.5 mL of 12.1 N HCl. Three column experiments were completed with 20-30 mesh Ottawa sand (mean grain diameter of 0.6 mm), and one experiment was completed with Federal Fine sand (30-140 mesh, mean grain diameter of 0.31 mm).

Preparing and delivering an iron particle suspension at a constant concentration was found to be challenging. Two delivery systems, designed to a) constrain the mass delivered or b) create well-mixed suspensions were evaluated and used in all subsequent experiments. The first method consisted of introducing 60 mL volumes of RNIP solution dispensed from separate syringes to constrain the mass of iron delivered, while the second method uses an impeller stirring system along with a Morten flask to generate turbulent mixing conditions in the stock solution.

An additional set of column experiments was performed to evaluate RNIP transport and bank formation at higher mass loadings. These experiments involved introducing high-concentration RNIP suspensions (e.g., 10 to 100 g/L) into water-saturated, sand-filled columns to determine the time required for RNIP breakthrough as well as the concentration of iron eluting from and retained within the columns. In addition to iron movement, the hydrostatic pressure required to drive the RNIP bank through the sand filled column was determined. The high-concentration experiments were performed to determine the critical RNIP concentration required for bank formation and to determine if the rate of bank movement was proportional to the rate of RNIP addition. The experiments on RNIP delivery and reactivity involved creating a column with residual PCE saturation and then introducing RNIP at 10 g/L, while monitoring the column effluent for PCE and reaction products.

The column experiments were performed using an unmodified RNIP suspension obtained from Toda America, with a reported concentration of 26 weight percent or 260 g/L (Lot no. 70601). RNIP suspensions with nominal concentrations of 10, 50 and 100 g/L were prepared by

transferring 40, 200, and 400 mL, respectively, of the 260 g/L Toda RNIP suspension into de-aired and de-ionized (DI) water containing 3.5 mM of calcium chloride in a 1 L Morton flask. The contents of the Morton flask was stirred with an impeller rotating at 200 revolutions per minute and the stirred suspension was then transferred to the column inlet using a peristaltic pump through sixteenth inch inner diameter Teflon tubing.
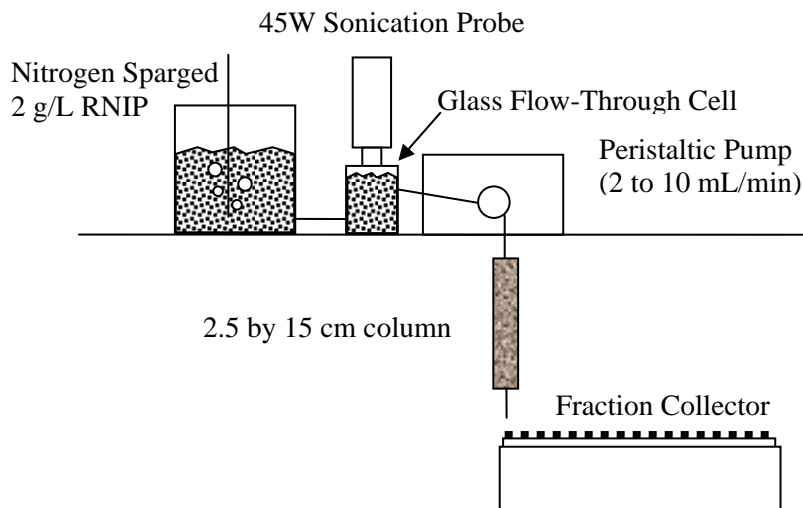
Figure II-1. Schematic diagram of the RNIP transport experimental setup

II.2.1.2. Column Experiments for Modified RNIP Transport

In an effort to address the aggregation and relatively poor transport properties of RNIP in porous media, Toda America developed a polymer-modified Reactive Nanoscale Iron Particles (mRNIP). This product is purported to form stable aqueous suspensions, in which the iron particles do not aggregate or precipitate due to gravity settling. A freshly-prepared batch of mRNIP was obtained from Toda America, from which we prepared a 2 g/L suspension that also contained 4 mM of calcium chloride as a background electrolyte. The mRNIP solution was then introduced into a water-saturated 20-30 mesh Ottawa sand column at a flow of 2 mL/min without use of sonication.

In addition to the polymer-modified RNIP experiments, a series of experiments was performed to evaluate the use of a nonionic surfactant, Tween80, to enhance RNIP suspension stability and transport. The delivery suspension was prepared by adding 1 g of Tween 80 (Uniqema, Wilmington, DE) to 1 L of a 4 mM aqueous calcium chloride solution, followed by the addition of 10 mL of 26% Toda RNIP to create a 2 g/L iron suspension. The RNIP-Tween80 suspension was delivered to a water-saturated 20-30 mesh Ottawa sand column at a flow of 2 mL/min without sonication.

II.2.1.3. Column Experiments for Z-Loy Transport

The transport of Z-Loy was evaluated in a series of column experiments. Details may be found in *Crocker et al.* [2008], and *Berge and Ramsburg* [2009]. In brief, Kontes borosilicate glass

columns were dry packed with Ottawa Sands to an approximate packed length (usually 10 cm). Methods for column preparation and packing may be found in *Pennell et al.* [1993]. Effective velocity and dispersion in the porous medium were quantified using a non-reactive, conservative tracer test. For columns containing DNAPL, the organic phase was dyed with 1 x 10⁻⁴M Oil-Red-O for visualization purposes and entrapped within the column (see *Pennell et al.* [1993] for detailed methods). A second non-reactive, conservative tracer test was conducted prior to commencing emulsion droplet or iron particle transport experiments. Effluent samples were periodically collected using an autosampler (ISCO Retriever II) and quantified for density, emulsion or iron content, and effluent TCE and degradation product concentrations.

Experiments commenced by introducing 4-5 pore volumes of Z-Loy (1% wt solids) to a column packed with Ottawa 20-30 mesh sand. Flow into the column was established using a Mariotte bottle in which the Z-Loy was maintained under a blanket of argon to reduce the consumption of reduced iron by dissolved oxygen. Experiments were conducted at two flow rates: 1 mL/min (Darcy velocity = 0.06 cm/min) and 8 mL/min (Darcy velocity = 0.44 cm/min). Throughout the experiment, effluent samples were collected using a fraction collector (ISCO Retriever II). Subsequent to determination of density, samples were digested in concentrated hydrochloric acid for quantification of the total iron content. Total iron was quantified using either a modified ferrozine method (Experiment A, based on *Voillier et al.* [2000]), or Atomic Absorption spectroscopy (Experiment B).

II.2.2. Potential for NAPL Mobilization during Iron Delivery

The delivery of nanoscale iron suspensions has the potential to mobilize and redistribute entrapped NAPLs from the pore space. A number of factors will determine this potential for mobilization, including (a) the density of the displacing fluid (i.e., a difference between the nanoscale iron suspension(displacing fluid) and the resident pore fluid density), (b) the viscosity of the displacing fluid (e.g., increased viscosity of emulsion-based delivery suspensions), (c) the interfacial tension with the entrapped NAPL (e.g., interfacial tension reduction due to presence of stabilization agents and surfactant-based emulsions), and (d) the (high) flow rates that are often employed to deliver nanoscale iron suspensions. Theoretical analyses and experimental studies were conducted to assess the potential for mobilization of PCE-DNAPL during delivery of nanoscale iron suspensions.

II.2.2.1 Trapping Number Analysis

Theoretical analysis of the potential to mobilize entrapped (residual) NAPL was performed using the trapping number (N_T) approach [*Pennell et al.*, 1996]. Here, the onset and extent of DNAPL mobilization is accounted for by considering the forces acting upon an entrapped NAPL droplet, which is described by the total trapping number as:

$$N_T = \sqrt{N_{Ca}^2 + 2N_{Ca}N_B \sin \alpha + N_B^2} \tag{1}$$

where α is the angle of aqueous-phase flow relative to the horizontal axis. The capillary (N_{Ca}) and Bond (N_B) numbers are defined as:

$$N_{Ca} = \frac{q_w \mu_w}{\sigma_{ow} \cos \theta}, \quad N_B = \frac{\Delta \rho g k k_{rw}}{\sigma_{ow} \cos \theta} \tag{2}$$

where q_w is the Darcy velocity of the aqueous phase (upward direction is taken as positive), μ_w is the dynamic viscosity of the aqueous phase, σ_{ow} is the interfacial tension between the organic and aqueous phases, θ is the contact angle between the aqueous and solid phases, $\Delta \rho$ is the difference between the aqueous and organic phase densities ($\rho_w - \rho_o$), g is the gravitational constant, k is the intrinsic permeability of the porous medium, and k_{rw} is the relative permeability of the aqueous phase. For the case of horizontal flow (α = 0º), Eq. 1 reduces to:

$$N_T = \sqrt{N_{Ca}^2 + N_B^2} \tag{3}$$

Results of prior column studies conducted with PCE-NAPL suggest that the threshold trapping number corresponding to the onset of ganglia mobilization is approximately 2 x 10^{-5}, with nearly complete displacement observed at N_T values exceeding 1 x 10^{-3} [*Pennell et al.*, 1996].

II.2.2.2 RNIP Delivery

A series of 1D column studies was conducted to evaluate the displacement of residual (entrapped) PCE-DNAPL during RNIP delivery. The experiments were performed in 15-cm long Kontes® (Kimble-Chase, Vineland, NJ) borosilicate glass columns with an inside diameter of 2.5 cm, and equipped with high density polyethylene end plates. To minimize any impediment to the flow of RNIP or PCE-DNAPL entering and leaving the column, mesh screens were placed in the end plate, and the end plate inlets were machined to yield an inside diameter of 1/8 inch. The columns were orientated vertically, and packed with 20-30 mesh Ottawa sand (U.S. Silica, Berkeley Springs, WV) in 1-cm increments under gentle vibration. Following dry packing, the column was saturated with CO_2 gas for 15 minutes at a flow rate of 50 mL/min to facilitate dissolution of any entrapped gas during water saturation process. De-aired, DI water containing 3.5 mM of calcium chloride was then introduced into the column using a Masterflex peristaltic pump (Cole-Parmer, Vernon Hills, IL) operated in an up-flow mode at a rate of 2 mL/min until the column was completely saturated with water. The aqueous pore volume (PV), determined from the difference in column weight before and after water saturation, ranged from 28-29 mL. Residual PCE-DNAPL was emplaced by injecting approximately 25 mL of PCE-DNAPL, which was dyed with Oil-Red-O dye to facilitate visual observations, through the bottom (up flow mode) of the water-saturated column at a flow rate of 2 mL/min. Approximately two PVs of de-aired water were then introduced through the top of the column (down flow mode) at a flow rate of 2 mL/min to displace mobile PCE-DNAPL from the column. Two additional pore volumes of de-aired water were then injected into the column in an up flow mode to displace any additional PCE-DNAPL. Following the establishment of residual PCE-DNAPL, an aqueous RNIP suspension was introduced into the column in a down flow mode. Effluent samples were collected during the delivery process to monitor for displaced PCE-DNAPL.

II.2.2.3 Z-Loy Delivery

For column experimental methods, refer to Section II.2.1.3.

II.2.2.4 Emulsion Delivery

A 1-D column experiment was conducted in a Kontes borosilicate glass column (4.8 cm internal diameter) containing Federal Fine sand with an approximate packed length of 10 cm. The column was prepared and packed following methods outlined by *Pennell et al*. [1993]. TCE-DNAPL (dyed with 1 x 10^{-4}M Oil-Red-O for visualization purposes) was entrapped within the column at a saturation of approximately 15.8%, an estimate based on an analytical solution developed by *Phelan* [2004] using pre- and post-NAPL entrapment tracer test results. Emulsion was introduced to the column in upflow mode using a syringe pump (Harvard Apparatus, Inc.) at a flow rate of approximately 0.5 mL/min (Darcy velocity = 0.028 cm/min) for approximately 2.84 pore volumes. This pulse of emulsion was immediately followed by 3.7 pore volumes of Milli-Q water. Throughout the experiment, effluent samples were periodically collected using an autosampler (ISCO Retriever II) and were quantified for density, emulsion content (oil, surfactant, and iron), effluent iron concentrations, and effluent TCE concentrations.

II.2.3. Reactivity and Transport of Delivery Systems in Columns Containing Entrapped DNAPL

For all of the column reactivity studies, nZVI suspensions were prepared by pipetting 40 mL of nZVI stock solution into a 1 L Morton flask (Ace Glass Inc.) containing de-aired DI water with 3.5 mM of calcium chloride. The Morton flask was stirred with an impeller rotating at a rate of 200 revolutions per minute, and the stirred suspension was then transferred to the column inlet using a Masterflex peristaltic pump through 1/8-inch outside diameter Teflon® tubing. The average concentration of nZVI at the column inlet was 63.5±3.1 g/L (total iron = Fe^{2+} + Fe^{3+}), as determined from six samples collected during the introduction of nZVI. Emplacement of nZVI throughout the column was achieved by injecting 22.5 pore volumes of the nZVI suspension to the top of the column (down-flow mode) at a flow rate of 5 mL/min, which resulted in the emplacement of 40.1±2.0 g of nZVI within the column. During introduction of the nZVI suspension, a small amount of PCE-DNAPL was displaced from the column, reducing the initial residual PCE-DNAPL saturation to 5.4% (2.47 g). Following nZVI delivery, DI water containing 3.5 mM calcium chloride was continuously pumped through the column in the downward direction at a flow rate 0.25 mL/min for 238 pore volumes. Aqueous effluent samples were collected periodically to determine the concentration of dissolved phase PCE exiting the column, along with potential reaction products including TCE, DCE, VC, and ethene. After 238 pore volumes of water flushing, the column was rinsed with 6.5 pore volumes of isopropanol (IPA) to extract the mass of PCE remaining in the column. Four additional column studies were conducted under similar conditions to confirm results obtained for RNIP experiment, and to evaluate the effective of surfactant (Tween 80) stabilized and surface modified (Ni coating) nZVI.

Aqueous effluent samples and solid-phase IPA extracts were analyzed for PCE, TCE, cDCE, VC, and ethene content using a Model 6890 Hewlett-Packard gas chromatograph (GC) equipped with a Tekmar® HT3 headspace autosampler (Teledyne Technologies, Inc.) and a 30 m long by

0.25 mm outside diameter (OD) DB-5 column (Agilent) with 0.25 µm film thickness connected to a flame ionization detector (FID). Aqueous samples were introduced using the headspace autosampler, which was programmed to heat samples for 30 min at 70 °C prior to transferring 1 mL of headspace gas into the GC inlet through heated silco-steel tubing. The GC oven was maintained at 35 °C for 7 min, and then increased at a rate of 10 °C/min to 60 °C. Aqueous calibration standards were prepared by injecting small volumes (< 10 µL) of a methanol stock solution containing PCE into 22 mL headspace vials that contained 1 mL of DI water. The IPA samples were directly injected into the GC inlet operated at 250 °C, where the GC oven was maintained at 35 °C for 7 min then increased at a rate of 10 °C/min to 60 °C. Aqueous-phase concentrations of ferrous iron (Fe^{2+}) and total iron ($Fe^{2+} + Fe^{3+}$) were determined using the ferrozine method [*Voillier et al.*, 2000] after digesting samples with 11.1N HCl (ACS grade, J.T. Baker).

II.3. CONTAMINANT MASS REDUCTION IN HETEROGENEOUS MEDIA

II.3.1. Transport and Reactivity of nZVI in Two-Dimensional Aquifer Cells

A series of two-dimensional (2-D) aquifer cells experiments was conducted to assess the delivery and reactivity of nZVI systems developed and evaluated in Tasks 1 and 2.

Aquifer cell experiments were conducted for two different systems, RNIP and Z-Loy.

II.3.1.1. RNIP Aquifer Cell Experiments

For these experiments, the aquifer cell was packed with 20-30 mesh quartz sand under water-saturated conditions. The overall dimensions of the aquifer cell were 30.5 cm (length) by 1.3 cm (width) by 20.5 cm (height). Two end chambers (3.5 cm wide) were constructed at both vertical boundaries (left and right) of the container to establish constant-head conditions. A series of 0.2 cm diameter overflow ports were located in the left and right-hand end chambers of the cell to allow the height of the water to control the head in each end chamber. A schematic diagram of aquifer cell transport visualization experiment is shown in Fig. II-2. In all experiments, water containing 10 mM sodium bicarbonate flowed from left to right by establishing a head difference of 0.8 cm between the two head chambers. After establishing a steady-state base flow condition of 9 mL/min, 10 mL of water dyed with a non-reactive tracer (red) was injected into the porous medium at a rate of 0.5 mL per second through a 10 cm long syringe needle. The injection point for tracer and RNIP was located approximately 5.5 cm from the left-hand side and 9.5 cm from the bottom of the aquifer cell. Transport of the tracer pulse through the aquifer cell was monitored using high resolution digital images captured at regular intervals. Aqueous suspensions of RNIP (10 g/L) and S-RNIP (1 % Tween 80 + 10 g/L RNIP) were injected in the flow container following the procedure used for the non-reactive tracer. Digital images of the nanoscale iron were captured for a period of 1 hour.
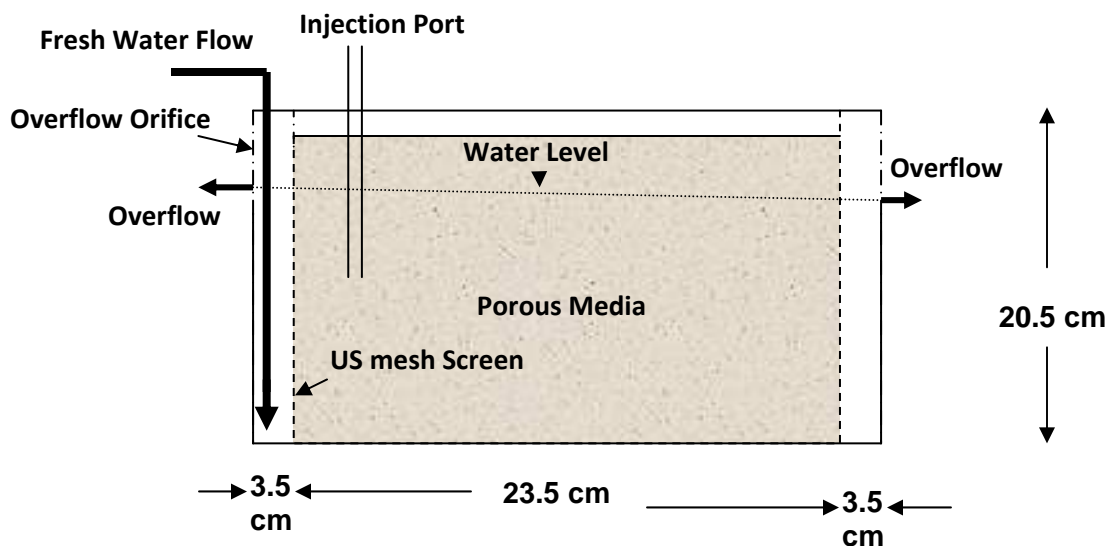
Figure II-2. Schematic diagram of the aquifer cell used to evaluate RNIP transport and retention.

II.3.1.2. Z-Loy Aquifer Cell Experiments

The second series of experiments employed a cell having dimensions of 63.5 cm x 38 cm x 1.4 cm, and was conducted following methods outlined in *Ramsburg and Pennell* [2002] and *Suchomel et al.* [2007]. The cell also contained 18 screw cap sampling ports aligned in four vertical sections, to determine local concentrations throughout the box. The cell was packed under water saturated conditions with a 2 inch layer of F-70 Ottawa Sand at the bottom. The remainder of the box was packed to contain low permeability lenses (F-70) within a background medium comprising the 40-50 fraction of Ottawa Federal Fine. Upon completion of packing the advective and dispersive transport properties of the medium were assessed using a nonreactive, conservative tracer test. 30 mL of dyed TCE was then injected into the source zone at 0.5 mL using a syringe pump fitted with an 18-gauge needle that ended 15 cm below the surface in the center of the cell. The TCE was allowed to redistribute for 24 hours after completion of the injection. Light transmission analysis was conducted to determine TCE saturation. This analysis was completed using a Flathead 80 Light bank, a Nikon Coolpix 950 digital camera. Saturation distributions were determined and were thickness averaged on a pixel basis using MATLAB and the total volume of TCE present in the source zone was determined (within 5% of known amount injected). A second non-reactive, conservative tracer test was subsequently conducted prior to the introduction of iron particles. Flow was maintained using a constant head reservoir located at the influent end of the cell. In this aquifer cell, two experiments were conducted to evaluate Z-Loy emplacement and reactivity within DNAPL source zones (Table II-1). In the first experiment, Z-Loy was injected upstream of the DNAPL source to evaluate its ability to distribute into the source zone. The second experiment directly injected Z-Loy into the source zone. In both experiments, the background flow from the influent to effluent end chambers was 1 mL/min. Subsequent to the introduction of Z-Loy flow in the aquifer cells was maintained at a rate of 4.5 mL/min. The residence time with the aquifer cell was approximately 5 hr. Four of the 18 sampling ports were routinely monitored during the course of each experiment (Fig. II-3).

Table II-1. Aquifer Cell Properties.

	Pore Volume (mL)	TCE added (mL)	Overall TCE Saturation
Aquifer Cell #1	1364	31.81	2.33%
Aquifer Cell #2	1312	23.29	1.75%
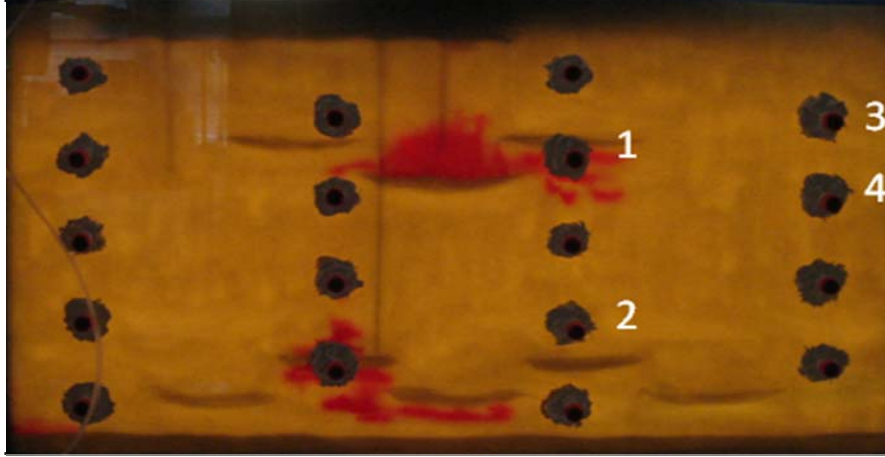
Figure II-3. Sampling port locations.

For the first experiment (Aquifer Cell #1), approximately 200 mL of the Z-Loy suspension was injected upstream of the source zone at 5 mL/min. Port and average mass flux effluents were sampled for chlorinated compounds over the next 1.5 pore volumes. Effluent samples were also monitored for the presence of Cl- and total iron content. Following this period, a second injection of 200 mL of Z-Loy was implemented in the same location and effluent samples were taken over another 2 pore volumes.

For the second experiment (Aquifer Cell #2) 200 ml of Z -Loy (from a new supply) was injected at 5 mL/min directly into the NAPL source. Again, port and average mass flux effluent samplingproceeded over the next 1.5 pore volumes, as well as effluent sample monitoring for the presence of Cl⁻ and total iron content. An additional 200 mL of Z-Loy was subsequently injected at locations to the immediate left and right (100 mL each) of the original injection point.

II.4. MATHEMATICAL MODELING OF nZVI DELIVERY AND REACTIVITY IN DNAPL SOURCE ZONES

Simulation of nZVI delivery and reactivity in DNAPL source zones requires a multiphase multicomponent flow and transport modeling approach. In this research we investigated two distinct approaches to nZVI delivery: direct injection of an aqueous nZVI suspension (e.g., Z-Loy, RNIP) and injection of emulsified nZVI. A number of modeling approaches were considered to model these alternative delivery systems. The outline of the conceptual models associated with these approaches and a brief description of their governing equations and numerical implementation are presented below. More complete descriptions of the models are presented in the results section of this report.

A conceptual model for the nZVI/emulsion delivery system is depicted in Fig. II-4. Here, three phases are considered: a mobile aqueous phase and immobile NAPL and solid phases. Once delivered into the porous medium, the nZVI or emulsion droplets, consisting of butanol, ZVI, surfactant and oil, are treated as a single solute in the aqueous phase. This approach assumes emulsion stability until contact with the DNAPL, and is consistent with findings of the emulsion transport studies conducted under Task 2. Thus, components in the aqueous phase include nZVI particles or emulsion droplets, dissolved NAPL components (e.g. TCE), and NAPL component degradation products (e.g., cis-DCE, acetylene, ethene, and ethane).

During the transport process, nZVI or emulsion droplets may be deposited to (retained by) the solid phase. When emulsion droplets contact the NAPL phase, a portion will destabilize and their components (ZVI, surfactant, butanol, and oil) will be released. Subsequent to destabilization, organic degradation and iron corrosion may occur, either within the DNAPL or at the DNAPL/aqueous interface. The presence of reaction components, together with the soybean oil, will affect the density and viscosity of the NAPL. In addition, the presence of the surfactant will affect the aqueous-NAPL interfacial tension, and thus, could lead to NAPL mobilization.

To implement the above described conceptual model, it is necessary to be able to simulate (1) NAPL mobilization; (2) emulsion/nZVI transport; and (3) nZVI reactivity and transport of reactants and reaction products in a NAPL source zone. This research effort focused on development of mathematical modules to describe these distinct processes.
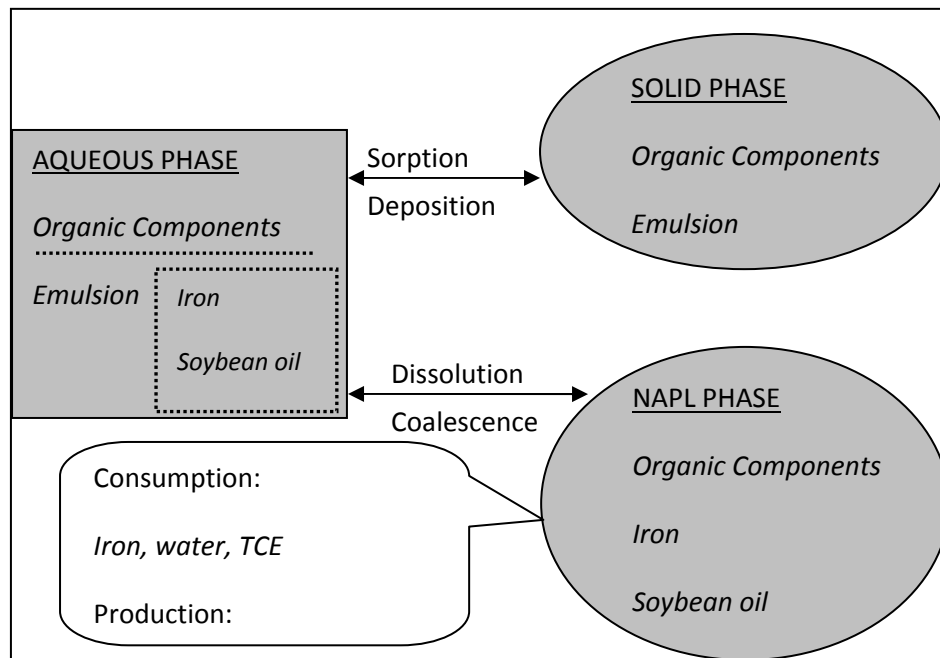
Figure II-4. Conceptual model of phases, components, interphase mass transfer, and reaction mechanism.

19

Model development was based upon standard macroscopic phase and component mass balance relations [*Abriola et al., 1997*]. Flow of the aqueous and NAPL phases can be represented by phase mass balance equations:

$$\frac{\partial}{\partial t}[\phi\rho_\alpha S_\alpha] - \nabla \cdot [\rho_\alpha \frac{kk_{r\alpha}}{\mu_\alpha}(\nabla P_\alpha - \rho_\alpha g)] = \phi \sum_i \sum_\beta E_{\alpha\beta_i} \quad \alpha = a, n \tag{4}$$

where, $\alpha = a$, n denotes the aqueous and NAPL phases respectively; ø is porosity, ρ_α is the mass density of the α phase; k is the intrinsic permeability tensor; $k_{r\alpha}$ is the relative permeability to the α phase; P_α is the α phase pressure; and $E_{\alpha\beta i}$ is the interphase mass transfer rate of component i between the α and β phases.

Component mass balance for a component i may be expressed as:

$$\frac{\partial}{\partial t}[\phi S_\alpha \rho_\alpha \omega_i^\alpha] + \nabla \cdot \phi S_\alpha \rho_\alpha [\omega_i^\alpha v^\alpha - D_{iH}^\alpha \nabla \omega_i^\alpha] = \phi \sum_\beta E_{\alpha\beta_i} \quad \alpha = a, n \tag{5}$$

where ω_i^α is the mass fraction of component i in phase α; v_α is the mass average velocity of the α phase; D_{iH}^α is the hydrodynamic dispersion tensor for component i in the α phase.

The phase and component mass balances are coupled through interphase mass exchange term $E_{\alpha\beta i}$. Here, the interphase mass transfer between NAPL and aqueous phases was modeled using a linear driving force relation:

$$E_{\alpha\beta_i} = \rho_\alpha \hat{k}_{\alpha\beta_i}(\omega_i^{eq,\alpha} - \omega_i^a) \tag{6}$$

where $\omega_i^{eq,\alpha}$ is the equilibrium mass fraction of component i in phase α; and $\hat{k}_{\alpha\beta_i}$ is the lumped mass transfer coefficient. $\hat{k}_{\alpha\beta_i}$ can be determined through correlations that relate to the system properties, which are typically expressed as:

$$Sh = aR_e^b \varepsilon_n^c \tag{7}$$

where $Sh = \hat{k}d_p^2/D^*$ is the modified Sherwood number, d_p is the particle size, D^* is the free liquid diffusivity coefficient, R_e is the Reynolds number, ε_n is the NAPL phase volumetric fraction, and a, b, and c are fitting parameters. Different correlations were developed to account for NAPL-aqueous system interphase mass exchange.

In the conceptual model, phase properties, such as density, viscosity, and interfacial tension must be expressed as functions of phase composition. Liquid phase density is estimated using Amagat's Law:

$$\rho_\alpha = \frac{\sum_c \chi_\alpha^c M_c}{\sum_c \frac{\chi_\alpha^c M_c}{\rho_c}} \tag{8}$$

where χ_α^c is the mole fraction of component c in α phase, and M_c is the molecular weight of c.

Phase viscosity can be expressed with a form similar to Amagat's Law:

$$\mu_\alpha = \left(\sum_c \frac{\left(\chi_\alpha^c \right)^{m_c}}{\mu_c} \right)^{-1} \tag{9}$$

where m_c are fitting parameters to be determined by experiment. Aqueous/NAPL interfacial tension for mixtures may be estimated using the model by *Fu et al.* [1986], which was considered as the most accurate approach in the review by *Demond and Lindner* [1993].

DNAPL mobilization was modeled based on the concept of total trapping number (see section II.2.2 above). Numerical simulations presented herein were conducted using a modified version of an existing two-dimensional Galerkin finite element multiphase compositional simulator, the Michigan Subsurface Environmental Remediation (MISER) Model [*Abriola et al.,* 1997].

Mobilization of entrapped NAPL was captured in MISER by calculating maximum entrapped NAPL saturation as a function of total trapping number. The functional relationship between total trapping number and DNAPL residual saturation was developed based on the experimental data reported in *Pennell et al.* [1996]. To improve model performance under low-IFT conditions, a mixed method approach was implemented in MISER to solve the pressure-based phase mass balance equations, and near-zero capillary pressures were replaced by a linear function, with very small capillary pressure values to maintain numerical stability.

In this research, a number of approaches were evaluated for approximating the transport of nZVI suspensions or emulsions and their reactivity (equations of the form 5). These approaches included: traditional Eulerian advection-dispersion-reaction solute transport models, Lagrangian Continuous Time Random Walk (CTRW) models, and various models based upon clean-bed filtration theory (CFT). To explore the appropriateness of these alternative models, one dimensional solutions were implemented, using finite difference approximation schemes, for simulation of the emulsion/nZVI transport experiments conducted in Task 2. The models were mathematically verified by comparisons of model outputs with analytical solutions, for simplified systems, and by demonstration of good global mass balances, for more complex scenarios. Model performance (validity) was then evaluated by comparing simulations with data from 1-D column experiments.

III. Results and Discussion

III.1. DEVELOPMENT, CHARACTERIZATION, AND REFINEMENT OF NANOSCALE IRON DELIVERY SYSTEMS

III.1.1. Characterization of Existing Approaches for Delivery and Reaction

The various nZVI sources employed in this research differed over a range of physical chemical characteristics, including iron content, ZVI content, surface composition, particle size, and even particle structure. The results of characterization and aqueous phase reactivity batch experiments were used to compare degradation pathways and relative efficiencies of these materials to the more common RNIP.

Results of batch reactivity screening experiments conducted with PCE and different types of nZVI are summarized in Fig. III-1. In the presence of unmodified RNIP (10 g/L), 61 percent of the initial PCE was degraded, primarily to ethene. No degradation of PCE was observed in the Tween 80-only controls. In the presence of 20 mM Ni coated nZVI, 17 percent of the initial PCE was degraded, while in Tween 80-stabilized RNIP only 13.3 percent of the PCE was transformed. Interestingly, Tween 80 stabilized 1 mM, 10 mM and 100mM Ni-coated nZVI increased the PCE degradation to 49, 82 and 85% PCE respectively.
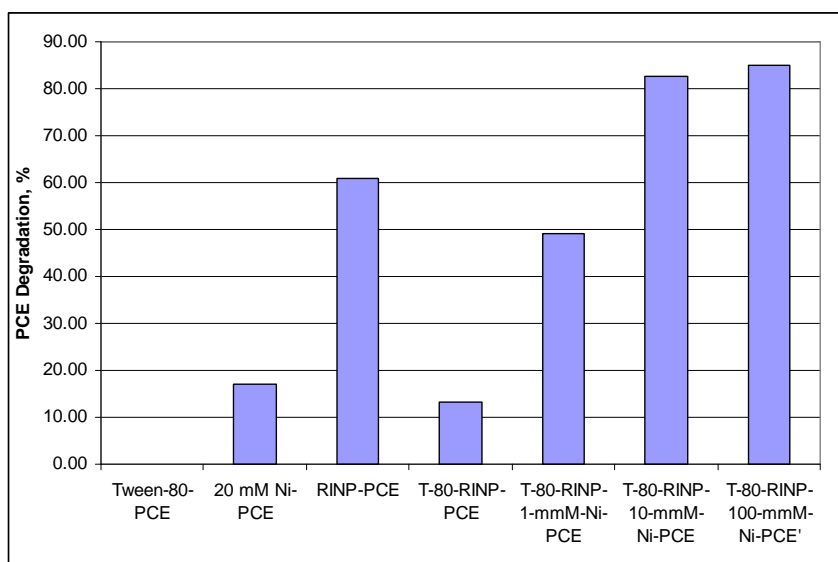
Figure III-1. PCE degradation by different types of nZVI.

III.1.1.1. MTI Reactivity

TCE degradation kinetics using MTI iron was quantified using a series of batch experiments. Here it was assumed that TCE reduction occurred via β-elimination to form acetylene, followed by acetylene reduction to ethane and ethane [*Liu et al.*, 2007]. A nonlinear least squares

regression was used to fit rate constants for the following reaction pathway (loss of TCE and the formation of acetylene, ethene, and ethane) [*Liu et al.*, 2007].

$$TCE \xrightarrow{k_1} Acetylene \xrightarrow{k_2} Ethene$$
$$\xrightarrow{k_3} Ethane$$

Rate constants fitted to the headspace data were converted to aqueous phase rate constants according to:

$$\overline{\hspace{4cm}} \tag{10}$$

where k_i is the reaction rate constant without a headspace (i.e. k_2 and k_3), k_{obs} is the modeled reaction rate constant with headspace, K_H is the dimensionless Henry's law constant for the reactant (here, the value of dimensionless K_H at 20°C was assumed to be 0.35 and 1.02 for TCE and acetylene, respectively), and V_h and V_w are the volume of headspace and aqueous solution respectively. Fitting the batch experimental data yielded mass (Fe) normalized rate coefficients of $k_1 = 4.3 \times 10^{-3}$ Lhr^{-1}g^{-1}, $k_2 = 2.2 \times 10^{-2}$ Lhr^{-1}g^{-1}, and $k_3 = 1.9 \times 10^{-2}$ Lhr^{-1}g^{-1}. Expressed as surface area normalized rate coefficients the values of k_1, k_2 and k_3 are 1.1×10^{-4} Lhr^{-1}m^{-2}, 5.6×10^{-4} Lhr^{-1}m^{-2}, 4.8×10^{-4} Lhr^{-1}m^{-2}, respectively. Given that k_1 is the only reaction representing TCE degradation, this rate coefficient can be compared to other coefficients expressed a k_{TCE} (Table III-1).

Shown in Fig. III-2 are observed and modeled headspace concentrations of TCE and major degradation products through time. Although TCE disappearance is well modeled, the model consistently over predicts the mass of acetylene produced. In addition, data suggest that the MTI iron may have a lag phase (~24 hr) related to the aging of the mineral surface (surface becomes more reactive once placed in the aqueous environment). Thus, further investigation is needed to fully understand the reaction kinetics of the MTI iron.

The average iron efficiency (fraction of theoretically available electrons involved in TCE transformation) was calculated by determining the experimental number of electrons that were consumed in the production of acetylene, ethane, and ethene and dividing this by the theoretical number of electrons that would be released assuming all the iron was oxidized to a specific oxidation sate (Fe^{2+}, Fe^{3+}, or Fe_3O_4 (2.67 electrons are released)). When assuming all the iron in the system is oxidized to Fe^{2+} the average iron efficiency was determined to be approximately 4%. However this value is misleading since the actual amount of iron that was available for the reaction was not determined and TCE could have been degraded to other products that were not detected/monitored.
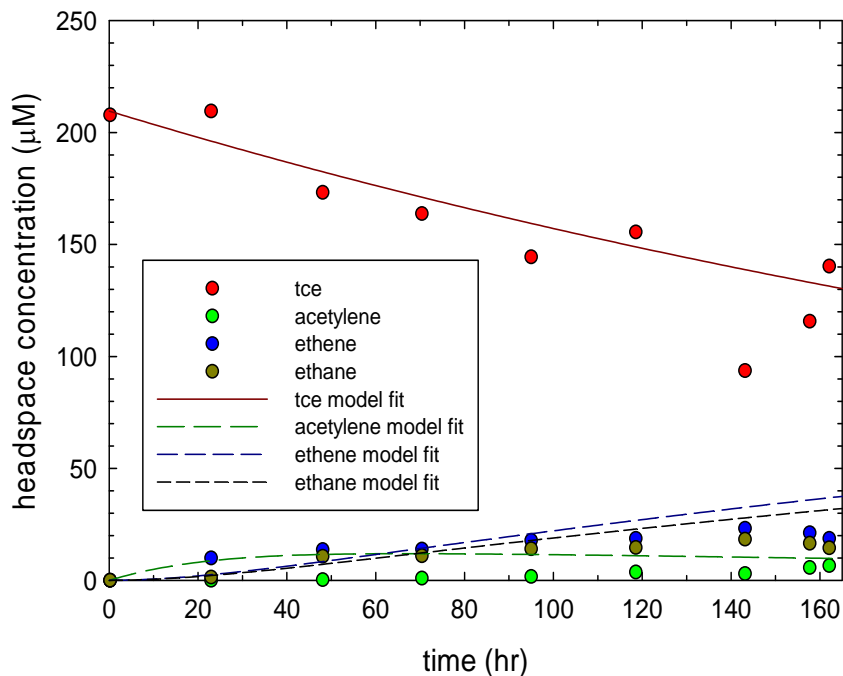
Figure III-2. Observed and fitted TCE, acetylene, ethene and ethane concentration in the headspace of reactors containing MTI iron in water.

Table III-1. Comparison of MTI iron reactivity with TCE to that reported for RNIP.

Iron Type	k_{TCE} $(Lhr^{-1}g_{Fe}^{-1})$	Specific Surface Area (m^2/g)	k_{TCE} $(Lhr^{-1}m^{-2})$	Fe^0 content (wt %)	% Iron Efficiency	Initial Particle Diameter (nm)
MTI (thin oxide layer)	4.3×10^{-3}	40	1.1×10^{-4}	>90	13	60
RNIP (magnetite layer)[1]	1.2×10^{-2}	30	4.0×10^{-4}	27	52	70
RNIP (magnetite layer)[2]	2.4×10^{-2}	20	1.2×10^{-3}	48	-	70

[1] *Liu et al., 2005;* [2] *Liu et al., 2007*

It is well documented in the literature that the reduction reactions promoted by ZVI are surface mediated and that the degradation rate of TCE by ZVI with respect to the contaminant concentration is characterized by a pseudo-first-order kinetic model wherein the rate constant (k_{TCE}) is a function of the specific surface area of the iron particles. This indicates that the amount of available surface area is an essential factor that governs the TCE reduction rate. *Lin and Lo* [2005] therefore suggest that HCl-washed and H_2-reduced Fe^0 have higher k_{TCE} values than untreated iron, since pretreatment of the iron particles reduces the iron oxide layer thus increasing the surface area of the particles. *Liu et al.* [2005] report that "the thicker and more crystalline Fe_3O_4 shell of RNIP slows the TCE dechlorination rate and makes some of the Fe^0 inaccessible."

As previously noted, in this investigation we observed a 24-hour lag. Lag phases, however, have not been observed in studies employing iron particles containing magnetite shells. Thus, we hypothesize that the lag observed in our experiments are associated with alterations to the oxide layer that result in exposure of TCE to reactive surface sites. Further research will be required to quantify the oxides pre- and post-experiment.

Li and Farrell [2000] suggest that under neutral pH conditions highly-pure iron will form a maghemite layer prior to the formation of magnetite and, as indicated by *Liu and Lowry* [2006], maghemite is considered to be a passive layer which inhibits the transfer of electrons, whereas magnetite has semiconductive properties that allow electron transport from the underlying ZVI to the solid/liquid interface to occur.

Although RNIP has a smaller iron content than MTI iron (the % weight of iron in MTI is >90% and the % weight of iron in RNIP is reported to be between 27% and 48%, Table III-1), the pseudo-first-order degradation rates of TCE observed in experiments employing RNIP are larger than those observed with MTI iron (Table III-1). This suggests that the magnetite oxide layer has an impact on the reaction kinetics of TCE. Furthermore, as shown in Table III-1, the electron efficiency appears lower for the MTI particles (however, this comparison may be deceptive since, as previously mentioned, the % iron efficiency in our experiments is not corrected for the extent of the reaction).

III.1.1.2. Z-Loy Reactivity

Results of the Z-Loy reactivity experiments are presented in Fig. III-3. Note that products of TCE dechlorination were ethene and ethane; no acetylene peaks were observed throughout the course of the test. A successive pseudo first order reaction pathway was then assumed (TCE → ethene → ethane). Regression models were developed to determine the best fit to the observed data and to gain better insight into the reaction kinetics.
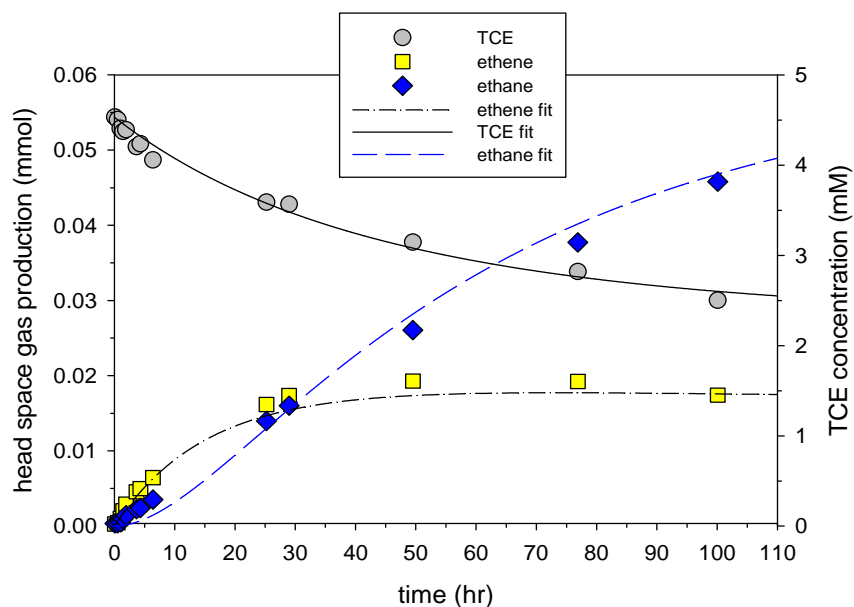
Figure III-3. The observed concentrations of TCE, ethene and ethane in the Z-Loy batch reactor study, and model fits employing first order kinetics

This model yielded reaction rates of $k_1 = 4.8899 \times 10^{-4}$ hr^{-1} and $k_2 = 4.8178 \times 10^{-4}$ hr^{-1} where k_1 is the reaction rate constant from TCE to ethene and k_2 is the reaction rate constant from ethene to ethane. Fitted curves are compared to the experimental data in the Fig. The specific surface area of Z-Loy is 15 m^2/ g which yields a first order deactivation of the iron surface of $k_d = 0.016$ hr^{-1}. Overall, the normalized TCE dechlorination rate constant found was $k = 2.2 \times 10^{-3}$ hr^{-1}m^{-2}. Originally, it was thought that Z-Loy would yield higher reaction rates than previously studied iron particles. However, the rate found was comparable to other literature values for solid iron particles ($k = 1.4 \times 10^{-2}$ to 2×10^{-3} hr^{-1}m^{-2}) [*Liu et. al*, 2005].

As stated before, hydrogen production was also monitored over the course of the experiment, as shown in Fig. III-4. It is believed that a catalytic reaction takes place, in which TCE utilizes H$^+$ in order to produce greater yield [*Liu and Lowry*, 2006]. Further investigation into this reaction and its impact on the system is warranted.
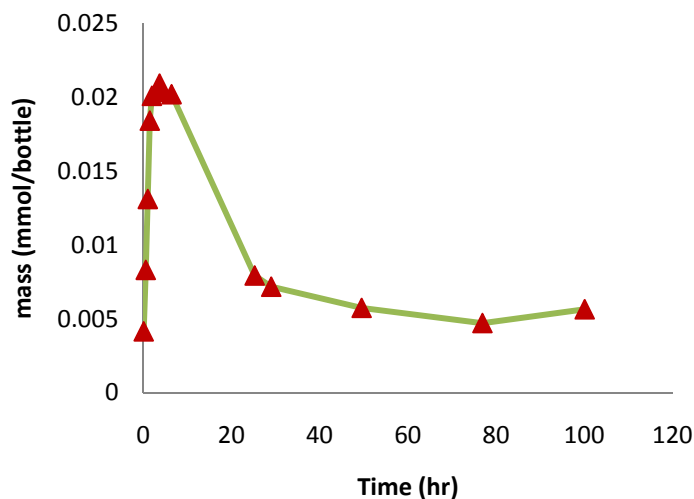
Figure III-4 Hydrogen production during the batch reactor study with Z-Loy

III.1.2. Emulsion Encapsulation of Reactive Iron Particles

Encapsulation of reactive iron particles within an oil-in-water emulsion is a novel concept that may offer some advantages over current delivery approaches. Emulsions (i.e., thermodynamically unstable macro- and mini-emulsions) are utilized in the food, medical and pharmaceutical industries to encapsulate, deliver, and release lipophilic components. With respect to subsurface remediation efforts, emulsions been employed to sequester contaminants and deliver remedial amendments. Location of the iron particles within a nonpolar phase (e.g., soybean oil) may limit corrosion during delivery, thereby conserving the mass of reactive iron for contaminant reduction. Additionally, coalescence between droplets of iron-laden oil and DNAPL may reduce or eliminate the need for contaminant dissolution from the DNAPL prior to contaminant reduction. A necessary prerequisite for assessment of these conceptual advantages, however, is to develop iron-containing, oil-in-water emulsions that are kinetically stable and readily transported in sandy porous media.

III.1.2.1. Surfactant Stabilized Emulsions

Results presented in *Crocker et al.* [2008] and *Berge and Ramsburg* [2009] demonstrate the ability to formulate kinetically stable oil-in-water emulsions containing iron. Shown in Fig. III-5 are representative images (cryogenic SEM and light microscopy) of the iron containing oil droplets and droplet size distributions. Emulsions developed in these studies had mean droplet diameters between 1 and 2 μm, remain kinetically-stable for > 1.5 hr and possessed densities (0.996-1.00 g/mL at 22°C) and dynamic viscosities (2.4-9.3 mPa·s at 22°C and 20 s^{-1}) that are favorable to transport within DNAPL source zones (Table III-2). The interested reader is

27

referred to these publications where additional details can be found on the development and characterization of the surfactant stabilized emulsions.
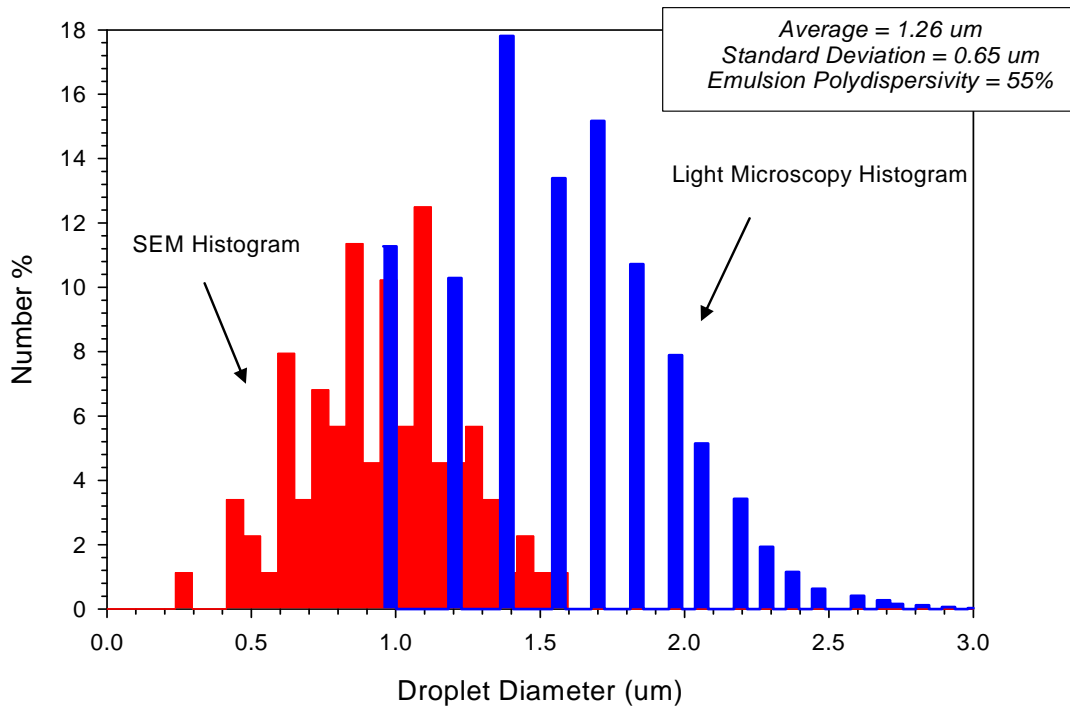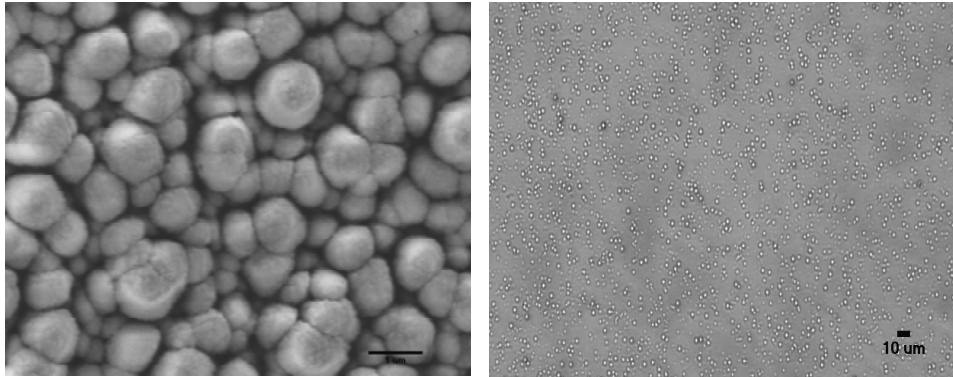
Figure III-5. Oil-droplet distributions for emulsion B; (a) cryogenic SEM micrograph (scale bar is 1 μm) with diameters adjusted for contraction due to freezing, (b) light microscopy micrograph (320 X magnification), and (c) histograms of oil-droplet distributions associated with SEM and light microscopy micrographs. [*Berge and Ramsburg*, 2009]

Table III-2. Selected Iron-Containing Oil-in-Water Emulsions[a]

Emulsion composition[b]	RNIP[b] (% wt)	stability[c] (min)	Density (g/mL)	Viscosity[d] (mPa · s)	IFT[e] (mN/m)
Water	NA	NA	0.998	0.95	35.2 0.3
Emulsion: 10% soybean oil + 6.2% Tween 20 + 2% Span 80	MA coated (0.25%)	100	1.0 ± 0.01	2.7 ± 0.5	7.54 ± 0.24
Emulsion: 10% soybean oil + 6.2% Tween 20 + 2% Span 80	AOT coated (0.25%)	90	1.0 ± 0.03	2.4 ± 0.5	7.07 ± 0.14
Emulsion C: 10% soybean oil + 3.2% F108 + 2.6% oleic acid	OA coated (0.25%)	7	NM	NM	NM
Emulsion D: 10% soybean oil + 6.4% F108 + 5.3% oleic acid	OA coated (0.25%)	90	0.996 ± 0.01	9.3 ± 0.5	8.46 ± 0.13
[a]All properties were measured at 22 ± 3° C and reported as mean (standard error. [b]Compositions in percent weight of total emulsion and comprise weight of particles plus surfactant coating (~2.5 g/L). [c]Kinetic stability as determined using the time to first visible coalescence in undisturbed samples. [d]Viscosity measured at 20 s^{-1}. [e]Interfacial tension with TCE-NAPL; NA = not applicable; NM = not measured because of low kinetic stability.						

III.1.2.3. Gum Arabic Emulsion

The iron containing oil-in-water emulsion created in these experiments was a dark-grey, opaque fluid (Fig. III-6) comprising GA (10.0% wt), soybean oil (9.0 % wt), oleic acid (2.2 % wt), iron (1.2% wt), methanol (0.4% wt) and water (77.2% wt). Note that the Fe^0 content of the emulsion (12 g/L), confirmed by acid digestion, was greater than that typically used in applications within the subsurface (1-10 g/L) [*Berge and Ramsburg*, 2009; *Kirschling et al*., 2010]. The ZVI content of the emulsion was quantified using an acid digestion procedure [*Berge and Ramsburg*, 2009].

Visual inspection of the GA stabilized emulsion suggested kinetic stability in excess of four hours (i.e., no discernible phase separation was observed during this time frame). Destabilization over longer times (4 days) was found to occur via sedimentation (dispersed phase (iron oil + GA) density was 1.15 g/mL) with ~20% volume observed at the bottom of the tube containing the emulsion. Sedimented emulsion droplets were readily resuspended by inverting the tube, suggesting limited coalescence (emulsions broken through coalescence generally require much greater energy input to reform the large surface area represented by suspended droplets). Light

microscopy examination of diluted suspended phase suggested droplet sizes of ~1 µm and smaller (Fig. III-6b) which compares favorably to the number average droplet diameter (1.03 µm) obtained from DLS (not shown). In addition, aggregates of nZVI particles were not observed in any sample, suggesting the iron remained encapsulated within the dispersed phase. Encapsulation of nZVI particles was further confirmed by the microscope images of the diluted settled phase (Fig. III-6c), where larger droplets were found among chains of smaller droplets. The observation of aggregated droplets, particularly those having diameters of several microns, is indicative of an attractive magnetic body force between ferromagnetic dipoles. The images in Fig. III-6 also suggest that, in contrast to surfactant stabilized iron-containing emulsion of *Berge and Ramsburg* [2009], coalescence of oil droplets was suppressed by the existence of GA film. The observed stability against coalescence in the presence of the magnetic attraction between the iron oil cores of the droplets is thought to result from the structural stability provided by the GA film. GA has a complex molecular structure comprising a hydrophobic protein rich backbone to which many hydrophilic carbohydrate blocks are attached [*Dickinson*, 2003]. At the water-oil interface, the protein groups strongly associate with the oil phase, leaving the carbohydrate blocks protruding outwards in the aqueous phase which form a physical macromolecular film around the oil droplets. Once formed, the viscoelasticity of the film can be maintained even when the emulsion is diluted, particularly when the GA to oil mass ratio is approximately 1:1 [*Dickinson*, 2003].
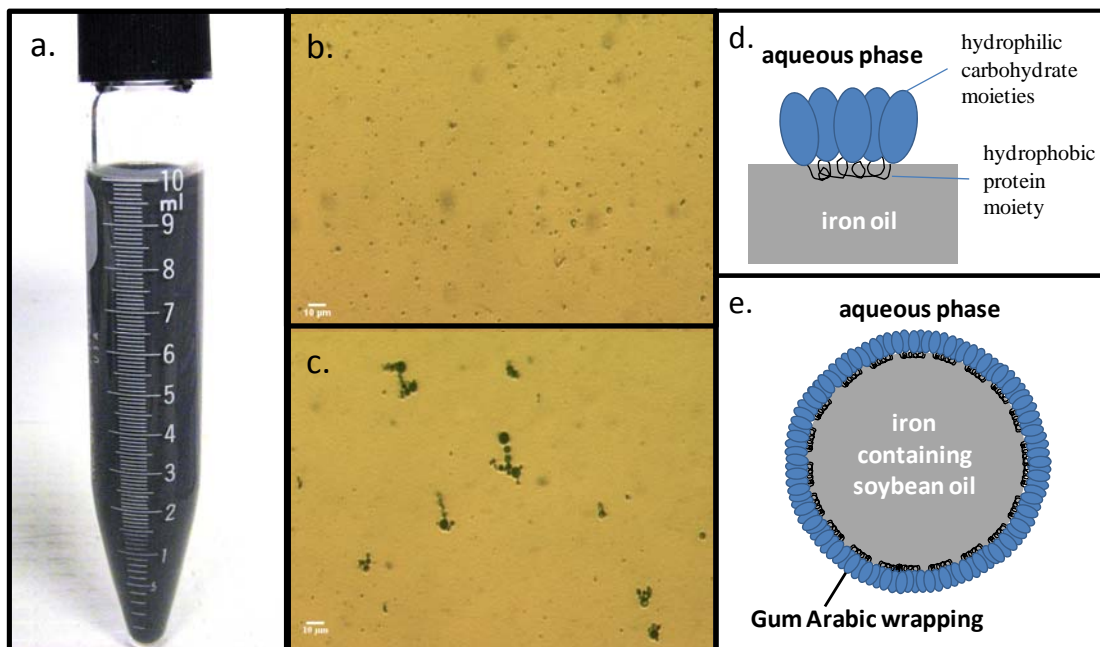
Figure III-6. GA stabilized, iron containing, oil-in-water emulsion: (a) photograph; light microscopy images of the suspended (b) and sedimented (c) fractions (with 10 µm scale bar); conceptual diagram of (d) adsorption of GA to iron oil (after ref. 18), and (e) stabilized droplet.

We hypothesize that the destabilization observed over the first 16 hr of the study resulted from droplet aggregation which hastened sedimentation. In addition, we hypothesize that the non-sedimenting fraction of the emulsion represents a size fraction that is kinetically stable against the coupled aggregation-sedimentation process.

To explore the hypotheses related to aggregation and sedimentation illustrative, like-like interactions between 600 nm and 1100 nm droplets were qualitatively assessed using extended DLVO theory for deformable emulsion droplets [*Ivanov et al.*, 1999; *Denkov et al.*, 2005; *Petsev et al.*, 1995]. The analysis included Van der Waals and magnetic attractive interactions with electrostatic, steric, interfacial dilatation, interfacial bending, and hydration repulsive interactions. It is noted that of these interactions, hydration, interfacial dilatation and interfacial bending are all short range forces that become important when assessing the potential for droplet deformation. The shape of aggregated droplets is important because deformed droplets represent strong aggregation on an energetic path toward coalescence (i.e., film rupture) [*Petsev et al.*, 1995]. Droplet deformation, as assessed by the dimension associated with the flattening of the interface (r, see Fig. III-7), occurs when attractive forces (Van der Waals and magnetic) are stronger than long range repulsive forces (electrostatic and steric) and those forces resulting from increased interfacial area (hydration, interfacial dilatation, and interfacial bending).

In contrast to soft particle barriers provided by grafted polymers, studies conducted on GA stabilized oil-in-water emulsions suggest the that we can conceptualize the emulsion droplets as having an iron oil core that is wrapped in a relatively smooth, structure inducing, viscous film of GA that is ~50 nm thick [e.g., *Vincent et al.*, 1986); *Tan,* 1998]. Taking the iron oil core radius as a (m) and considering the approach of two cores of size a though the beginning of core deformation (Fig. III-7) suggests that we need to consider multiple interactions controlling the overall energy associated with droplet approach.
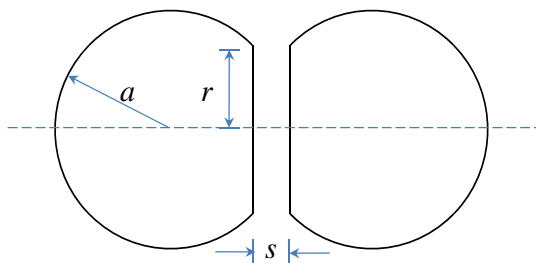
Figure III-7. Schematic for DLVO calculations for deformable droplets

Van der Waals interactions for this scenario can be described as outlined by *Denkov et al.* [1995]. The Hamaker constant was estimated to be 5×10^{-20} J which is a typical value for 10 to18 carbon chain triacylglycerol oils in water [*Damodaran*, 2005]. Magnetic attractive forces were modeled based upon the equation provided by *Phenrat et al.* [2008] but modified for deformation according to the process described in *Petsev et al.* [1995]:

$$\frac{V_M\left(s\right)}{k_BT} = -\frac{8\pi\mu_0M_s^2a^3}{9k_BT\left(\dfrac{s}{a}+2\right)^3} - \frac{32\pi r^2\mu_0M_s^2a}{9k_BT\left(\dfrac{s}{a}+2\right)^4} \tag{11}$$

where μ_0 is the magnetic permeability of vacuum (N/A^2), and M_s is the saturation magnetization of the iron oil (A/m). Under the assumptions that the iron oil can be modeled as a homogeneous continuum, M_s can be estimated by volume averaging the iron oil phase [*Bashtovoy and Berkovsky*, 1987]. Applying an M_{sf} for Fe^0 of 1226 kA/m [*Phenrat et al.*, 2009] and 0.012 for the volume fraction of the magnetic fraction produces an Ms for the iron oil of 14.7 kA/m. Electrostatic interaction can be described as outlined in *Phenrat et al.* [2008].

Since the GA film is conceptualized as a wrapping and not as grafted soft polymer chains a general description for the steric interaction is sufficient (i.e., soft particle theory as applied by *Phenrat et al.* [2008] is not required). Steric interactions, hydration interactions, the interfacial dilatation, that is the chemical energy required to create additional interface, and the repulsion associated with the physical work required to deform the interface is interfacial bending are all outlined in *Ivanov et al.* [1999].

Illustrative results from the DLVO analysis are shown in Fig. III-8 with deformation (*r*) and separation (*s*) normalized by the radius of the iron-oil core (*a*) (see Fig. III-8 for a conceptual model of the droplets). Calculations suggest that the minimum energy condition lies at zero deformation for both droplet sizes. This can be seen in the contour plot of deformation versus separation by the energy valley (s = 450 and 181 nm for the 600 and 1100 nm diameter droplets, respectively) that extends to the zero deformation condition (r = 0) [*Petsev et al.*, 1995]. It is important to note when comparing these separation distances to those dimensionless distances reported in Fig. III-8, that the core radius (a) represents the iron-containing oil droplet without the GA wrapping (see Fig. III-6d-e). The absence of deformation in these calculations is consistent with the lack of coalescence seen in the DLS measurements and suggests that the GA structure provides a competent physical-chemical barrier against the strong magnetic attraction.
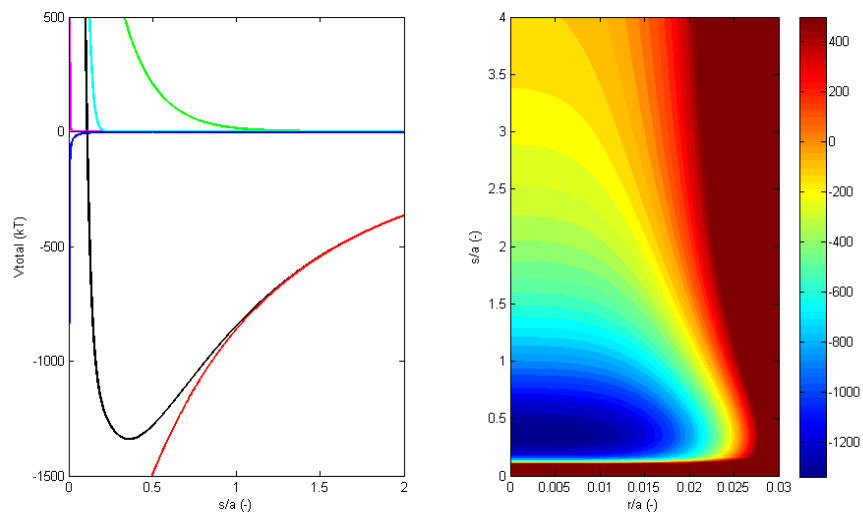
Figure III-8. Interaction energies for 600 (top) and 1100 (bottom) diameter GA wrapped droplets for zero deformation (left) and as a function of deformation (right). Plots are in terms of dimensionless separation (*s/a*) and dimensionless deformation (*r/a*), where *a* is the radius of the magnetic, iron oil core (i.e., 600 nm diameter GA wrapped drop has a 250 nm core radius (*a*) and GA wrapping thickness of 50 nm). Lines in zero deformation interactions are color coded: total (black), magnetic (red), Van der Waals (blue), electrostatic (green), steric (cyan) and hydration (pink). Interfacial dilatation and surface bending are only operable for *r>0*. Color contours correspond to interaction energies for droplets undergoing deformation. Values greater than 50 (top) and 500 kT (bottom) are shown as dark red to highlight the minimum energy state. See Fig. III-7 for a schematic definition of droplet deformation.

Application of the theory of reversible coagulation [*Derjaguin*, 1989] suggested that droplet-droplet contact (and hence coalescence) is avoided using the GA emulsion. Reversible aggregation, however, may still occur in the secondary minimum. In the case of the 600 nm diameter droplet, the secondary minimum (~-40 kT) occurs at long range (431 nm). The large separation distance and zero deformation suggest that aggregates of 600 nm droplets are relatively weak and perhaps overcome by mixing which is consistent with our observation of slow sedimentation [*Petsev et al.*, 1995; *Becher*, 2001]. In contrast, the secondary minimum associated with 1100 nm droplets represents a strong attractive force (~-1340 kT) that may lead to more rapid aggregation and settling – an assessment that is supported by the observation of chains and clusters of relatively large droplets in the sedimented fraction (Fig. III-6c). It is interesting that the droplet size distributions (Fig. III-5) do not appear to be consistent with the extent of aggregation expected from the strong, albeit theoretical, interaction calculated using extended DLVO theory (see Table III-3). Thus, it is important to recall that the temporal study of droplet size distribution was conducted in the context of coalescence where the vials were inverted 3-4 times before sampling. We hypothesize that this inversion process was sufficient to separate the flocculated droplets – a hypothesis that is supported by the ability to re-suspend the settled emulsion (described above).

Table III-3. Parameter summary for DLVO calculations.

Parameter	Value	Units	Description	Reference
a	2.5×10^{-7} 5.0×10^{-7}	m	iron oil core radius	assumed, illustrative calculations
k_B	1.38065×10^{-23}	$\dfrac{J}{K}$	Boltzman constant	*Lide*, 2008
T	295	K	temperature	measured
A_H	5.00×10^{-20}	J	Hamaker constant for oil-oil interact. in water	*Damodaran*, 2005
ε_0	8.85×10^{-12}	$\dfrac{A \cdot s}{V \cdot m}$	permittivity of free space	*Lide*, 2008
ε_r	79.99	-	relative permittivity of water	*Lide*, 2008
μ_0	1.257×10^{-6}	$\dfrac{N}{A^2}$	permeability of free space	*Lide*, 2008
ψ_0	-4.30×10^{-2}	V	zeta potential of droplet	measured
M_s	1.47×10^{4}	$\dfrac{A}{m}$	saturation magnetization of iron oil	calculated, see Equation SD-E5
κ	1.03869×10^{7}	$\dfrac{1}{m}$	Debye-Huckel parameter ($I = 1 \times 10^{-5}$ M)	calculated
δ	5.00×10^{-8}	m	Gum Arabic thickness	*Tan,* 1998
f_0	3×10^{-2}	$\dfrac{J}{m^2}$	interaction energy for water – drop pair	*Ivanov et al.*, 1999
a_w	1.93×10^{-10}	m	molecular size of water	*Salou et al.*, 1998
λ_0	1×10^{-9}	m	decay length for hydration force	*Ivanov et al.*, 1999
B_0	-5×10^{-11}	N	interfacial bending moment	*Ivanov et al.*, 1999
C_{EL}	6.02×10^{21}	$\dfrac{molec}{m^3}$	number concentration of electrolyte	Calculated
e	1.602177×10^{-9}	C	elementary charge	*Lide*, 2008
γ	3.0×10^{-2}	$\dfrac{N}{m}$	oil-water interfacial tension	estimated w/ data in *Dickinson et al.*, 1991
Γ	6.576×10^{16}	$\dfrac{molec}{m^2}$	accumulation of GA at oil water interface	*Nakauma et al.*, 2008

II.1.2.4 Reactivity Studies within GA Emulsion

A series of batch experiments was designed to quantify apparent rate coefficients for the four phase system (headspace, dispersed phase (oil droplets), continuous phase (aqueous phase) and iron particles) assuming the reaction occurs within the dispersed (oil) phase. Reactors were iron limited with a TCE to Fe^0 molar ratio of 1.8 mol/mol. Headspace data for both TCE and H_2 shown in Fig. III-9 (averages of triplicate reactors) demonstrate reactivity in comparison to that in the control reactors for which the emulsion did not contain iron. Recall that phases were assumed to be in equilibrium given the large surface area represented by the emulsion droplets, and the rapid partitioning reported for completely mixed reactors [*Gossett*, 1987]. Thus the control (emulsion without iron) represents the equilibrium distribution of TCE between the three fluid phases. The data suggest that over the ~300 hr monitoring period, 4 mmol TCE was consumed in presence of between 17 and 24 mmol e- (range established by assuming Fe^0 goes to Fe (II) and Fe (III), respectively).

Rate coefficients reported in Table III-4 were obtained using a weighted (inverse of standard error from triplicate reactors), non-linear, least-squares regression (within MATLAB) of headspace concentrations against the model described by:

$$\frac{dC_{TCE}}{dt} = -k_{obs,TCE}k_d^{\circ}C_{TCE} - k_{obs,TCE-H_2}k_d^{\circ}C_{TCE}C_{H_2}$$

$$\frac{dC_{H_2}}{dt} = k_{obs,H_2} - 4 \cdot k_{obs,TCE-H_2}k_d^{\circ}C_{TCE}C_{H_2} \tag{12}$$

$$k_d^{\circ} = \exp(\text{-}k_d t)$$

where C_{TCE} and C_{H2} are the molar concentrations of TCE and H_2 in the headspace, respectively; $k_{obs,\ TCE}$, $k_{obs,TCE-H2}$, and $k_{obs,H2}$ are the rate coefficients corresponding to the pseudo-first order consumption of TCE, pseudo-second order, catalytic, hydrogenation of TCE, and pseudo-zeroth order production of H_2, respectively; and k_d is the first-order deactivation term [*Liu et al.*, 2005]. Here the hydrogenation of TCE is assumed to proceed to ethane. Observed ethane concentrations were not used in the fitting of the kinetic model to the TCE and H_2 concentrations. Rather, we used the ethane concentrations as a predictive check on the amount of hydrogenation suggested by the fitted rate coefficients. Predicted ethane concentrations shown in Fig. III-9 were generated using the fitted rate coefficients (Table III-4) and the catalytic hydrogenation reaction represented by:
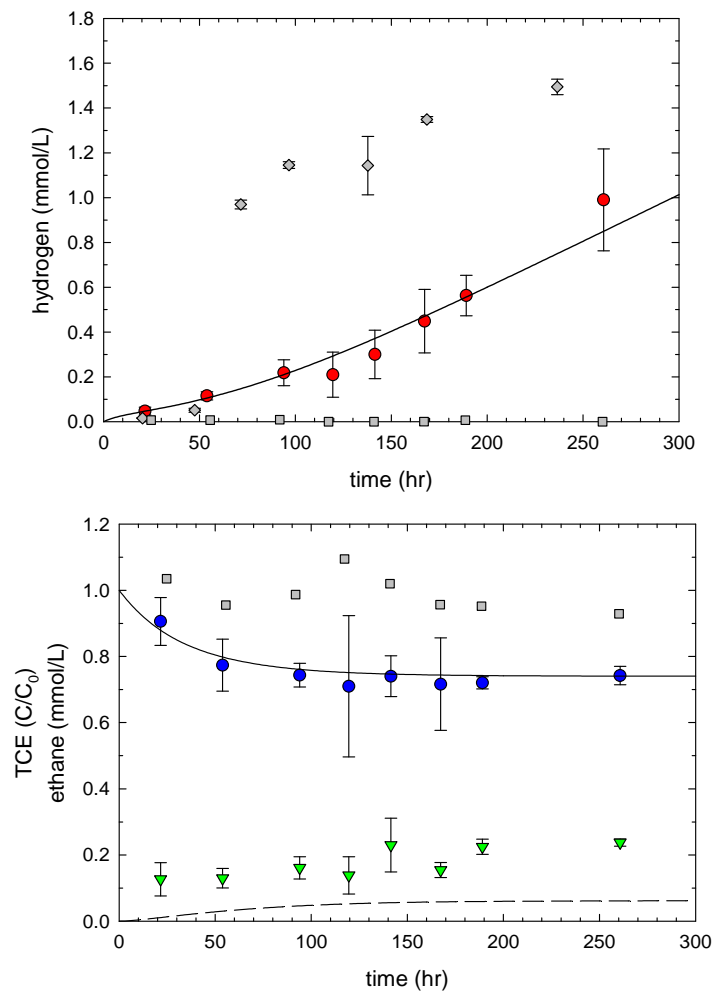
Figure III-9. Reaction data and kinetic model fit for TCE transformation by the GA stabilized emulsion. Error bars represent standard error of triplicate reactors. Headspace data and model fits for TCE (blue circles, top) and hydrogen (red circles, bottom). Control reactors included absence of iron (gray squares, top and bottom) and absence of TCE (gray diamonds, bottom). TCE and hydrogen data were simultaneous fit (solid lines). Ethane data (green triangles, top) are shown with predicted concentration (dashed line) from hydrogenation reaction fit to TCE and hydrogen data.

Table III-4. Fitted rate coefficients for reaction within the dispersed phase of the GA emulsion.

	fitted rate coefficient for reaction in droplet[1] k	surface normalized rate coefficient for reaction in droplet[2] k_{SA}
TCE consumption (iron)	$(7.9\pm0.6)\times10^{-3}\ \dfrac{1}{hr}$	$(1.5\pm0.1)\times10^{-5}\ \dfrac{L_{oil}}{m^2\cdot hr}$
TCE consumption (catalytic)	$(1.1\pm0.2)\times10^{2}\ \dfrac{L_{oil}}{mmol_{H_2}\cdot hr}$	$(2.0\pm0.3)\times10^{-1}\ \dfrac{L_{oil}^2}{mmol_{H_2}\cdot m^2\cdot hr}$
H_2 production	$(4.7\pm0.4)\times10^{-2}\ \dfrac{mmol_{H_2}}{L_{oil}\cdot hr}$	$(8.9\pm0.8)\times10^{-5}\ \dfrac{mmol_{H_2}}{m^2\cdot hr}$
TCE deactivation	$(2.9\pm0.2)\times10^{-2}\ \dfrac{1}{hr}$	---

[1]represents reaction rate coefficient in absence of headspace, [2]specific surface area of the iron particles was determined to be 8 m^2/g.

$$\frac{dC_{C_2H_6}}{dt} = k_{obs,TCE-H_2}\, k_d^{\circ}\, C_{TCE}\, C_{H_2} \tag{13}$$

The fitted pseudo-first order rate coefficient for the consumption of TCE ($k_{obs,TCE}$) was modified assuming the reaction occurs in the oil (k_{TCE}) [*Burris et al.*, 1998].

$$k_{TCE} = k_{obs,TCE} \left(\frac{V_o + \dfrac{V_{aq}}{K_p} + \dfrac{V_g K_H}{K_p}}{V_o} \right) \tag{14}$$

where K_p is the oil-water partition coefficient of TCE, K_H is the Henry's coefficient for TCE, and V_o, V_{aq}, and V_g are the volumes of the dispersed, aqueous, and gas phases, respectively. In general, k can be normalized to produce $k_{SA,TCE}$ as shown in Eq. 15.

$$k_{SA} = \frac{k}{SSA_{Fe}\, C_{Fe,oil}} \tag{15}$$

where, SSA_{Fe} is the specific surface area of the iron particles, $C_{Fe\,oil}$ is the mass concentration of the iron particles in the oil.

Correction of pseudo-second and pseudo-zeroth order reactions can also be accomplished following the general procedure in *Burris et al.* [1998]. Considering the pseudo second order reaction occurring in the oil phase:

$$\frac{dC_{o,TCE}}{dt} = -kC_{o,TCE}C_{o,H_2} \tag{16}$$

where $C_{o,TCE}$ is the concentration of TCE in the oil and C_{o,H_2} is the concentration of H_2 in the oil. It is noted the dimensions on the rate coefficient, k, are $V_o/mol_{o,H_2} \cdot time$, where mol_{o,H_2} is mol of H_2 in the oil. Thus, the concentration term C_{o,H_2} must be corrected (in addition to the rate and $C_{o,TCE}$ terms) by introducing an additional term in the form of $K_{H,H_2}/K_{p,H_2}$ as shown in Eq. 17 with the additional step of normalization.

$$k_{SA} = \frac{k_{obs}}{SSA_{Fe}C_{Fe,oil}} \left(\frac{K_{H,H_2}}{K_{p,H_2}} \right) \left(\frac{V_o + \dfrac{V_{aq}}{K_p} + \dfrac{V_g K_H}{K_p}}{V_o} \right) \tag{17}$$

Similarly, the pseudo-zeroth order rate coefficient, with dimensions $mol_{o,H_2}/V_o \cdot time$ requires the addition of $K_{p,H_2}/K_{H,H_2}$ when correcting the rate coefficient, as shown in Eq. 18 with the additional step of normalization.

$$k_{SA} = \frac{k_{obs}}{SSA_{Fe}C_{Fe,oil}} \left(\frac{K_{p,H_2}}{K_{H,H_2}} \right) \left(\frac{V_o + \dfrac{V_{aq}}{K_p} + \dfrac{V_g K_H}{K_p}}{V_o} \right) \tag{18}$$

For the purposes of comparison, the pseudo-first order rate coefficient for the consumption of TCE can be modified to an equivalent aqueous phase rate coefficient by assuming the reaction occurs in a single phase. Thus, dM_T/dt in the oil phase is assumed to be the same as in the *hypothetical, equivalent* aqueous phase (aqe).

$$\left. \frac{dM_T}{dt} \right|_{oil} = \left. \frac{dM_T}{dt} \right|_{aqe} \tag{19}$$

Defining the rate in both phases produces:

$$V_{oil}C_{oil}k_{sa,oil}SSA_{Fe}C_{Fe,oil} = V_{aqe}C_{aqe}k_{sa,aqe}SSA_{Fe}C_{Fe,aqe} \tag{20}$$

38

where $C_{Fe,aq}$ is the mass concentration of iron in the hypothetical, equivalent aqueous phase. Rearranging Eq. 20, substituting K_p for the ratio of concentrations, and assuming that the *mass* of iron in the aqe is the same as the *mass* in the oil phase:

$$k_{sa,aqe} = K_p k_{sa,oil} \tag{21}$$

Modeling results suggest approximately half of the 160 μmol H_2 produced was subsequently consumed in the hydrogenation reaction. Total ethane production, estimated using K_{ow} values for the soybean-oil partition coefficient [*Sangster*, 1997] to be 25 μmol, is consistent with this amount of hydrogenation. Surprisingly little production of ethane occurred beyond what is predicted by the hydrogenation reaction (Fig. III-9) suggesting coupling pathways may be enhanced within the soybean oil. *Liu et al.* [2005] found that coupling products (C3-C6) accounted for up to 30% of the TCE mass degraded in aqueous phase systems. We hypothesize that lack of products observed here resulted from formation of a broad distribution of coupling products that remained below our quantification limits due to partitioning (reactors contained three fluid phases). Computational and experimental studies that report a 0.5 log unit increase in K_{ow} for each carbon addition demonstrate the affinity of coupling products for the oil and support this hypothesis [*Sangster*, 1997; *Garrido et al.*, 2009]. It is interesting that water remains reactive within the emulsion (as evidenced by the production of H_2) even as the reaction with TCE slows. This suggests that: sites responsible for catalyzing the conversion of TCE may be passive (no effects on H2 production just decrease in H_2 consumption); reactive sites on the iron surface remain accessible to water after becoming inaccessible to TCE (water can transport through porous oxides [*Wang and Farrell*, 2003] or both.

Comparison of surface normalized rate coefficients to those reported for aqueous suspensions of iron particles must consider the capacity that the oil droplet has for chlorinated solvents. The TCE rate coefficient within the oil droplets can be shown to be equivalent to an aqueous phase rate coefficient of ~5×10^{-3} L_{aq}/m^2-hr (Eq. 12) which is similar to rate coefficients reported for bare iron particles [*Liu et al.*, 2005; *Liu et al.*, 2007; *Song and Carraway*, 2008]. The emulsion, however, is ~10% oil, suggesting that conversion within the emulsion is equivalent to an aqueous phase rate coefficient of ~5×10^{-4} L_{aq}/m^2-hr. *Berge and Ramsburg* [2010] employed surface normalized, maximum observed rates of TCE consumption to compare aqueous and nonaqueous reactions mediated by various types of iron. Maximum observed rates of TCE consumption were employed because aqueous phase reactions are limited by the solubility of TCE in water, while reactions within the nonaqueous phase are limited by the amount of water within the organic phase. Maximum observed rates were found to typically range between 1 and 200 $\mu mol_{TCE}/m^2$-hr for Fe^0 particles and between 50 and 500 $\mu mol_{TCE}/m^2$-hr for bimetallic particles [*Berge and Ramsburg*, 2009]. When the equivalent rate coefficient of the GA emulsion system is applied with the solubility of TCE in water (~ 8 mM, *Ramsburg and Pennell* [2002]), the maximum observed rate of TCE consumption is ~100 μmol/m^2-day. Thus, the rate of TCE conversion in the emulsion system compares favorably to rates observed in aqueous suspensions of iron particles [*Quinn et al.*, 2005; *Phenrat et al.*, 2009] while stabilizing 12 g/L Fe^0.

Overall, the GA emulsion represents an advance in stabilizing high quantities of nZVI particles for transport in porous media while maintaining particle reactivity at rates that are consistent with polymer coated particles. Droplet sizes on the order of a micron have been shown to be mobile within fine sand due to limited potential for straining [*Berge and Ramsburg*, 2009;

Coulibaly and Borden, 2004; *Borden*, 2007]. Moreover the net negative charge on the emulsion droplets and the ability for gentle mixing to maintain the kinetic stability suggest that the GA emulsion may be transported within porous media. The combination of the relatively high IFT with TCE-NAPL (30.75±0.02 mN/m) and modest viscosity (16.8±0.1 mPa-s at 10 s^{-1} and 20.00±0.01 ℃) suggest that the GA emulsion has limited potential to mobilize DNAPL during delivery.

The materials employed to create the emulsion (GA, soybean oil, oleic acid) are food-grade, commodity chemicals and may enhance the synergy between iron-based reductive dechlorination and metabolic reductive dechlorination; particularly since encapsulation of iron sequesters the chemical and biological reactions [*Borden*, 2007; *Kirschling et al*., 2010*; Xiu et al*., 2010; *Barnes et al*. 2010]. Immersion of the iron within oil immediately following particle synthesis protects the Fe^0 from oxidation by atmospheric oxygen and reaction with water, suggesting the possibility of limited decline in ZVI content during longer-term storage. Because the reaction occurs in a non-aqueous phase (oil or NAPL), the availability of dissolved water becomes critical and represents a tradeoff between TCE consumption and H$_2$ production [*Berge and Ramsburg*, 2010]. While a mechanistic study of the oil-based reactions was beyond the scope of the present study, the results presented here warrant follow on study to elucidate reaction pathways, as well as the influence of iron mineralogy on the reaction.

III.1.3. Iron-Mediated Reactions within the NAPL

Aqueous slurries or suspensions containing reactive iron nanoparticles are increasingly suggested as a potential means for remediating chlorinated solvent nonaqueous phase liquid (NAPL) source zones. Aqueous based treatment approaches, however, may be limited by contaminant dissolution from the NAPL and the subsequent contaminant transport to the reactive nanoparticles. Reactions occurring within (or at the interface) of the NAPL may alleviate these potential limitations, but this approach has received scant attention due to concerns associated with the reactivity of iron within nonaqueous phases. Results presented in *Berge and Ramsburg,* [2010] suggest that iron nanoparticles are reactive with TCE-NAPL and exhibit dechlorination rates proportional to the concentration of (soluble) water present within the NAPL. The interested reader is referred to the publication for full details. The important conclusion is that reaction within the NAPL appears as efficient (with respect to iron consumption) as reactions occurring within the aqueous phase. The results open important new questions related to the possibility of engineering reactions which maximize the effectiveness of the iron particles through control of NAPL composition. Manipulation of NAPL composition within the subsurface is well established with a rich body of literature available related to techniques that may be employed within NAPL source zones [e.g., *Roeder et al*., 1996; *Martel et al*., 1998; *Lunn and Kueper*, 1999; *Jawitz et al.*, 2000; *Ramsburg and Pennell*, 2002].

At present, iron treatment of NAPL source zones is limited by the mass ratio of iron needed to degrade chlorinated solvents to benign products. For conversion of TCE to ethene the mass ratio lies between 0.85 and 1.3 g_{Fe^0}/g_{TCE} depending whether Fe^0 is oxidized to Fe^{III} or Fe^{II}, respectively, or an intermediate oxidation state such as that found in magnetite. Thus, iron treatment may ultimately be shown to be at its best when employed as a follow-on treatment designed to limit mass discharge from hotspots, or integrated within the aggressive mass removal technologies. One of the challenges related to engineering reactions within the NAPL is co-

location of NAPL and iron particles. Existing techniques for targeted delivery such as interfacial targeting [*Saleh et al*., 2005a; *Saleh et al*., 2005b] and iron containing oil-in-water emulsions [*Crocker et al*., 2008; *Berge and Ramsburg*, 2009] may, therefore, prove good candidates for study of follow-on or integrated treatment.   In fact, oil-in-water emulsions have also been employed to recover NAPL or alter NAPL composition [e.g., *Okuda et al*., 1996; *Kibbey et al*., 2002; *Yan et al*., 2003; *Ramsburg and Pennell*, 2003; *Ramsburg et al*., 2004.].

Rates of TCE transformation within the NAPL [*Berge and Ramsburg,* 2010] are slower than those reported in most studies examining TCE reactivity within the aqueous phase (Table III-5, Fig. III-10).   Particles within the aqueous phase, however, have been shown to "burn out" leaving considerable amounts (perhaps as much as 35% wt) of the Fe^0 unreacted [*Liu et al.* 2007].   In contrast, rates of TCE dechlorination showed no indication of deactivation over the period investigated here, suggesting a sustained rate dechlorination within the NAPL may prove to be effective in consuming TCE over the longer term.
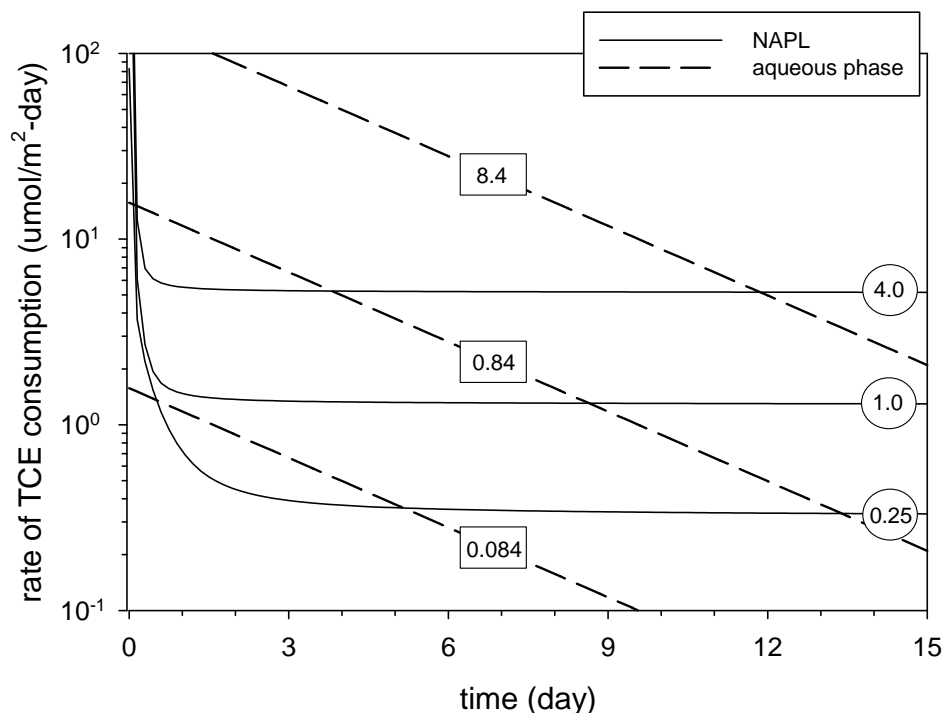
Figure III-10. Surface normalized rates of HR iron mediated consumption of TCE in the NAPL (solid lines) and aqueous phase (dashed lines) assuming constant concentrations of water and TCE, respectively. Aqueous phase rates decrease linearly due to first order deactivation.   Water concentrations (M) controlling TCE consumption in the NAPL are shown in the circles.   TCE concentrations (mM) controlling TCE consumption in the aqueous phase are shown in the rectangles.

Table III-5. Selected rate data for iron-mediated dechlorination of TCE within the aqueous phase.

Iron type	Reported k_{SA} (L/h-m^2)	Initial TCE concentration (mM)	Maximum observed rate[1] (umole TCE/day-m^2)	Source
HR	0.0011	0.027	0.7	Liu et al., 2007
HR	0.0012	0.11	3.2	Liu et al., 2007
HR	0.0012	0.46	13	Liu et al., 2007
HR	0.0004	2.21	21	Liu et al., 2005a
HR	0.00078	8.4	160	Liu et al., 2007
BH	0.002	0.03	1.4	Liu et al., 2005a
BH	0.0027	0.08	5.2	Wang et al., 2010
BH	0.089	0.08	170	Song and Carraway, 2008
BH-Pd (0.42% wt. Pd)	0.14	0.13	440	Meyer et al., 2009
BH-Pd (0.42% wt. Pd)	0.019	0.15	68	Meyer et al., 2009
BH-Pd (5% wt. Pd)	0.005	0.91	119	Lien and Zhang, 2007
BH-Ni (20% wt. Ni)	0.037	0.08	71	Tee et al., 2005
BH-Pd (Pd is 0.1% w/w Fe) particles coated with CMC	1.56	0.38	14000	He et al., 2007
Carbon particles with physisorbed CMC containing Fe-Pd: 0.8 % wt. CMC, 1 g/L Fe particles, 0.05% (w/w iron particles)	0.0447	0.152	160	Zhan et al., 2009
HR coated with various polyelectrolytes	0.00073 - 0.00014	8.4	28 - 150	Phenrat et al. 2009
BH coated with poly(methyl methacrylate)	0.00077	0.08	1.5	Wang et al., 2010

[1] maximum rates are calculated as the product of the initial TCE concentration and surface normalized rate constant (k_{SA}).

III.2. TRANSPORT AND REACTION OF NANOSCALE IRON IN A REPRESENTATIVE POROUS MEDIUM

III.2.1. RNIP Transport

Four experiments were performed, as described in Section I.2.1. to determine the distance RNIP would travel in water-saturated columns as a function of flow rate and grain diameter. Breakthrough of iron from the column packed with 20-30 mesh Ottawa sand was not observed after introducing the 2 g/L iron solution for 90 minutes at a flow rate of 2 mL/min (seepage velocity of 16.6 m/day, d_{50} Reynolds number of 0.05). After the 90 minute iron introduction period, the sand was removed from the column in 2.5 cm sections and each section was transferred to a 500 mL glass jar into which 400 mL of 1 N HCl solution were added. After allowing the acid solution to dissolve the iron particles overnight, the iron content of each of the six sand extracts was determined using the Ferrozine method. Results of the column sectioning and iron extraction procedure indicated that iron was retained within first 4 cm of the column, and was not present in the subsequent 11 cm of the column. Based on the distribution of iron in the column and the 90 minute introduction period, the estimated iron transport velocity was 2.7 cm/hr in this 20-30 mesh Ottawa sand at flow rate of 2 mL/min. Comparing the mass of iron introduced into the column to the amount recovered from the sectioning indicated that there was two times more iron in the column than estimated based on the concentration of iron in the influent sample collected prior to the 90 minute introduction period. This mass balance of 208% suggests that the influent iron concentration was not constant during the 90 minute introduction period, and that a single influent sample was not sufficient to determine the mass of iron delivered to the column.
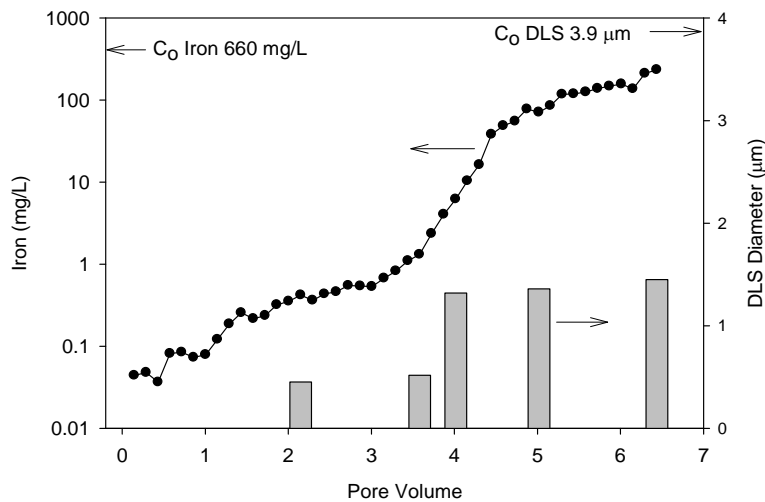
Figure III-11. Breakthrough of iron and size of iron particles from a 20-30 mesh Ottawa Sand column at a flow rate of 10 mL/min.

Increasing the flow rate to 10 mL/min (seepage velocity of 166 m/day, d_{50} Reynolds number of 0.23) caused RNIP to readily travel through the column and breakthrough within 2 pore volumes (60 mL) of initiating deliver, with visible breakthrough of the dark-colored RNIP suspension after 4 pore volumes (Figs. III-11 and III-12). Thus, the RNIP transport velocity increased to 80

43

cm/hr at an applied flow rate of 10 mL/min. Before dissolving the iron particles in effluent samples for subsequent Fe content analysis, the diameter of particles present in selected vials was determined using a Malvern Dynamic Light Scattering (DLS) Zetasizer. Prior to particle size analysis, the sample was diluted with an equal volume of de-ionized water and then sonicated for 1 minute in a Branson 1510 sonicator. Particles in the stock influent suspension had mean DLS diameter of 3.9 μm, rather than the 0.028 μm (28 nm) dimension provided by Toda America. Upon further inquiries, the manufacturer (Toda America) indicated that the 28 nm value corresponds to the dimension of the D110 crystal face as determined by x-ray diffraction (XRD) analysis, rather than the overall particle diameter, which are actually aggregates of the individual crystals. The DLS-measured diameter of RNIP particles eluting from the column after 2.15 and 3.58 pore volumes was approximately 0.5 μm, and then increased to 1.3 μm after 4 pore volumes. These diameters are four times smaller than particle diameters measured in the inlet stock suspension, suggesting that large particles were retained in the 20-30 mesh Ottawa sand. An image of a 10 g/L RNIP suspension, obtained with a Cytoviva-modified microscope, illustrates the formation of micron-scale RNIP clusters, consistent with the DLS measurements (Fig. III-13).

A longer duration experiment was completed with 20-30 mesh Ottawa sand at the flow rate at 2 mL/min to determine the number of pore volumes required for RNIP breakthrough and the distribution of iron over the entire length of the column. Upon entering the column, the RNIP suspension could be visually observed due to its dark color, and formed a distinct bank with a sharp interface, separated from the region of RNIP-free or "clean" sand (Fig. III-12). The front of the RNIP bank progressed through the sand column with continuous addition of RNIP suspension at a flow rate of 2 mL/min.   The velocity of RNIP bank movement was approximately 1 cm per pore volume, or 4 cm/hr. After introducing 29 pore volumes of RNIP suspension into the column, the RNIP bank reached the column outlet.

Additional experiments were conducted at higher RNIP concentrations. As observed in previous experiments (i.e., 2 g/L unmodified RNIP suspension), the RNIP particles aggregated upon entering the sand-filled column and formed a dark bank of RNIP. The RNIP bank moved through the column with continuous addition of RNIP suspension and eluted from the columns after 20.0 and 8.2 pore volumes at applied concentrations of 10 and 50 g/L, respectively. When the applied concentration was increased to 100 g/L, the RNIP particles formed a bank which moved approximately 6 cm into the 15 cm long column within 2 pore volumes; however, no further water flow through the column was possible thereafter, even at inlet pressures that approached 30 psig (2.1 meters of water). The concentration of iron eluting from the columns was equal to the inlet concentration (i.e., C over Co was equal to one) within 1.5 and 0.6 pore volumes for the 10 and 50 g/L experiments, respectively, indicating that this incremental increase in RNIP loading caused a sharpening of the iron bank front.

Figure III-12. Photographs of the RNIP bank in 20-30 mesh Ottawa sand column at a flow rate of 2mL/min.

Figure III-13. Image of RNIP aggregates (large clusters) in an aqueous suspension containing 100 nm diameter gold nanoparticles (small dots) obtained with a Cytoviva-modified microscope.

The average concentrations of iron in the bank were 35.4, 58.1, and 69.4 g/L for experiments performed with RNIP inlet concentrations of 10, 50, and 100 g/L, respectively. These concentrations are 2 to 4 times greater than that encountered for the previous experiments (performed with an RNIP inlet concentration of 2 g/L). The hypothesis that RNIP bank movement occurred after reaching a critical iron concentration of between 10 and 20 g/L, however, was not supported by these results. Rather than remaining constant, the iron concentration increased and was correlated (r^2 = 0.99) to the logarithm of the RNIP inlet concentration. Thus, increases in RNIP inlet concentration caused increases in the iron content of the RNIP bank as opposed to reaching a limiting or maximum concentration. The increase in iron concentration of the bank also coincided with increases in the rate of bank movement. For an injected concentration of 10 g/L, the bank moved at 4 cm/hr, which was identical to the rate determined in previous experiments with the injected concentration at 2 g/L. Increasing the injected concentration to 50 and 100 g/L increased the rate of bank movement to 7 and 11 cm/hr, respectively.

The inlet pressure during the injection of the high-concentration RNIP solutions was determined using a calibrated pressure transducer installed in-line between the peristaltic pump and the column inlet, and was recorded at 10 second intervals using a Campbell Scientific data logger. The pressure at the column inlet steadily increased with the number of pore volumes injected for all injection concentrations. For example, with an RNIP injection concentration of 10 g/L, the pressure increased to a maximum value of 0.9 psig (63 cm of water) at the point in time when RNIP eluted from the column. Following RNIP breakthrough, at least two pore volumes of clean water were pumped through the column and the pressure decreased from 0.9 to 0.6 psig (42 cm of water). For an RNIP injection concentration of 50 g/L, the pressure steadily increased to 10 psig (700 cm of water) at the point of RNIP breakthrough, and subsequently decreased to 7 psig (500 cm of water) during the subsequent water flood. For the experiment conducted with an injection concentration of 100 g/L, the inlet pressure increased to 30 psig (2.1 meters of water) prior to elution of RNIP from the column and clean water would not flow through the column at pressures up to 30 psig.

The results of the high-concentration RNIP injection experiments suggest that the movement of the RNIP bank is controlled by pore throat diameters of the 20-30 mesh Ottawa sand. Increasing the injection concentration led to increases in the iron content of the bank and pressure required to move water through the column. Thus, we hypothesize that as additional RNIP was introduced into the column, the pore throats were blocked, resulting in an increase in the resistance to water flow. This hypothesis was tested by pumping a 10 g/L RNIP suspension through a column filled with lower permeability Federal Fine Ottawa sand (30-140 mesh). As was observed with the 20-30 mesh Ottawa sand-filled columns, the RNIP formed a dark bank after entering the column with Federal Fine sand. However, the column inlet pressure increased to 30 psig (2.1 m of water) after pumping 9 pore volumes of RNIP suspension into the column and the iron bank had progressed only 1.5 cm into the 15 cm long column. This finding clearly indicates that decreasing the sand grain diameter decreased the travel distance for the 10 g/L RNIP suspension, consistent with pore throat blockage by the accumulation of RNIP.

Phenrat, et al. [2007] reported that the aggregation of RNIP particles was affected by magnetic attractive forces, and incorporated these forces into an extended Derjaguin-Landau-Verwey

Overbeek (DLVO) theory to show that there was no energy barrier to RNIP aggregation after accounting for magnetic interactions. *Phenrat et al.* [2007] also measured the magnetic susceptibility (i.e., the degree of magnetization in response to a magnetic field) of an RNIP suspension and found that it was greater than was observed for an equivalent suspension of magnetite. Thus, magnetic particle-particle interactions should be accounted for in models developed to describe RNIP self-aggregation and transport in porous media. This was evident in experiments where the formation of a distinct RNIP bank with a sharp interface was observed, rather than an unstable interface indicative of RNIP fingering. Initially, an unstable interface was expected since the overlying RNIP fluid possessed a greater density than the underlying RNIP-free fluid. The lack of fingering suggests that magnetic particle-particle interaction forces are stronger than the gravitational forces that would cause the more dense RNIP solution to form an unstable interface. Although *Phenrat et al*. [2007] incorporated magnetic interactions of RNIP solutions, the study of fluids with magnetic particles possessing permanent dipole moments, referred to as dipole fluids, has a rich history [*Range and Klapp*, 2005]. Dipole-dipole interactions result in complex non-linear behaviors, such as the spontaneous formation of aggregates in the absence of a magnetic field for magnetic particles with diameters of greater than 10 nm, regardless of surface coatings [*Klokkenburg et al.*, 2004].

The first phase in RNIP bank formation is thought to involve RNIP particle aggregation upon entering the water-saturated, sand-filled column. With further addition of RNIP particles, aggregates located within soil pores continue to grow in size until a critical iron concentration is reached. Based on the retention profile obtained after RNIP breakthrough from column experiments, the critical iron concentration was estimated to range from 10 to 24 g/L. Once the critical concentration of RNIP was reached, the bank continued to move through the sand filled column. Thus, the bank only moved after the addition of more RNIP mass, and no bank migration was observed visually without further addition of RNIP. The mechanisms involved in RNIP bank transport are less clear. Highly viscous, rigid-suspensions have been observed in previous work with magnetite suspensions [*Popplewell et al.*, 1995]. Such rigid suspensions were formed when the volumetric solids fraction exceeded a critical value of 0.74 for coated magnetic particles, while a lower value was observed for suspensions of magnetic particles that tend to aggregate. The volumetric RNIP fraction, based on the critical concentrations between 10 and 24 grams/L, ranged from 0.00026 to 0.0091. These volumetric fractions are orders of magnitude lower than the critical value of 0.74 corresponding to the formation of a rigid suspension. Thus, rather than forming a rigid suspension, RNIP is hypothesized to self-assemble into complex chains of particles that move by either 1) single particle attachment to and detachment from pore-entrapped RNIP aggregates or 2) deformation and transport of the RNIP aggregates through sand pores. Recent reports from the dipolar fluids literature suggest that aggregates are dynamic structures, where particles can attach and detach as long as the aggregates are not subject to oxidation [*Klokkenburg et al.*, 2004].

III.2.2. Modified RNIP Transport

While the uncoated or bare RNIP formed a bank of dark-colored iron (Fig. III-12), the deposition of mRNIP was less uniform and appeared to form localized regions of high retention within pore bodies, especially near the column outlet (Fig. III-14). Even though the dark colored mRNIP

appeared to move through the column faster than the bare RNIP, there was only a slight improvement in the time for breakthrough with 25 pore volumes of flushing required for mRNIP, compared to the 29 pore volumes required for breakthrough of bare RNIP. The mass of iron retained within the mRNIP column after 25 pore volumes was 71 mg as compared to the 197 mg of iron in the bare RNIP column after 29 pore volumes.
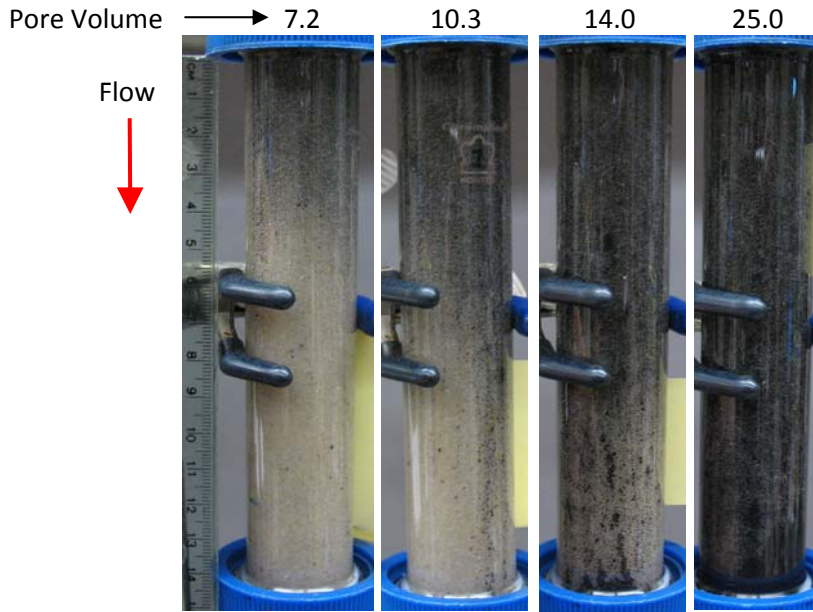
Figure III-14. Photographs of the polymer-coated mRNIP in 20-30 mesh Ottawa sand filled column operated at a flow rate of 2 mL per min.

In the presence of the 1,000 mg/L (0.1%) Tween 80, the RNIP formed a dark bank, similar to that observed with the bare RNIP alone. However, the RNIP-Tween 80 bank now moved at a velocity of 4 cm per pore volume or 16 cm/hr, as compared to 4 cm/hr for the RNIP alone. Iron breakthrough occurred after 5 pore volumes with the RNIP-Tween 80 suspension and effluent concentrations varied from 300 to 3,000 mg iron/L. The rapid iron breakthrough also corresponded to an increase in iron loading as the mass of iron within the Tween80-RNIP column was 640 mg versus the 197 mg measured in the bare RNIP column experiment. Thus, the addition of Tween 80, at a concentration of 1,000 mg/L, substantially (3-fold) increased both the movement of RNIP through the 20-30 mesh Ottawa sand filled column and the mass of iron retained within the column. A summary of the RNIP delivery results are presented in Table III-6.

Table III-6. Comparison of bare (unmodified), polymer-modified, and surfactant-stabilized RNIP delivery in water-saturated 20-30 mesh Ottawa sand.

RNIP Suspesion	Pore Volumes When Breakthrough Occurred (1 PV ~ 30 mL)	Mass of Iron Retained in Column at Breakthrough (mg)
RNIP alone	29.0	197.0
Polymer-modified RNIP	25.0	71.0
RNIP + 0.1% Tween 80	5.0	640.0

III.2.3. Z-Loy Column Experiments

Experimental conditions and measured observations from two Z-Loy transport experiments are presented in Table III-7 and Fig. III-15 - III-17. Examination of effluent iron concentrations presented in Fig. III-15 suggests that approximately 97% of the injected iron mass was retained within the sandy medium during Experiment A. This is confirmed by inspection of the retention profile presented in Fig. III-16 (65% was retained within the first 2-cm). Gas formation within the column was observed during Z-Loy injection. It is hypothesized that gas production may be one mechanism that inhibited Z-Loy transport. Preliminary results from batch experiments aimed at evaluating the source of the gas formation suggest that hydrogen production does occur and may account for a portion of the gas bubbles observed in Experiment A. Increasing the flow rate for Experiment B resulted in a decrease in the amount of retention of the Z-Loy product, with 84% of the injected iron retained within the sandy medium. A significant amount of gas production was also observed during Experiment B. Note that production of hydrogen gas could be advantageous if Z-Loy injection were combined with biostimulation or bioaugmentation approaches.
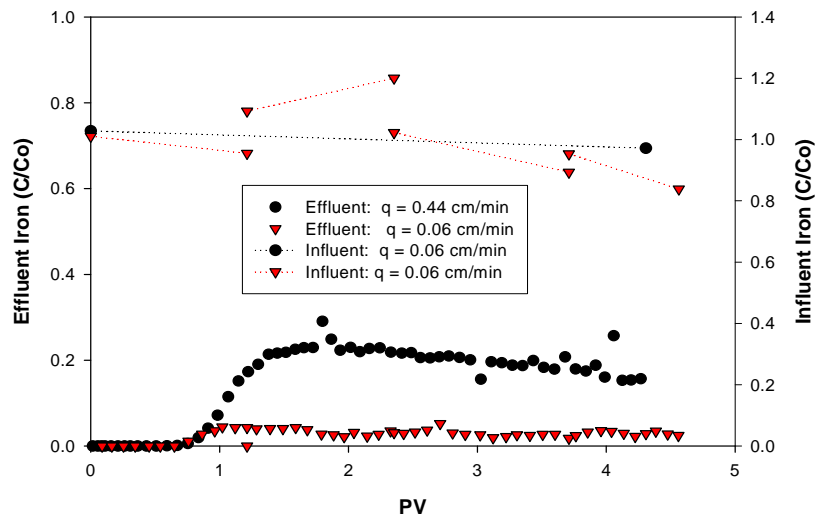
Figure III-15. Effluent and influent iron concentrations from Z-Loy experiments.
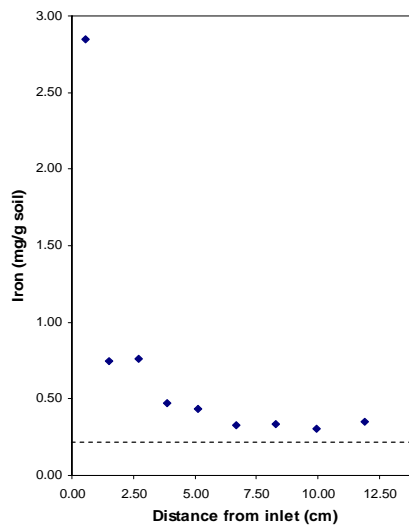
Figure III-16. Deposition profile for Z-Loy column experiment A. Dashed line represents the limit of detection for the column extraction procedure.
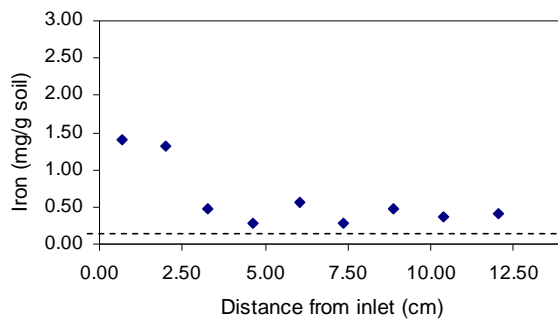
Figure III-17 Deposition profile for Z-Loy column experiment B. Dashed line represents the limit of detection for the column extraction procedure.

Table III-7 Z-Loy Column Transport Experimental Conditions.

	Experiment A	Experiment B
Ottawa Sand Type	Ottawa 20-30 Mesh	Ottawa 20-30 Mesh
Permeability (cm^2)	3.1×10^{-6}	3.1×10^{-6}
Porosity (-)	0.36	0.36
Packed Length (cm)	12.44	12.72
Pore Volume (mL)	81.98	83.08
Darcy Velocity (cm/min)	0.06	0.44

III.2.4. Emulsion Transport and Reaction

The transport of the surfactant stabilized emulsions was thoroughly characterized and is reported in *Crocker et al.*[2008] and *Berge and Ramsburg* [2009]. Key findings of these two studies are summarized here. In addition, results from emulsion transport studies conducted with entrapped TCE-NAPL are included below.

III.2.4.1. Emulsion Transport
Results from the *Crocker et al.* [2008] study demonstrate the ability to formulate kinetically stable oil-in-water emulsions containing iron. The emulsions consisted of tallow oil droplets smaller than estimated soil pore diameters and contain no visible iron (under light microscopy) agglomerates. Importantly, results shown in Fig. III-18 suggest that increased head loss during emulsion flushing is the result of fluid viscosity rather than extensive pore-clogging. Note that the pressure increases decay as the pulse of emulsion moves through the medium. Results from these preliminary experiments justified further research related to emulsion-based encapsulation of reactive iron.
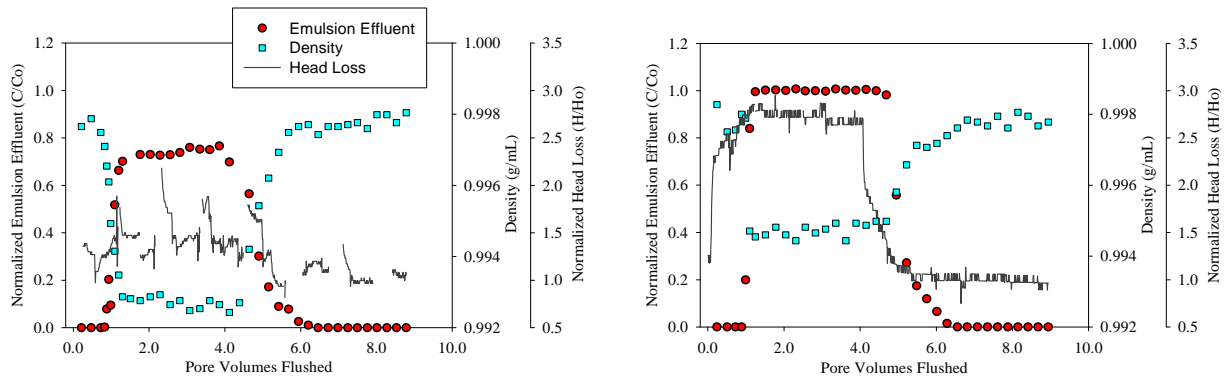
Figure III-18. Density and relative concentration of effluent samples plotted with head loss data for column experiments conducted with iron-free emulsion (left) and iron-laden emulsion (right). [*Crocker et al.*, 2008]

Berge and Ramsburg [2009] conducted a more detailed study that demonstrates the benefits of encapsulating iron particles within soybean oil droplets. Breakthrough curves and post-experiment column extractions from column experiments conducted with medium and fine sands suggest little emulsion retention (<0.20% wt.) at a Darcy velocity of 0.4 m/day. Shown in Fig. III-19 are results from two representative column experiments (see *Berge and Ramsburg* [2009] for complete set of experiments). Velocity is a key factor when assessing iron delivery. Most studies have employ velocities that will be difficult to attain in shallow unconfined aquifers (see Supporting Information in *Berge and Ramsburg* [2009]). It is here that the emulsion encapsulation offers a considerable advance. The findings published in *Berge and Ramsburg* [2009] demonstrate that emulsion encapsulation is a promising method for delivery of iron particles. Moreover the techniques are easily adapted for encapsulation of other nano- to sub-micron scale reactive particles.
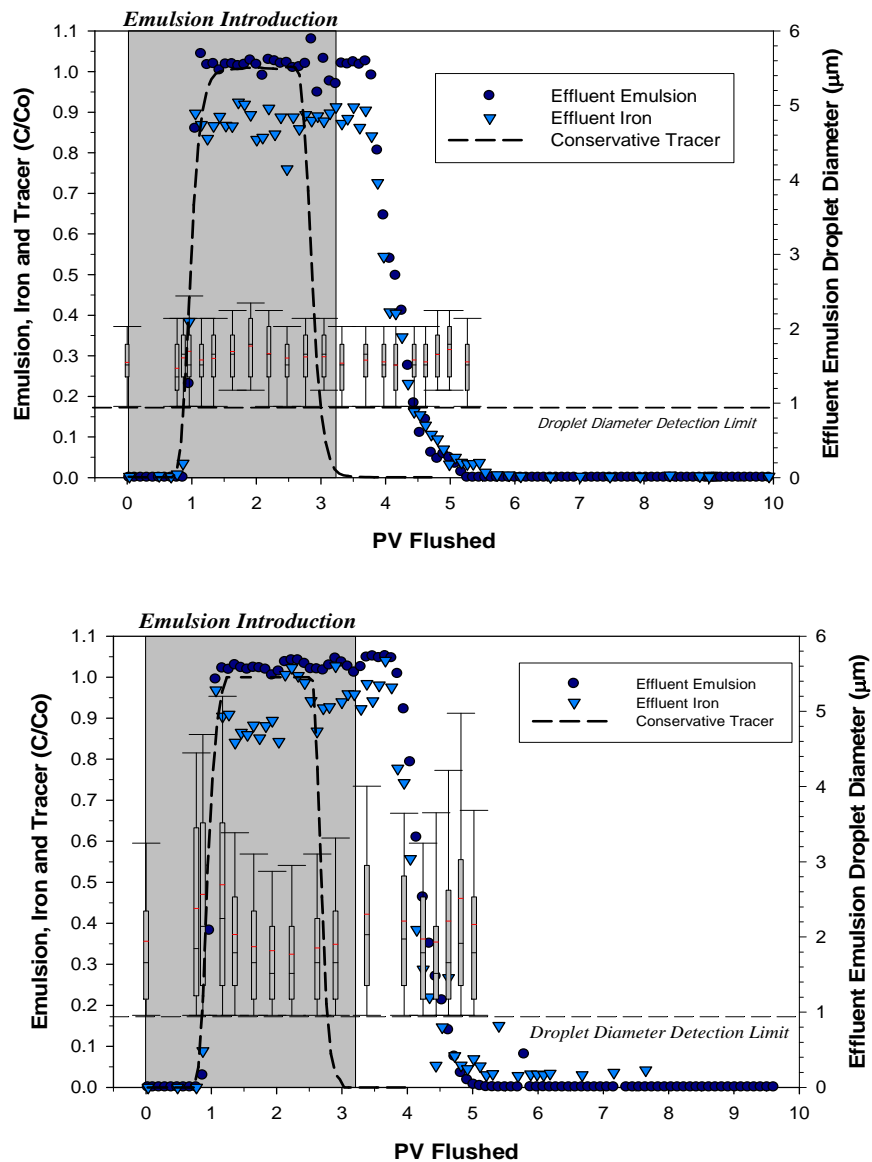
Figure III-19 Emulsion transport results for Experiments I (top) and II (bottom). Breakthrough curves for a bromide tracer (prior to the introduction of emulsion), emulsion, and iron. Box and whisker plots represent emulsion droplet size distribution data for effluent samples having quantifiable emulsion content. Red lines in the box and whisker plot indicate the mean droplet size, black lines indicate the median droplet size, boxes represent 25% and 75% of the data, and whiskers represent 10% and 90% confidence intervals. [*Berge and Ramsburg*, 2009]

III.2.4.2. Emulsion Transport in Presence of Entrapped DNAPL

Results of the emulsion flushing experiment in the presence of DNAPL are presented in Fig. III-20. Inspection of the Figure reveals that 55% of the entrapped TCE was removed from the column during the emulsion flush. Emulsification of TCE (i.e., incorporation of TCE into the oil-phase of the emulsion) is hypothesized to be the primary removal mechanism. Approximately

96 and 84% of emulsion and iron, respectively, were recovered in the column effluent, demonstrating that the emulsion, and the iron component of the emulsion, can be transported in sandy media containing DNAPL.

Upon completion of the experiment and a seven day shut in period, sand sections were removed from the column in 1-cm intervals and placed into approximately 100mL of acetone. Liquid samples were removed and analyzed for TCE concentrations and iron contents. Extracts taken during column sectioning indicate some TCE reduction occurred, as evidenced by small masses of ethene, butane, pentene and propane. Quantification of the exact mass of TCE reduced, however, is complicated by the potential for volatile losses of gaseous products when opening the column and mixing the sand with acetone (extraction solvent).
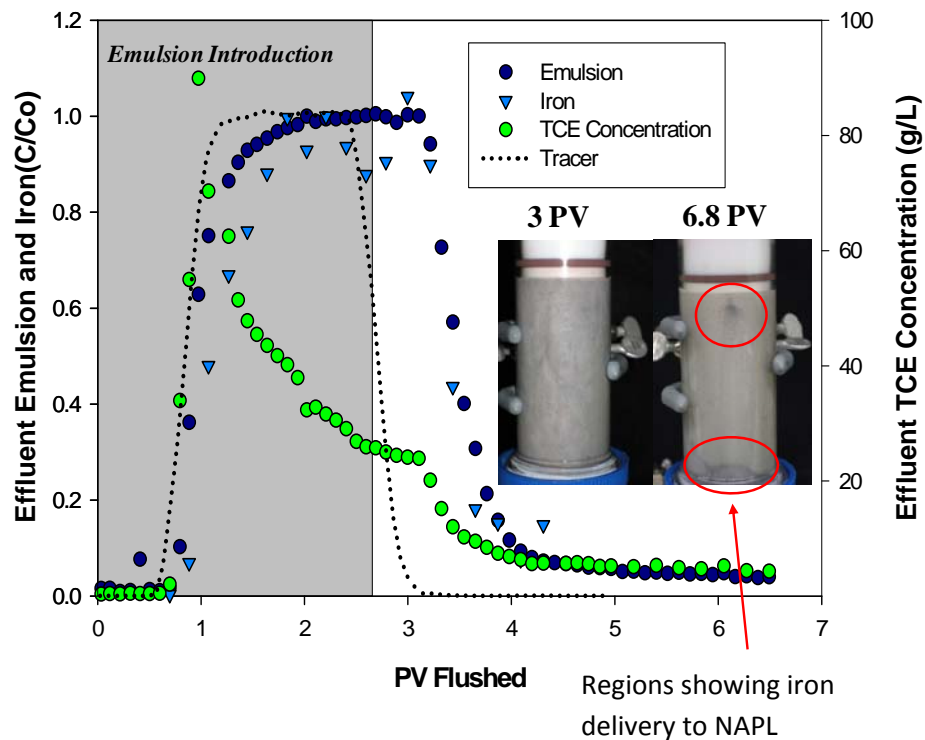
Figure III-20. Results from 1-D column experiment containing entrapped TCE.

III.2.4.3. Potential for NAPL Mobilization during Iron Delivery

The density, viscosity and interfacial tension with TCE of each commercially-available product and emulsions containing iron (only those exhibiting stability greater than 1 hr) were measured (Table III-8) and used to assess the potential for DNAPL mobilization during product delivery. Results of the total trapping number analysis suggest that injection of iron-containing emulsions with viscosities <3.0 cP present little potential for mobilization of TCE-DNAPL entrapped within fine-grained sand (intrinsic permeability = 2.8 x 10^{-8} cm^2) and medium-grained sands (intrinsic permeability = 4.69 x 10^{-7} cm^2) for Darcy velocities up to approximately 7 and 0.4 m/day, respectively, as illustrated in Fig. III-21. Results from a column experiment in which an

emulsion was injected to a media containing entrapped DNAPL confirm this analysis. Results from the trapping number analysis also suggests that injection of the emulsions generated in Task 1, when delivered in coarse-grained sands (Fig. III-21, blue square symbols) may cause mobilization of entrapped (residual) NAPLs. Trapping number analysis results also suggest that emulsions having viscosities near 10 cP (i.e., OA coated emulsion) require more careful design of site hydraulics to minimize the potential for DNAPL migration. A trapping number analysis was conducted for all iron delivery approaches in which physical/chemical properties were measured (Table III-8). A comparison of delivery techniques reveals that Z-Loy exhibits the least potential for DNAPL mobilization.

Table III-8. Measured properties relevant to flow for zero valent iron delivery systems.

Product	Density (g/mL)	Interfacial Tension (dynes/cm)*	Viscosity (cP)
Water	0.998	35	1.0
10% Soy Oil, no RNIP	0.995 ± 0.002	16.9 ± 0.13	2.3
Z-Loy Product (OnMaterials)	1.01 ± 0.01	23.6 ± 0.32	1.5
MA Coated RNIP Emulsion: 6.2% Tween 20, 2% Span 80	1.00 ± 0.01	7.54 ± 0.24	NM
OT Coated RNIP Emulsion: 6.1% Tween 20, 2% Span 80	1.00 ± 0.01	7.07 ± 0.14	2.8
Oleic Acid Coated RNIP Emulsion: 6.4% F108, 5.3% Oleic Acid	0.996 ± 0.003	8.46 ± 0.13	9.3
Modified RNIP (Toda America), As Delivered	1.15 ± 0.05	21.4 ± 1.08**	7.3
Modified RNIP (Toda America), 2% solids	1.01 ± 0.01	NM	1.3
Bare RNIP (Toda America)	1.25 ± 0.03	NM	NM
EZVI [*Quinn et al.*, 2005]	1.1	33.5	1940

*with TCE; **supernatant only; NM=not measured
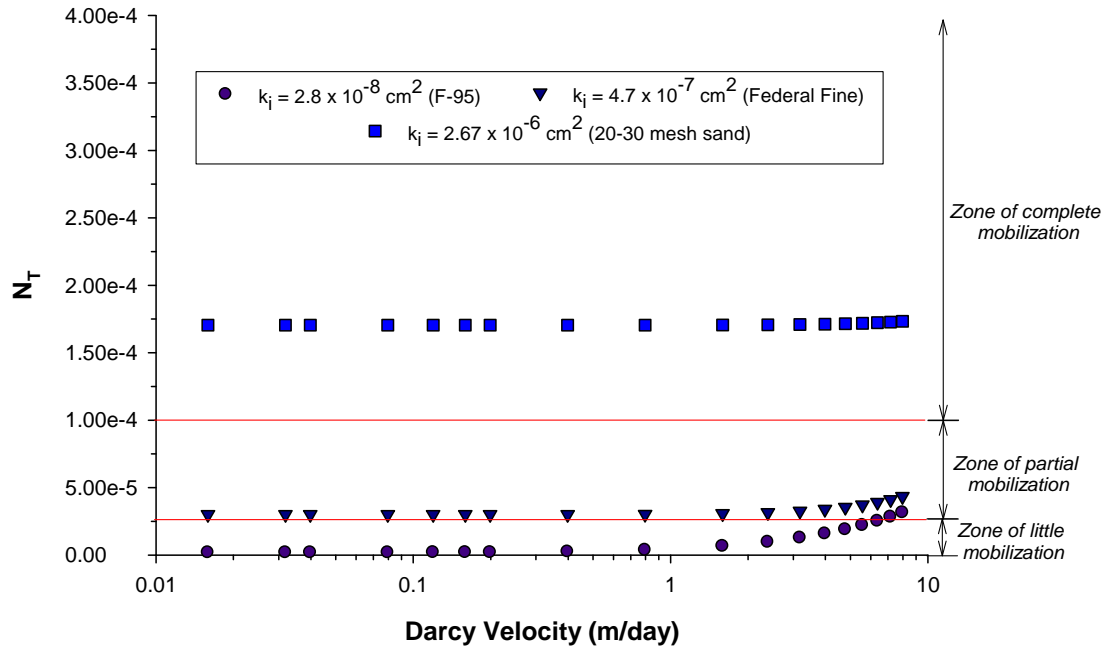
Figure III-21. Trapping number analysis for an emulsion (composition: 10% wt. soybean oil, 2% wt. Span 80, 6.2% wt. Tween 20, and 0.25% wt. OT-coated RNIP) with a viscosity <3cP.
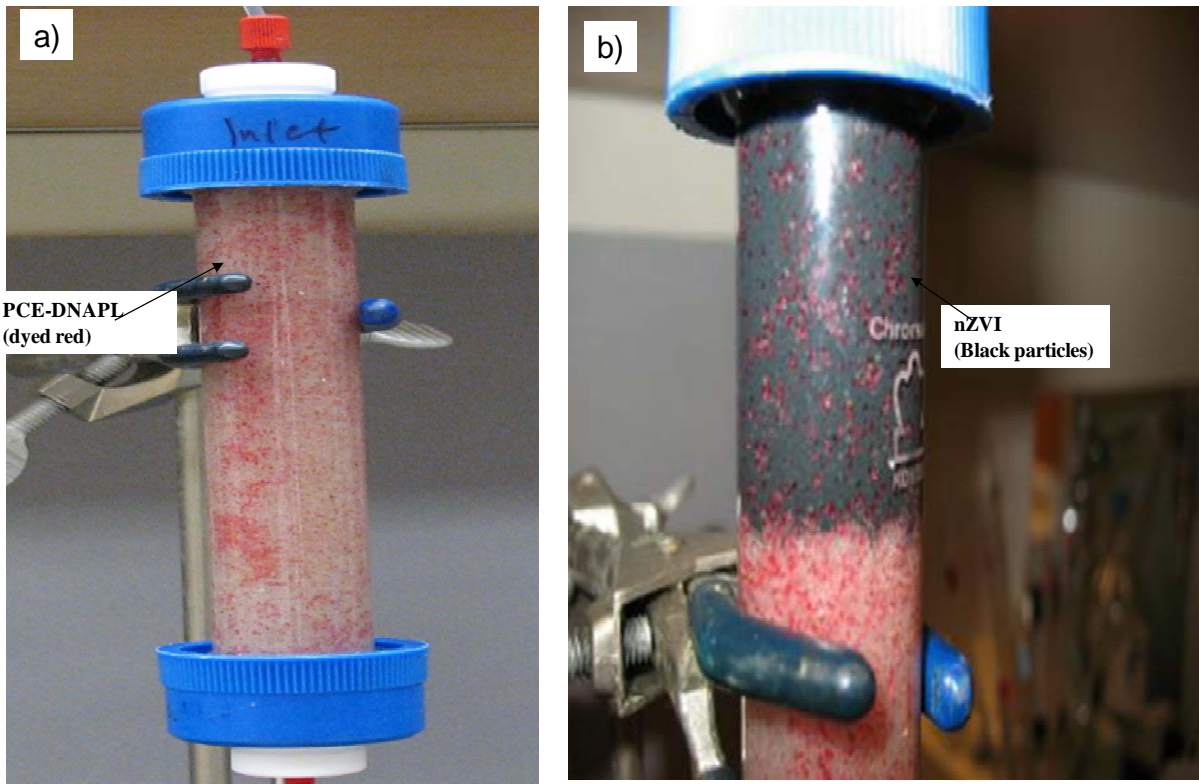
Figure III-22. Photographs of 20-30 mesh Ottawa sand column containing PCE-DNAPL (dyed red) at residual saturation (A) and during the injection of unmodified RNIP suspension (B).

During injection of the unmodified RNIP suspension into a column containing PCE-DNAPL at residual saturation, a small fraction (< 2 %) of the entrapped PCE-DNAPL was displaced from the column. As shown in Fig. III-22, the unmodified RNIP suspension migrated through the column leaving the entrapped PCE-DNAPL droplets (dyed red) in place, with was no visual indication of migration or displacement from the column. When the 10 g/L RNIP suspension, stabilized with 1% (10,000 mg/L) Tween 80, was introduced into a column containing residual PCE-DNAPL a continuous black pulse of RNIP suspension was observed, similar to that observed during RNIP delivery. However, approximately 10% of the residual PCE-DNAPL was displaced from the column. This result was attributed to a reduction in interfacial tension between the surfactant-containing RNIP suspension and PCE-DNAPL relative to the unmodified RNIP suspension. When the concentration of Tween 80 in the RNIP suspension was reduced to 0.1% (1,000 mg/L), less than 7% of the entrapped PCE-DNAPL was displaced from the column. These findings indicate that while the use of surfactant-stabilized RNIP suspensions may improve delivery rate and retention (see Subtask 2.1), the potential exists for partial mobilization of entrapped PCE-DNAPL during RNIP delivery. Hence, a combination of theoretical analysis and laboratory testing with site specific materials and delivery suspension should be undertaken to minimize the potential for NAPL mobilization during the delivery of nanoscale iron suspensions.

Delivery of remedial amendments within DNAPL source zones requires consideration of several important physical properties – density, viscosity and interfacial tension. Because small differences in density between the injected and resident fluids can result in gravity over- or under-ride of the zone targeted for treatment [e.g., *Taylor et al*., 2004] emulsions represents a compromise between delivery and iron loading. Additional iron loading increases density and consequently, the complexity of any hydraulic design aimed at uniformly distributing the iron within the subsurface. Measurement of the viscosity of the emulsion as a function of shear rate (0.4-100 s^{-1}) at 20.00 ±0.01 ºC suggests the emulsions may be weakly shear thinning, but that a Newtonian assumption may provide a reasonable approximation at shear rates expected in porous media (Table III-9). Within DNAPL source zones, the combined influence of viscosity, density and interfacial tension on DNAPL mobility must be considered thought the use of the total trapping number [*Pennell et al*., 1996].

Assuming that the NAPL phase will be mobilized when N_T is above a critical value $N_{T,crit}$, the corresponding critical Darcy velocity can be expressed as:

$$q_{w,crit} = \frac{1}{\mu_w}\sqrt{\left(\sigma_{ow}\cos\theta\right)^2 N_{T,crit}^2 - \left(\Delta\rho g k_{rw} k\right)^2} \tag{22}$$

Eq. 22 indicates that a high IFT and low viscosity will increase the critical velocity, below which the NAPL phase is less likely to be mobilized. The limiting permeability value k_0 for each reagent system can be deduced from Eq. (22):

$$k_0 = \frac{\sigma_{ow}\cos\theta N_{T,crit}}{\Delta\rho g k_{rw} k} \tag{23}$$

The potential for mobilization (as determined using the total trapping number of *Pennell et al.* [1996]) can be visualized in a novel format shown in Fig. III-23. The range of intrinsic permeability shown on the x-axis represents permeability for which injection/flushing is most applicable (silty sands to gravel). The utility of Fig. III-23a lies in the regions defined under the elbow curves that represent conditions consistent with limited ($N_T=2 \times 10^{-5}$) and complete ($N_T=1 \times 10^{-4}$) DNAPL mobilization. In general, the horizontal extent of the curve is related to the IFT between the solution and NAPL (higher IFT solutions are better suited for higher permeability formations), while the vertical extent of the curve is related to the ratio of IFT to the viscosity of the flushing solution (higher viscosity solutions are restricted to using lower treatment velocities). The calculations shown in Fig. III-30b suggest that the GA emulsion has potential for broad applicability within DNAPL source zones (as determined by the area under the curve).

Table III-9. Data used in total trapping number analyses (at $22 \pm 3 \, ^{\circ}C$).

System	Density (g/mL)	Viscosity (mPa·s)	Interfacial Tension[a] (N/m)
GA stabilized emulsion	1.03±0.01	16.8±0.1	30.75±0.02
Surfactant-stabilized, iron containing, oil-in-water emulsion [*Berge and Ramsburg*, 2009]	1.00±0.03	2.4±0.5	7.07±0.14
Surfactant-stabilized macroemulsion for density-modified displacement of TCE [*Ramsburg et al.*, 2003]	0.979±0.0001	2.52±0.05	7.2±0.4
Surfactant Flood for Mobilization (3.3% wt.) Aerosol MA-90 + 8% (wt.) 2-propanol+4g/L NaCl [*Suchomel et al.*, 2007]	0.994±0.001	1.64± 0.02	0.19
Surfactant Flood for Solubilization (4% wt.) Tween 80 + 0.5 g/L CaCl$_2$ [*Suchomel et al.*, 2007]	1.002±0.001	1.29± 0.04	10.4± 0.08
Emulsified Zero Valent Iron [*Quinn et al.*, 2005]	1.1	1942	37.5

[a] with TCE

Table III-10. Parameters utilized in total trapping number calculations.

Parameter	Value
Relative Permeability	1
TCE-DNAPL Density	1.46 g/mL
Contact angle	0
Flow direction	horizontal
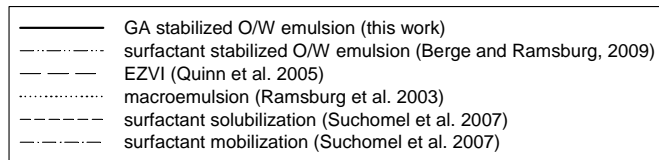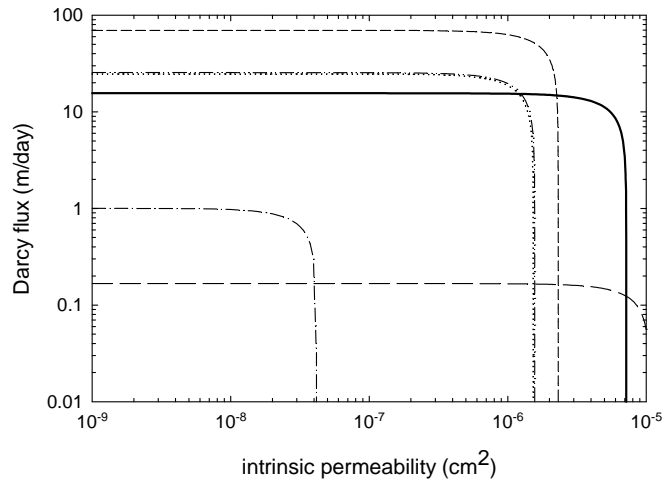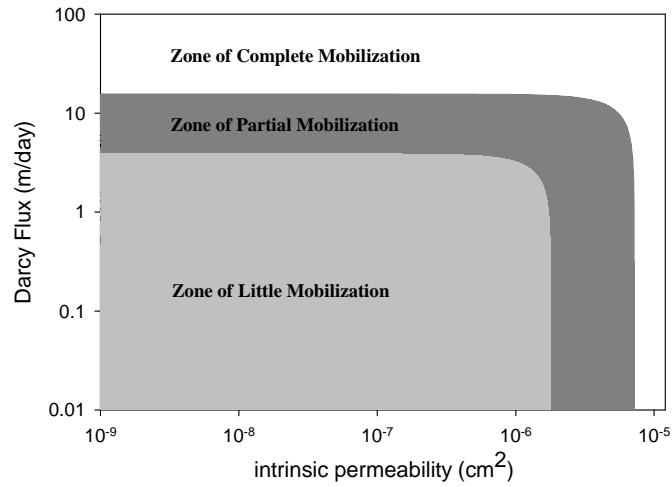
Figure III-23. Trapping number regions (a) defining zones of little, no and complete mobilization for the GA emulsion and (b) showing the line representing complete mobilization for several flushing solutions.

III.2.5. Reactivity and Transport of Delivery Systems in Columns Containing Entrapped DNAPL

A series of five column experiments was conducted to experimentally evaluate the capacity of emplaced nZVI to react with PCE-DNAPL in a porous medium. The column experiments were designed to represent the portion of a DNAPL source zone at residual saturation and to test whether nZVI, delivered as an aqueous suspension, would have sufficient reactivity to transform PCE to ethene. Here, it should be noted that the majority of the research on dehalogenation reactions mediated by ZVI has involved batch studies that employ dissolved contaminant concentrations and total mass loadings that are much lower than those typically observed within DNAPL source zones, specifically less than < 20 mg/L [e.g., *Arnold and Roberts*, 2000; *Doong and Lai*, 2005; *Dries et al.*, 2004; *Kim et al.*, 2008; *Liu and Lowry*, 2006; *Schrick et al.*, 2002; *Shin et al.*, 2008; *Wang et al.*, 2010; *Zhan et al.*, 2009]. Similarly, field-scale nZVI demonstration projects have focused on the treatment of relatively dilute dissolved phase contaminant plumes, using an groundwater extraction/reinjection system [*Henn and Waddill*, 2006] and direct injection of nZVI under gravity feed [*Elliot and Zhang*, 2001], with initial TCE concentrations of less than 20 mg/L and 1 mg/L, respectively. With the exception of *Lui et al.* [2005] (290 mg/L dissolved TCE), no published studies examined the effectiveness of nZVI at higher contaminant concentrations that would be anticipated to occur within or in close proximity to a DNAPL source zone. Thus, the experiments undertaken here represent the first effort to directly evaluate the potential effectiveness of using nZVI to treat a DNAPL source zone at residual saturation. A total of 5 column studies were conducted with different types of nZVI, including a baseline experiment with unmodified RNIP (Toda America), surface modified nZVI, and surfactant (Tween 80)-stabilized RNIP.

The nZVI delivery (60 g Fe/L aqueous suspension) phase of the column experiment was carried out at a constant flow rate of 2 mL/min and was associated with minimal displacement of PCE-DNAPL from the column (Fig. III-24). Fingering was not observed and the overall process resulted in the establishment of a uniform distribution of both nZVI and residual PCE DNAPL throughout the column. Following nZVI emplacement, 267 PVs of a 3.5mM $CaCl_2$ aqueous solution were flushed through the column. No displacement of RNIP particles or PCE-DNAPL was observed in column effluent samples during this water flushing phase. Fig. III-25 presents effluent concentrations of organic constituents measured during the first 170 PVs aqueous solution flushing which were used for model validation since only one additional data point was collected at 267 PVs. Despite the presence of nZVI, no substantial reductions in PCE effluent concentrations was observed during the experiment, i.e., a near equilibrium solubility concentration of PCE (average effluent concentration of 240.2 mg/L) was measured. Significant ethene evolution (average concentration of 18.2 mg/L) was observed, indicating that nZVI was reacting with PCE. Other relevant daughter products, including TCE, cis-DCE, and vinyl chloride were not detected in any of the effluent samples. Additional column experiments conducted using the same or similar nZVI material yielded similar results, including effluent PCE concentrations at or near the aqueous solubility limit and production of ethene at concentrations ranging from 10 to 30 mg/L. Only intermittent emergence of gas bubbles was observed during the experiments, suggesting that hydrogen gas production via a corrosion reaction of nZVI with water was minimal. Limited gas production at high PCE concentrations is consistent with the findings of *Liu and Lowry* [2006], who reported a substantial decrease in H_2 gas evolution with increasing organic contaminant concentrations (above 10 mg/L for TCE). At

the conclusion of the column experiment, approximately 20% of in the initial PCE-DNAPL mass remained in the column.

During the RNIP introduction period, the concentration of PCE remained near its aqueous solubility of approximately 200 mg per liter, while the concentration of ethene steadily increased, reaching a maximum value of 10 mg per liter. The inlet pressures during RNIP delivery to the column containing entrapped PCE were 1.6 psig as compared to the 0.9 psig determined while introducing RNIP into an identically prepared PCE-free column. This result provides additional evidence supporting the theory that the pore throat diameter controls the RNIP bank movement since entrapped PCE droplets typically reside in the pore body and act to lower the effective permeability by reducing the cross-sectional area available for water flow. After the column was filled with RNIP, clean water containing 3.5 mM calcium chloride as a background electrolyte was continuously pumped through the column at a flow rate of 0.25 mL per minute for 238 pore volumes. The concentration of PCE remained at or near the aqueous solubility value (ca. 200-250 mg/L) throughout the water flood, while the concentration of ethene was also relatively constant at 35 mg per liter. Following 238 pore volumes of water injection, the column was flushed with isopropyl alcohol to recover any residual PCE-DNAPL remaining in the column. Of the 1.5 mL neat PCE initially present in the column, 75 percent was removed by solubilization in the effluent during the 238 pore volumes, 19 percent remained in the column as neat PCE, and only 4 percent was removed by transformation to ethene (Fig. III-25). These experimental results suggest that introducing RNIP into a subsurface region containing residual DNAPL will not result in substantial contaminant transformation to ethene, and that the fraction PCE mass degraded may be insignificant compared to the amount removed due to dissolution in water.

In a previous column study we found that the addition of Tween 80, a nonionic surfactant, resulted in a three-fold increase in the rate of RNIP transport through 20-30 mesh Ottawa sand and increased the amount of RNIP retained in the column. Therefore, an additional column experiment was performed to evaluate the delivery and reactivity of surfactant (Tween 80)-stabilized reactive nano-iron particles (S-RNIP) in columns containing residual PCE-DNAPL. To prepare a 10 g/L suspension of S-RNIP in 1 percent Tween 80, 1 g of Tween 80 was mixed with 40 mL of RNIP (Toda America, Lot no. 70601) in 1 L of de-aired, DI water containing 10 mM sodium bicarbonate. For this experiment, sodium bicarbonate was used as the background electrolyte instead of calcium chloride to minimize oxidation of zero valent iron by chloride ions. Approximately 30 mL of neat PCE was introduced into a column containing water-saturated 20-30 mesh Ottawa sand. Following displacement of mobile PCE-DNAPL by water flushing, 4.6 mL of PCE-DNAPL remained in the column, representing a PCE-DNAPL residual saturation 15.5 percent.

61
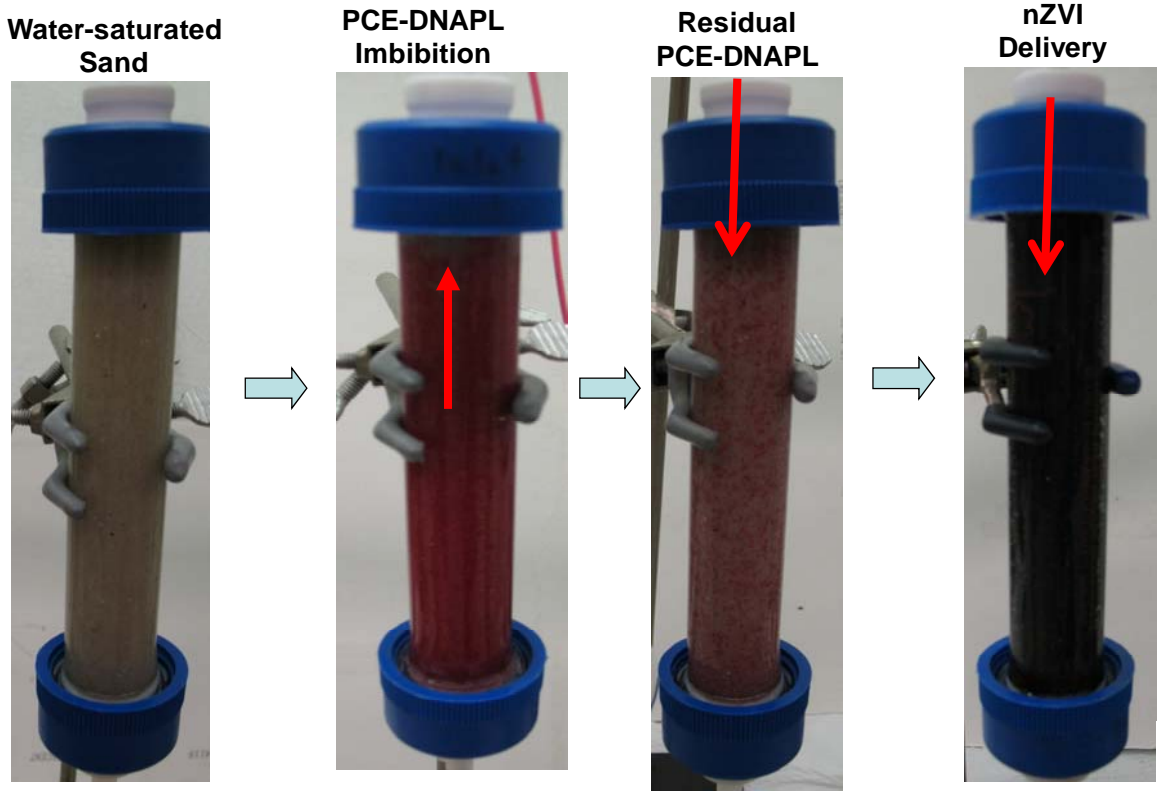
Figure III-24. Photographs illustrating the experimental procedure to create a uniform distribution of residual PCE-DNAPL and deliver nZVI suspensions.
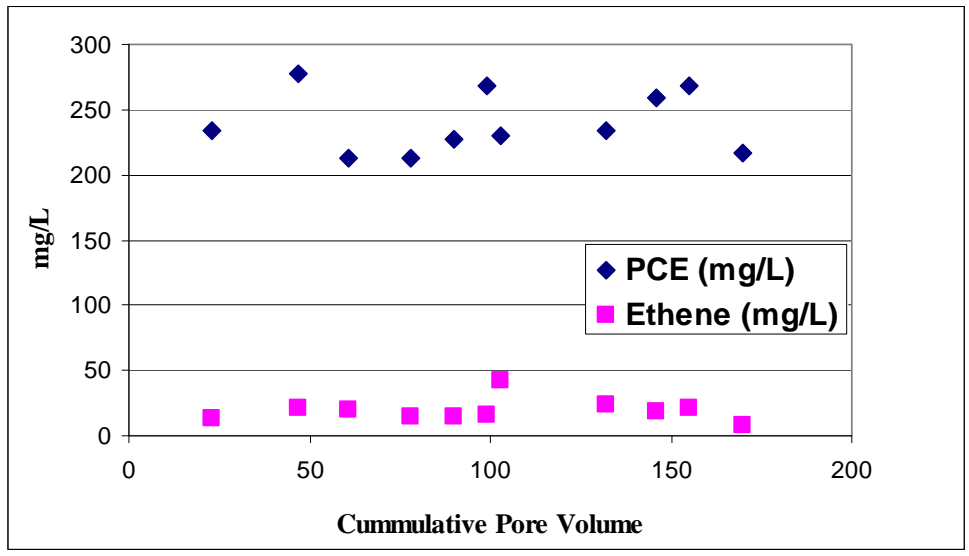
Figure III-25. Concentrations of dissolved phase PCE and ethene in effluent collected from a column containing entrapped PCE-DNAPL and treated with a 10 g/L suspension of RNIP.

The 10 g/L S-RNIP suspension, maintained under continuous stirring with an impeller rotating at 200 rpm, was introduced into the column from a Morton flask using a peristaltic pump. Column effluent samples were collected every 5 min during S-RNIP injection and analyzed for PCE as well as potential reaction products including TCE, DCE, VC, and ethene. The concentration of PCE decreased throughout the S-RNIP introduction period while the concentration of ethene steadily increased. After the column was filled with S-RNIP, clean water containing 10 mM sodium bicarbonate was continuously pumped through the column at a flow rate of 0.25 mL per minute to determine if the retained S-RNIP would react with the residual PCE-DNAPL remaining in the column and reduce the effluent concentration of PCE. Of the 4.6 mL PCE initially present in the column, 54.5 percent removed by dissolution in the effluent during 241 pore volume water flush, while only 3.5 percent was transformed to ethene. These findings are consistent with the results presented above, and lead to the general conclusion that emplacement of nZVI with a DNAPL source zone is unlikely to result in complete conversion of PCE to ethene at the local scale. Further analyses of the nZVI column results, including mathematical modeling of the experimental data and a detailed a sensitivity analysis (e.g., nZVI iron content, length of nZVI treatment zone), are presented in discussed in Section III.4.

III.3. CONTAMINANT MASS REDUCTION IN HETEROGENEOUS MEDIA

A series of two-dimensional (2-D) aquifer cells experiments was conducted to assess the delivery of nZVI systems developed and evaluated in Tasks 1 and 2. Initial experiments involved the assessment of the delivery and redistribution of two nZVI delivery systems, unmodified RNIP and surfactant (Tween 80)-stabilized RNIP. In these experiments the size and location of the nZVI reactive zone were directly compared to the transport path of a non-reactive tracer, while subsequent experiments were designed to evaluate the nZVI reactivity in systems containing DNAPL source zones. Qualitative (visual observations) and quantitative data (e.g., concentration profiles) obtained from the 2-D aquifer cell experiments were used to assess the nZVI delivery and reactivity, and to inform the development and validation of mathematical models developed in Task 4.

III.3.1. RNIP Aquifer Cell Experiments

Time lapse photographs of the RNIP delivery experiments are presented in Fig. III-26. Inspection of the Figure reveals that the non-reactive tracer pulse readily moved horizontally through the aquifer cell and reached the right boundary after approximately 22 min. Unmodified RNIP and surfactant stabilized RNIP, on the other hand, did not move even after 1 hour. The observed lack of migration of the RNIP and S-RNIP pulses following injection is consistent with column results presented in Section III.2, which demonstrated no further migration of the nanoparticle front once nanoscale iron delivery was stopped. The size of the injected non-reactive tracer pulse was approximately 6.9 cm diameter. In contrast, the diameter of the region occupied by RNIP was only 3.0 cm, while the diameter of S-RNIP region was approximately 6.0 cm diameter (Fig. III-26). The greater extent of nanoscale iron migration in the presence of 1,000 mg/L Tween 80 was also consistent with column experimental results.

Nano-material	0- min	1-min	4-min
Tracer			
	5-min	7-min	8-min
Tracer			
	0-min	20-min	
RNIP			
	0-min	20-min	
Tween 80 - RNIP			
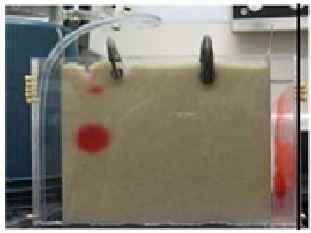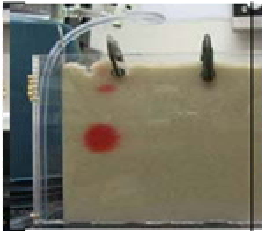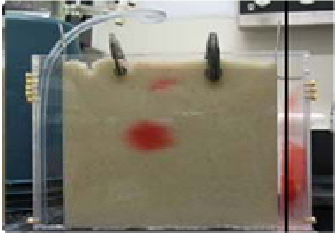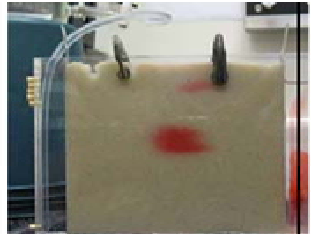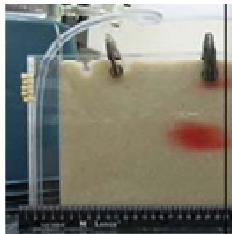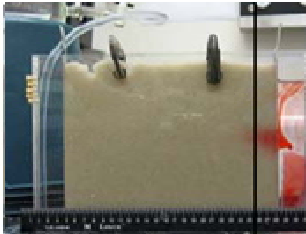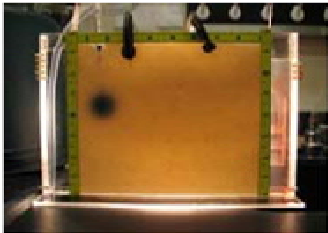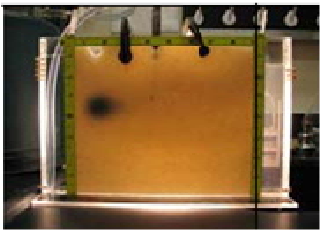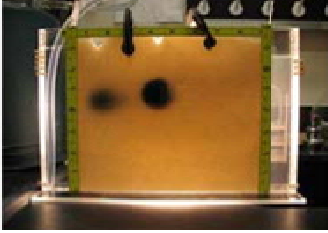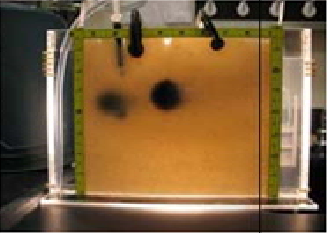
Figure III-26. Transport of a non-reactive tracer and RNIP in the aquifer cell following point injection into a horizontal flow field at 19.2 mL/min (left to right).

III.3.2. Z-Loy Aquifer Cell Experiments

Two experiments were conducted to evaluate Z-Loy emplacement and reactivity within DNAPL source zones. In the first experiment, Z-Loy was injected upstream of the DNAPL source to evaluate its ability to distribute into the source zone. In the second experiment, Z-Loy was directly injected into the source zone.

III.3.2.1. Aquifer Cell 1

Port sample data and flux-averaged effluent TCE concentration data from the first experiment are presented in Figs. III-27 and III-28.
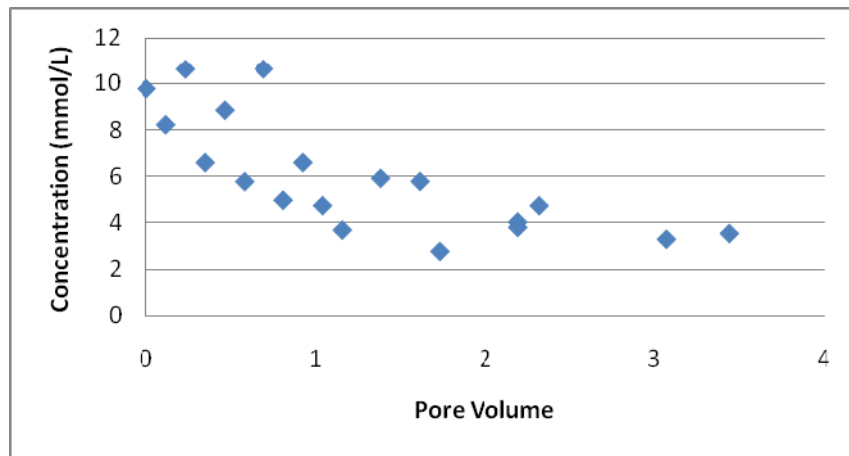
Figure III-27. Concentrations of TCE in the effluent for experiment #1.
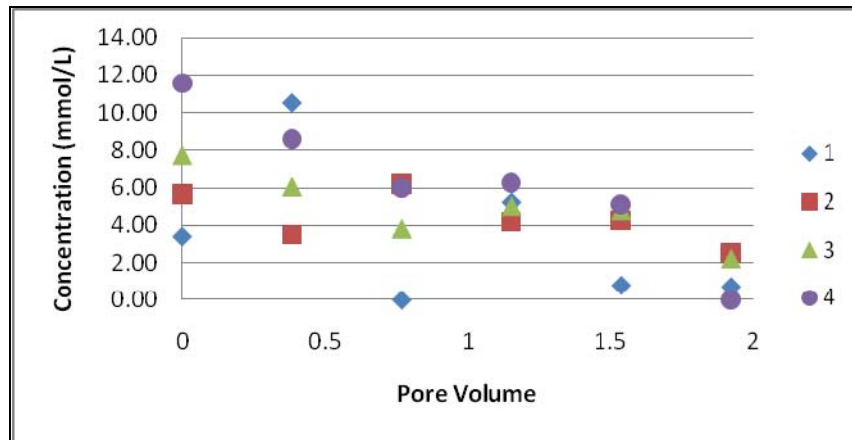
Figure III-28. TCE concentrations in sampling ports for experiment #1. Sampling was discontinued after 2 pv.

Although not shown here, negligible levels of dechlorination products (ethene and ethane) were observed in all samples. Additionally, analysis of effluent and port samples yielded negligible

amounts of H_2 and Cl^-, suggesting that negligible transformation of TCE was occurring in the cell. Inspection of the figures, however, reveals that TCE concentrations, decreased in both ports downstream of the injection location and in the effluent samples. Indeed, batch tests conducted in conjunction with Experiment #1 confirmed that this shipment of Z-Loy was not reactive. Thus, the reduction in TCE concentrations may be attributed to changes in the flow field created by the injection of the Z-Loy. Examination of Fig. III-29 supports this hypothesis. Here, visualization of the dyed influent tracer reveals that the flow appears to bypass the zone containing Z-Loy, suggesting that there was a reduction in permeability due to the presence of Z-Loy and resulting in an alteration of the flow path. Furthermore, no iron was detected in the effluent samples, although it is noted that our analysis was focused on assessing iron concentrations that were indicative of Z-Loy particles - not necessarily dissolved iron. The lack of iron in the effluent suggests Z-Loy transport is limited to the black region shown Fig. III-30 and supports the hypothesis that flow through the region into which Z-Loy was injected is limited. Thus, we hypothesize that the reduction in TCE concentration observed in both the effluent and port data results from the limited flow through the region of the aquifer cell containing the majority of the DNAPL. To further explore this idea, a non-reactive tracer test was conducted following the Z-Loy injection. Comparison of the pre and post Z-Loy emplacement tracer test data in Fig. III-30 reveals that the post emplacement tracer broke through about a fifth of a pore volume earlier than the one prior to injection, again indicating that some of the pore volume was occluded from the flow, presumably caused by pore clogging associated with the injection of Z-Loy. While the results of the quantitative tracer test are consistent with the qualitative photographs, it is noted that the photographs suggest a much greater influence of the Z-Loy on the flow field.
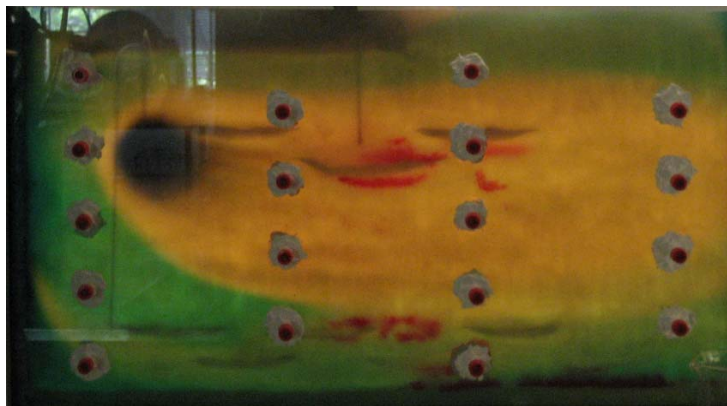
Figure III-29. Photograph of flow in Experiment #1 1.0 pv after the final Z-Loy injection.
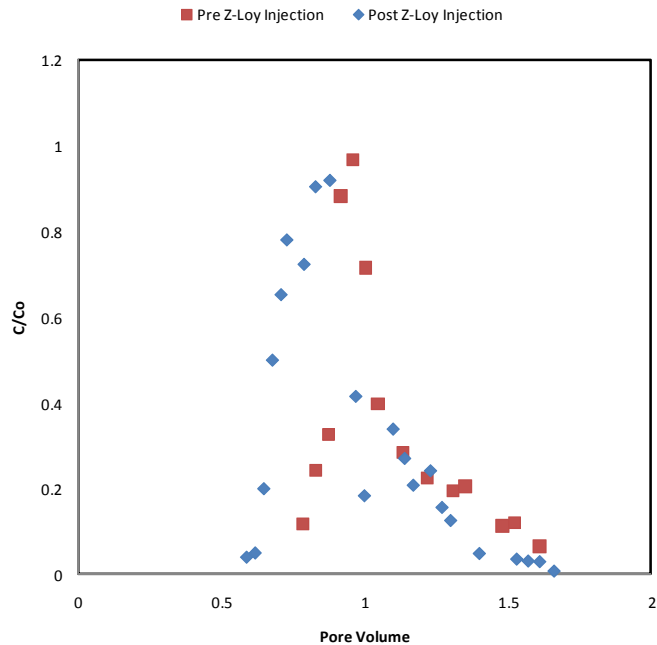
Figure III-30. Tracer tests from Experiment #1 used to assess the influence of the Z-Loy on the flow.

III.3.2.2. Aquifer Cell 2

A second aquifer cell study was conducted with a new supply of Z-Loy to determine the extent to which the reactive particles can reduce source zone mass. An initial injection was followed by a subsequent injection close to the left and right of the original injection. During the two injections to the cell, pore clogging immediately surrounding the injection area was observed and adjustments were made to the location of the injection tube (0.125 in SS tubing) to permit the remaining mass of Z-Loy to be injected. As with the previous aquifer cell, the issues of pore clogging suggest Z-Loy transport was minimal. Effluent samples had negligible total iron content, confirming the limited transport of the iron product. Concentration data are shown in Fig. III-31 for the tracer test conducted immediately after DNAPL redistribution and for the tracer test conducted after the Z-Loy injection.

As with the first aquifer cell, the earlier breakthrough of the tracer following the Z-Loy injection suggests that emplacement of the iron limited transport though the iron-containing portions of the aquifer cell. Shown in Figs. III-32-III-35 are the light transmission images, as well as the DNAPL saturations before and after the iron injection. Note that the iron mass in Fig. III-34 prohibits assessment of the DNAPL saturations in the corresponding region of Fig. III-35. While the DNAPL saturations in the iron-containing zones cannot be quantified, Fig. III-35 does show some evidence of DNAPL redistribution resulting from the injection process. It should be noted that this limited mobilization is likely the result of repositioning the injection tube and represents a physical disturbance of the DNAPL architecture similar to that which may occur during drilling or direct push installation of injection points. There was no evidence of DNAPL mobilization resulting from chemical effects such as a reduction in interfacial tension.

67
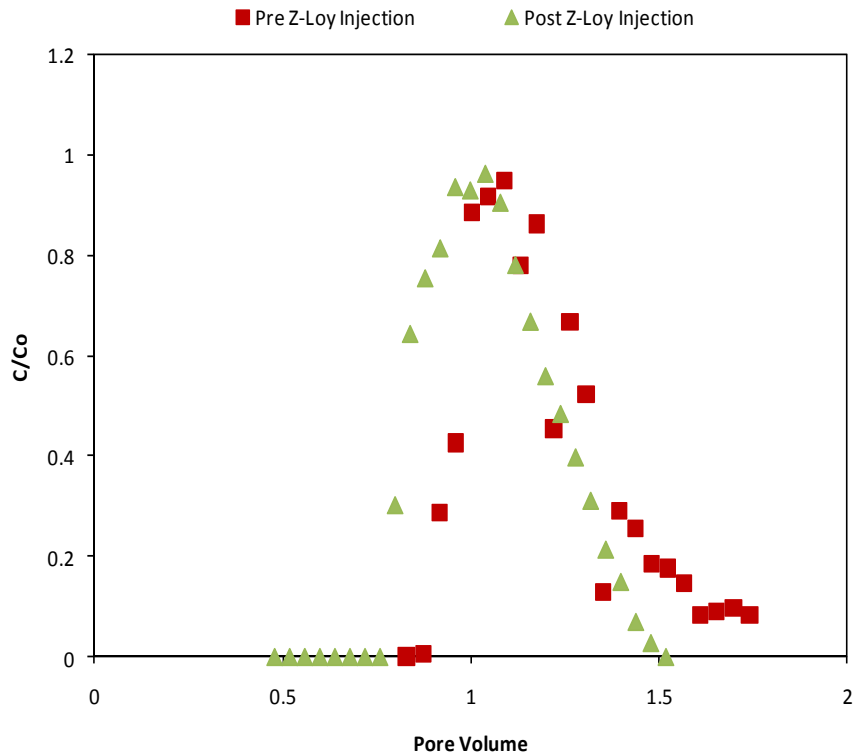
Figure III-31. Tracer test data from Experiment #2.

Effluent and port samples were taken over the next 6.5 pore volumes. During this period of sample collection, the flow was interrupted four times to shut in the aquifer cell for a fixed duration. These flow interruptions were employed to explore the influence of the flow on the reduction of TCE. Shown in Figs. III-36- III-38 are the observed flux-averaged effluent concentrations of TCE, ethene and ethane, and chloride, respectively. Recall that batch experiments suggested that ethene and ethane are the major products of TCE reduction using Z-Loy. TCE, ethene, and ethane concentrations in samples collected from the side ports are shown in Figs. III-39-III-42, respectively.
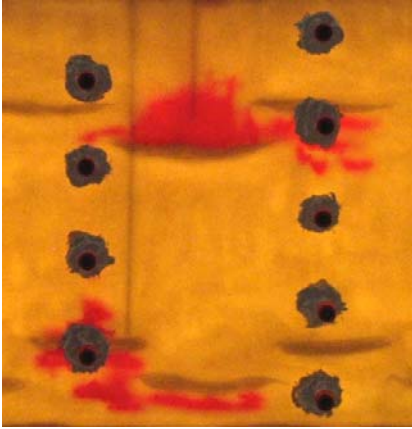
Figure III-32. Source Zone, Pre Z-Loy
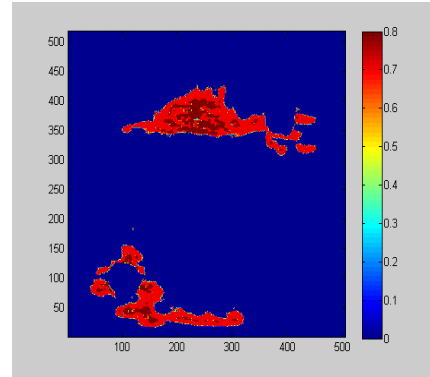
Figure III-33. Source Zone Saturation, Pre Z-Loy
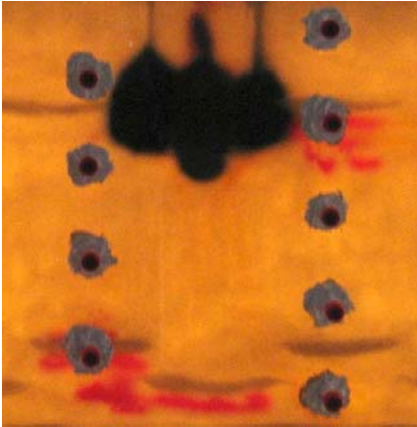
Figure III-34. Source Zone, Post Z-Loy
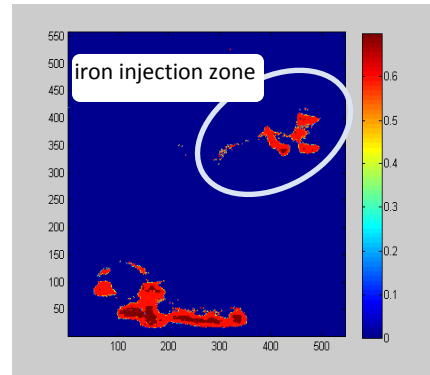
Figure III-35. Source Zone Saturation, Post Z-Loy
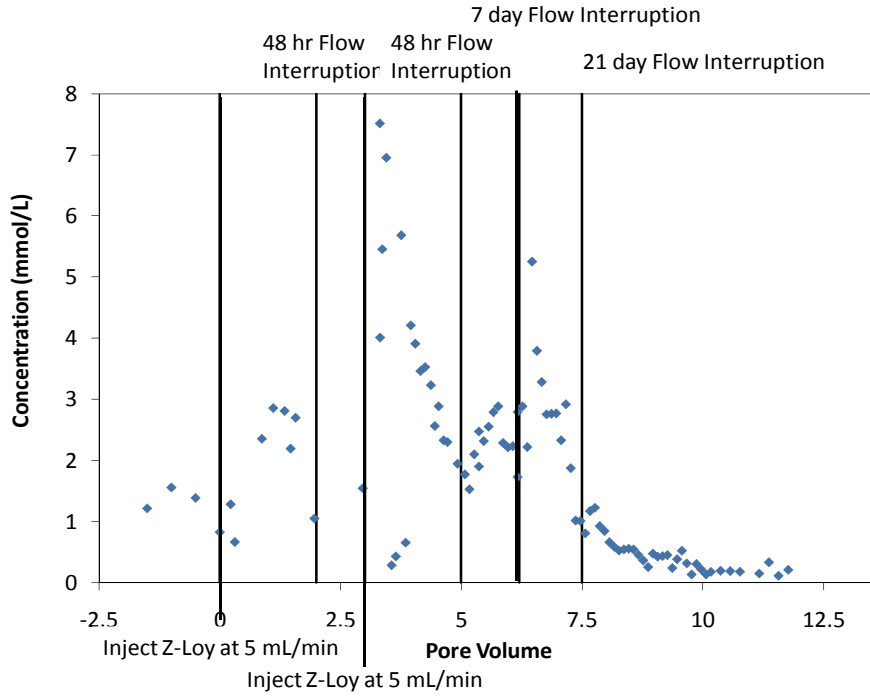
Figure III-36. Effluent concentrations of TCE in Experiment #2.
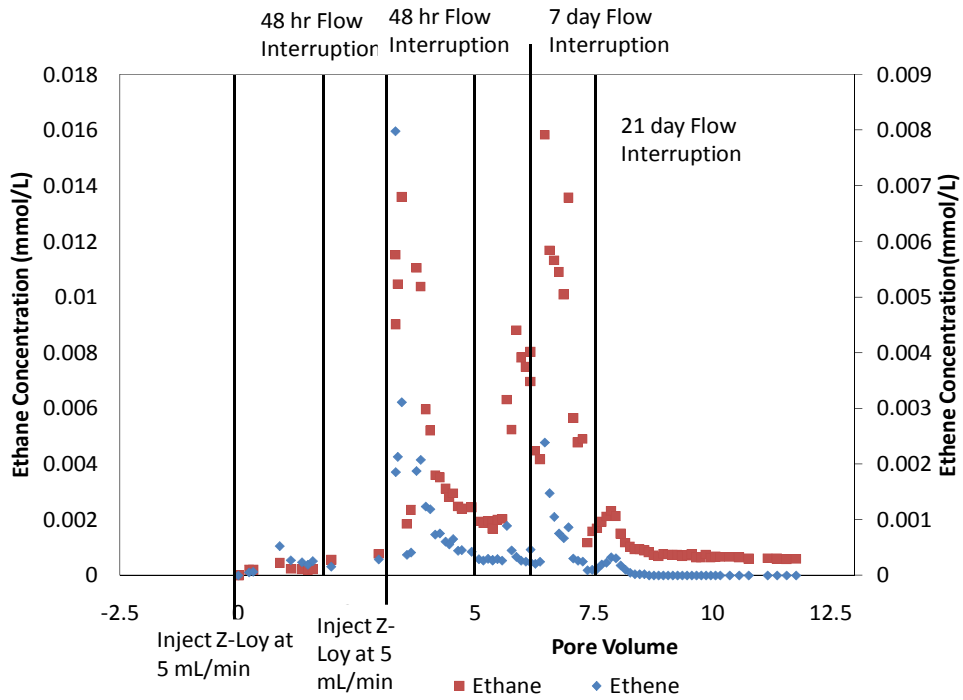
Figure III-37. Effluent concentrations of ethene and ethane in Experiment #2.
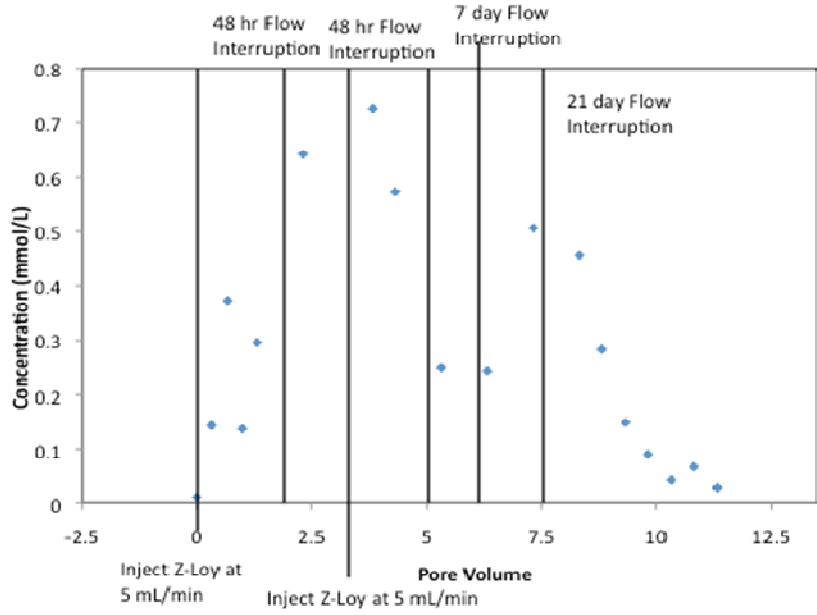
Figure III-38. Effluent concentrations of chloride in Experiment #2.
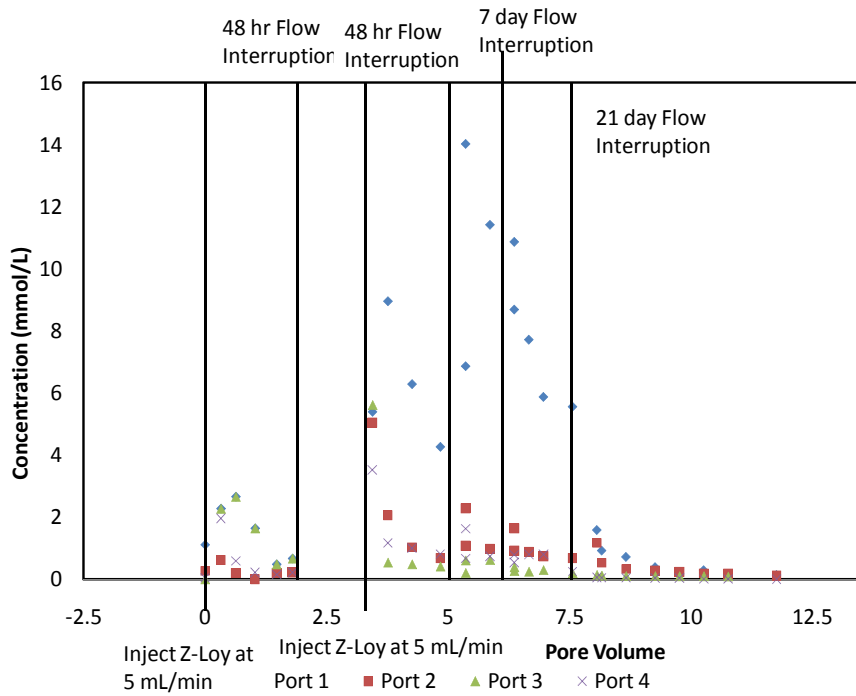
Figure III-39. TCE concentrations from port samples in Experiment #2.
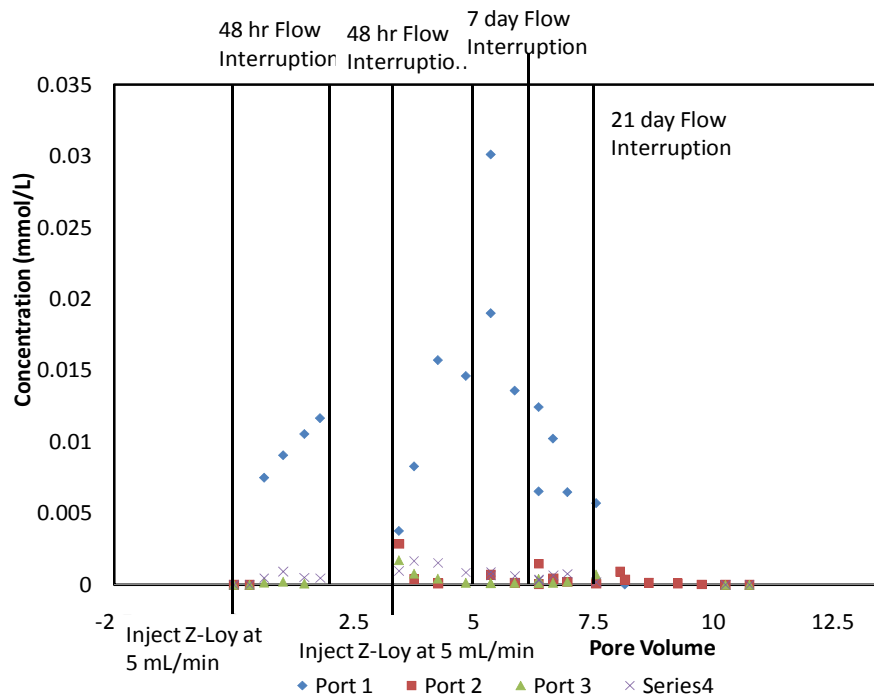
Figure III-40. Ethene concentration from port samples in Experiment #2.
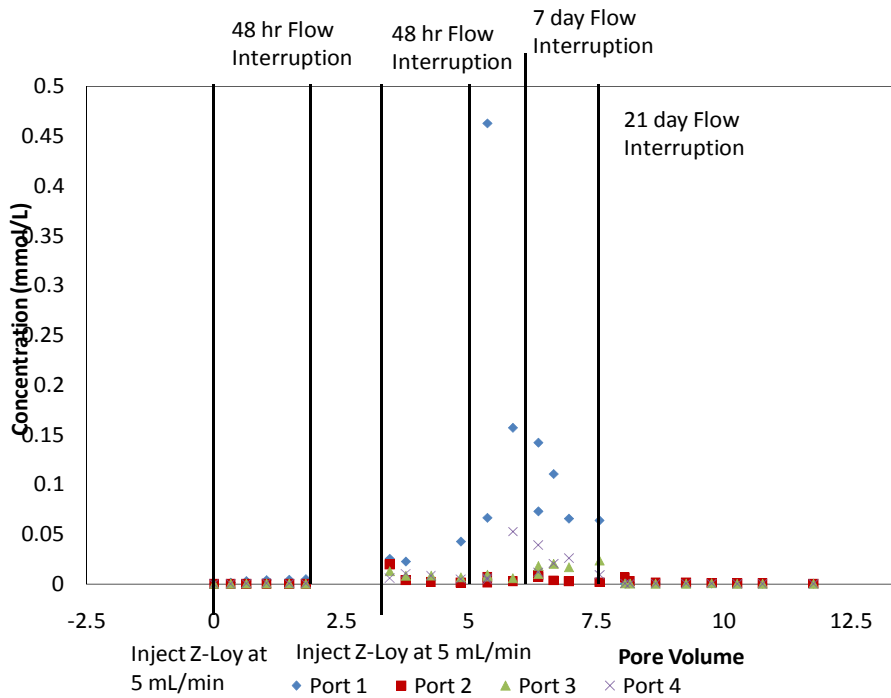
Figure III-41. Ethane concentrations in port samples in Experiment #2.

Port 1, which is directly downstream of the source zone, exhibited the largest amounts of TCE and degradation products. Ports 3 and 4 showed an increase in concentrations following injection, but the concentrations were not of the same magnitude as Port 1. All of flow interruptions were followed by increases in concentrations of all constituents. Flow interruptions occurring after 6 pore volumes represent several days post Z-Loy injection. Moreover these later flow interruptions were for extended periods of time (days). The increases in ethene and ethane following these shut in periods suggest that the reaction is long lasting. The reaction, however, is not sufficient to keep up with dissolution. As is shown in Fig. III-42 the main mechanism of TCE removal in Experiment #2 was dissolution. Two assessments were used for the amount of TCE reacted: chloride concentrations and ethene + ethane concentrations. The data suggest chloride is a more reliable method of assessing the reaction extent, perhaps given the volatility of the dissolved gases. Based on the port and effluent data, Z-Loy appears to be able to partially reduce source zone mass and mass flux, but it has a very limited transport range and could not overcome the dissolution process in these experiments.
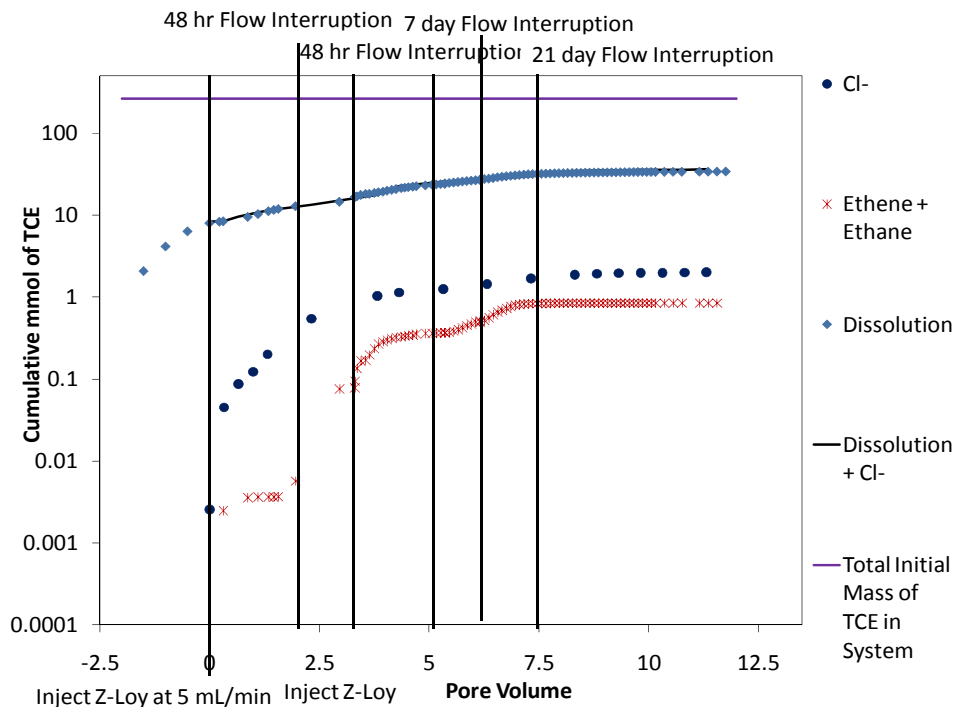
Figure III-42. Cumulative mass discharge.

III.4. MATHEMATICAL MODELING OF ZVI DELIVERY AND REACTIVITY IN DNAPL SOURCE ZONES

III.4.1 DNAPL Mobilization Modeling

III.4.1.1. Trapping Number (N_T) Implementation

The total trapping number is dimensionless number developed to predict the onset of NAPL mobilization based on force balances. At the pore scale, capillary forces act to retain entrapped

73

NAPL ganglia, while viscous and gravity forces may act to promote displacement. *Pennell et al.*[1996] derived the dimensionless total trapping number expression that quantifies this force balance:

$$N_T = \sqrt{N_{Ca}^2 + 2N_{Ca}N_B \sin\alpha + N_B^2} \tag{24}$$

where

$$N_{Ca} = \frac{q_a \mu_a}{\sigma_{an} \cos\theta} \tag{25}$$

$$N_B = \frac{\Delta\rho g k k_{ra}}{\sigma_{an} \cos\theta} \tag{26}$$

Here, q_a is the Darcy velocity of the aqueous phase (positive upward) [L/t], α is the angle of flow relative to the horizontal, μ_a is the dynamic viscosity of the aqueous phase (M/Lt), σ_{an} is the IFT between the aqueous and nonaqueous phases [M/t^2], θ is the contact angle between the aqueous/nonaqueous interface and the porous medium [degrees], $\Delta\rho$ is the density difference between the aqueous and nonaqueous phases [M/L^3], g is the gravitational constant [L/t^2], k is the magnitude of the intrinsic permeability tensor of the isotropic porous medium [L^2], and k_{ra} is the relative permeability to the aqueous phase. Eq. 24 reduces to $N_T = \sqrt{N_{Ca}^2 + N_B^2}$ for horizontal flow ($\alpha=0°$) and $N_T = |N_{Ca} + N_B|$ for vertical flow ($\alpha=90°$). In one-dimensional column experiments, the onset of DNAPL mobilization corresponded to N_T values ranging from 2×10^{-5} to 5×10^{-5}, while complete ganglia displacement was observed at N_T values approaching 1×10^{-3}. These critical N_T values are similar to threshold N_{Ca} values reported for oil desaturation curves in the absence of buoyancy effects, supporting the consistency of the total trapping number approach with previous work reported in the petroleum literature.

In the mobilization module, the value of N_T was computed using Eq. 24. For systems with surfactant (compositional effects on IFT), IFT was represented as a linear function of surfactant concentration below the CMC. In addition, experimental data from *Pennell et al.* [1996] were used to derive a functional relationship between N_T and DNAPL residual saturation. For implementation in MISER, desaturation relations were developed by fitting the following expression to measured PCE-DNAPL desaturation data for each sand type:

$$S_{nr} = S_{nr}^{min} + (S_{nr}^{max} - S_{nr}^{min})[1 + (T_1 N_T)^{T_2}]^{1/T_2 - 1} \tag{27}$$

where S_{nr} is the residual DNAPL saturation, $S_{nr}{}^{max}$ the residual DNAPL saturation before mobilization, $S_{nr}{}^{min}$ is the residual DNAPL saturation after full mobilization, and T_1 and T_2 are fitting parameters. In Eq. 27, T_1 controls the onset of DNAPL mobilization; as T_1 decreases, mobilization occurs at a higher N_T. T_2 controls the desaturation curve shape; a higher T_2 is associated with a steeper desaturation curve. Inspection of the fitted PCE-DNAPL desaturation

curves for each sand type suggested that T_1 decreases with increasing mean grain size and T_2 is a function of grain uniformity. To implement Eq. 27 in the model, S_{nr}^{max} was assumed equal to the initial DNAPL saturation, and S_{nr}^{min} was assumed equal to 0.015, which represents the observed residual saturation at complete mobilization [*Pennell et al.* 1996]. In model validation simulations below, experiments in two sands were simulated (Ottawa 20-30 and Wurtsmith aquifer material). Parameter fits for PCE-DNAPL desaturation in 20-30 mesh Ottawa sand were directly used for the Ottawa sand experiments ($T_1 = 1.31 \times 10^4$ and $T_2 = 7.81$). Wurtsmith aquifer parameters ($T_1 = 2.17 \times 10^4$ and $T_2 = 3.53$) were determined by linear interpolation of sand grain size and uniformity index.

Changes in entrapped residual saturation and IFT will influence capillary retention, relative permeability, and interphase mass transfer. Capillary pressure-saturation relations for the aqueous-nonaqueous system in this study were represented by the van Genuchten functional form [*Van Genuchten*, 1980]. The influence of IFT on the capillary pressure-saturation relationship was incorporated using Leverett scaling. Two widely-used parametric models, the *Mualem* [1976] and *Burdine* [1953] models, were incorporated for estimating relative permeability. In these two models, changes in entrapped DNAPL residual and IFT will affect both the integrand and limits of integration in the relative permeability expressions.

Interphase mass exchange of the organic component between the nonaqueous and aqueous phases was modeled as a rate-limited process that was driven by the difference between aqueous phase concentration and solubility. For model validation, the solubility of PCE in the surfactant solution was represented as a linear function of surfactant concentration at concentration above CMC and remained as the PCE water solubility when the surfactant concentration fell below the CMC. The lumped mass transfer coefficient was estimated from correlations that relate the Sherwood number (N_{Sh}) to the Reynolds number (N_{Re}). For the simulations presented herein the correlation of *Mayer et al.* [1999] was employed based upon similarity in surfactant chemistry for the conditions under which it was derived.

Model predictions were compared to data from three low-IFT mobilization experiments that were previously conducted in horizontal rectangular glass columns containing uniform distributions of residual PCE. Comparisons of observed displacement fronts and effluent recovery data with numerical simulations of the mobilization were used to validate the total trapping number approach and the enhancements to the MISER model. A more complete presentation of this work may be found in *Li et al.* [2007].

III.4.1.2. Description of Mobilization Experiments

Experimental methods are described briefly here. A more complete description can be found in *Li et al.* [2007]. Three displacement experiments were conducted in rectangular glass columns with internal dimensions of 14.8 cm (length) × 5.2 cm (height) × 2.6 cm (width). Two columns (Experiments OS-1 and OS-2) were packed with 20-30 mesh Ottawa sand (U.S. Silica) and one column (Experiment WS-1) was packed with aquifer material obtained from Wurtsmith Air Force Base located in Oscoda, MI. Relevant properties of the two porous media are summarized in Table III-11.

Table III-11. Relevant properties of 20-30 mesh Ottawa sand and Wurtsmith aquifer material.

Soil Property	Wurtsmith aquifer material	20-30 mesh Ottawa sand
Mean grain size, d_{50} (mm)	0.35	0.71
Intrinsic permeability, k (m^2)	4.2×10^{-11}	3.9×10^{-10}
Solid density, ρ_s (g/cm^3)	2.65	2.65
Organic carbon content, f_{oc} (% wt.)	0.02	nd
Van Genuchten α (1/Pa)	1.67×10^{-4}	9.59×10^{-4}
Van Genuchten n	5.31	7.42
Estimated residual aqueous phase saturation, S_{ar}	0.125	0.07
Estimated maximum residual PCE saturation, S_{nr}	0.15	0.12
Linear PCE sorption coefficient, K_D (mL/g)	0.17	0.08

To facilitate visual observation of PCE-DNAPL within the rectangular columns, PCE was dyed with Oil-Red-O (Fisher Scientific). The surfactants, sodium diamyl sulfosuccinate (Aerosol® AY) and sodium dioctyl sulfosuccinate (Aerosol® OT), were obtained from American Cyanamid (now Cytec), and used as received from the manufacturer. All aqueous surfactant solutions were prepared with distilled water that had passed through a Nanopure® Analytical purification system (Barnstead/Thermolyne Corp.).

Three rectangular columns were packed with either air-dry Ottawa sand or Wurtsmith aquifer material and a uniform residual saturation of PCE-DNAPL was established following the procedures of *Pennell et al.* [1996]. The columns were oriented horizontally and flushed with an aqueous solution consisting of a 4% (wt.) 1:1 mixture of Aerosol® AY and Aerosol® OT containing 500 mg/L of CaCl$_2$. The liquid density of the 4% Aerosol AY/OT solution at 20 °C was determined to be 1.03 g/cm^3 using calibrated 25-mL glass pycnometers (Ace Glass). The dynamic liquid viscosity of the 4% Aerosol AY/OT was 3.5 cP, measured at a shear rate of 200 s^{-1} using a Rheostress R-75 rheometer (Haake). At 22 °C, the 4% 1:1 Aerosol AY/OT solution has an apparent PCE solubility of 71,720 mg/L and an IFT with PCE of 0.09 dyne/cm. The critical micelle concentration of Aerosol AY/OT was calculated to be approximately 1,200 mg/L (1992). Experimental conditions for each column, including the capillary, Bond and total trapping numbers, are summarized in Table III-12.

Table III-12. Flushing parameters, dimensionless analysis, and PCE recoveries for the Wurtsmith (WS-1) and Ottawa sand (OS-1, OS-2) displacement experiments.

Experimental Parameter	Displacement Experiment		
	WS-1	OS-1	OS-2
Porosity,	0.38	0.36	0.36
Total pore volume, pv (mL)	76.0	71.2	72.3
Initial PCE-DNAPL saturation, S_n (%)	12.9	12.4	13.8
Effective aqueous-phase permeability, k_e (m²)	1.72×10^{-11}	1.76×10^{-10}	1.64×10^{-10}
Aqueous phase flow rate, Q_a (mL/min)	0.96	0.96	4.95
Aqueous phase Darcy velocity, q_a (cm/min)	0.07	0.07	0.36
Capillary number, N_{Ca}	4.54×10^{-4}	4.54×10^{-4}	2.33×10^{-3}
Bond number, N_B	1.12×10^{-3}	1.15×10^{-2}	1.07×10^{-2}
Total trapping number, N_T	1.21×10^{-3}	1.15×10^{-2}	1.10×10^{-2}
Angle of mobilization, τ	67.9	87.7	77.7
PCE recovered as NAPL (mL)	9.92	9.30	9.07
PCE recovery as NAPL (% vol)	101.4	105.2	91.2

Three experiments were conducted to evaluate the mobilization and subsequent migration of residual PCE-DNAPL in rectangular soil columns (Table III-12). The total pore volumes (PV) of the columns, which were packed with either Wurtsmith aquifer material (Experiment WS-1) or 20-30 mesh Ottawa sand (Experiments OS-1 and OS-2) ranged from 71 to 76 mL. Following water saturation, PCE-DNAPL injection, and water displacement, the initial residual PCE saturations ranged from 12.4 to 13.8%. The entrapped PCE-DNAPL could be visually observed as entrapped droplets and ganglia, uniformly distributed throughout the columns. The effective permeability to water (ke = kkra) of the Ottawa sand columns (OS-1 and OS-2) was approximately 1.70×10^{-10} m2, while the corresponding value for the Wurtsmith column (WS-1) was one order-of-magnitude lower (1.72×10^{-11} m2), consistent with the differences in intrinsic permeability (Table III-11).

Based on measured properties of the 4% Aerosol® AY/OT flushing solution (μa = 3.5 cP; ρa = 1.03 g/mL; IFT = 0.09 dyn/cm), applied Darcy velocities (0.07 or 0.36 cm/min) and effective permeability values, the capillary (N_{Ca}), Bond (N_B) and total trapping (N_T) numbers were computed using Eqs. 25, 26, and 24, respectively (Table III-12). The resulting values of N_T ranged from 1.21×10^{-3} (WS-1) to 1.10×10^{-2} (OS-2), which are greater than the experimental value (1×10^{-4}) corresponding to nearly complete displacement of PCE-DNAPL from one-

dimensional soil columns packed with various size fractions of Ottawa sand. Thus, mobilization of the entrapped PCE-DNAPL was expected during flushing with the 4% Aerosol AY/OT solution. In addition, the Bond numbers calculated for each experiment were 2.5 to 25 times larger than their corresponding capillary numbers, indicating that gravity will have a greater impact on PCE-DNAPL mobilization than viscous forces, and therefore downward migration of mobilized PCE-DNAPL is likely to occur.

In the first displacement experiment conducted with Wurtsmith aquifer material (WS-1), mobilization of residual PCE-DNAPL was observed immediately after introducing the 4% Aerosol AY/OT solution into the column at a flow rate of 0.96 mL/min. After flushing with 0.13 PV of surfactant solution, a sufficient volume of mobilized PCE-DNAPL had migrated downward to form a 10-cm high bank of mobile DNAPL above the lower boundary of the rectangular column (Fig. III-43a). As flushing proceeded, an angled bank of PCE-DNAPL formed along the lower portion of the rectangular column (Fig. III-43b, 0.38 PV), which moved toward the column outlet at an average pore velocity of approximately 0.17 cm/min, calculated from the location of the x-axis centroid of the bank over time. The observed bank angle at 0.38 PV was at least 60º from vertical, as shown in Fig. III-43b, with the region of the bank 20 to 80 cm from the inlet forming an angle of approximately 70º. The expected angle of this DNAPL bank displacement relative to the x-axis (τ) can be obtained from the ratio of the Bond and capillary numbers:

$$\tau = \arctan\left(\frac{N_B}{N_{Ca}}\right) \tag{28}$$

where a τ value of 0° corresponds to a vertical bank (perpendicular to flow) and a value of 90° indicates a horizontal bank (parallel to flow). Based on Eq. 28 the estimated bank angle is 68º, which compares favorably with the experimental observations (Table III-12). Hence, the onset, extent, and angle of PCE-DNAPL mobilization observed during low-IFT surfactant flushing of Wurtsmith aquifer material were consistent with expected behavior based on total trapping number analysis. Note that bank behavior is also consistent with previous studies in two-dimensional aquifer cells containing residual TCE-DNAPL, where injection of a low-IFT Aerosol MA surfactant solution (NT = 2.0×10-3) resulted in formation of TCE-DNAPL banks with angles of approximately 65º and 85º, similar to the values (76º and 87º, respectively) predicted using Eq. 28.

In the second set of displacement experiments, the effect of flow rate on PCE-DNAPL mobilization behavior was explored in a higher permeability medium, 20-30 mesh Ottawa sand (k = 3.9×10-10 m2). In the first Ottawa sand experiment (OS-1), the 4% Aerosol AY/OT solution was introduced at a flow rate of 0.96 mL/min. Representative images of the column after flushing with 0.43 and 0.76 PV of the surfactant solution are shown in Fig. III-44. Mobilization of residual PCE-DNAPL was observed immediately after introducing the surfactant solution. Individual PCE droplets migrated downward and accumulated along the lower boundary of the rectangular column to form a bank of mobile DNAPL approximately 6 cm thick (Fig. III-44). The rapid downward migration of mobilized PCE-DNAPL droplets resulted in an inverted front (i.e., approximately 45º from horizontal) between the advancing surfactant solution and the zone of residual PCE, with the fastest migration of the surfactant solution immediately above the bank of mobile DNAPL. This behavior was attributed to the greater

permeability of the clean medium relative to that with residual saturation, the shorter vertical travel distance for the PCE droplets located closer to the bank, and the greater density of the surfactant solution containing solubilized PCE relative to the resident aqueous solution. This phenomenon can be thought of as "mobilization fingering" and is analogous to the dissolution fingering process, where the removal of entrapped DNAPL via dissolution leads to increased effective permeability and fingered patterns of clean media [*Imhoff and Miller*, 1997]. The bank of mobile DNAPL was nearly horizontal along the upper surface, consistent with the 88º bank angle computed using Eq. 28. The mobile PCE-DNAPL bank migrated steadily toward the effluent end of the column at a pore velocity of approximately 0.19 cm/min, resulting in the recovery of 91.2 % of the initial PCE volume after flushing with 2.0 PV of 4% Aerosol AY/OT (Table III-12).
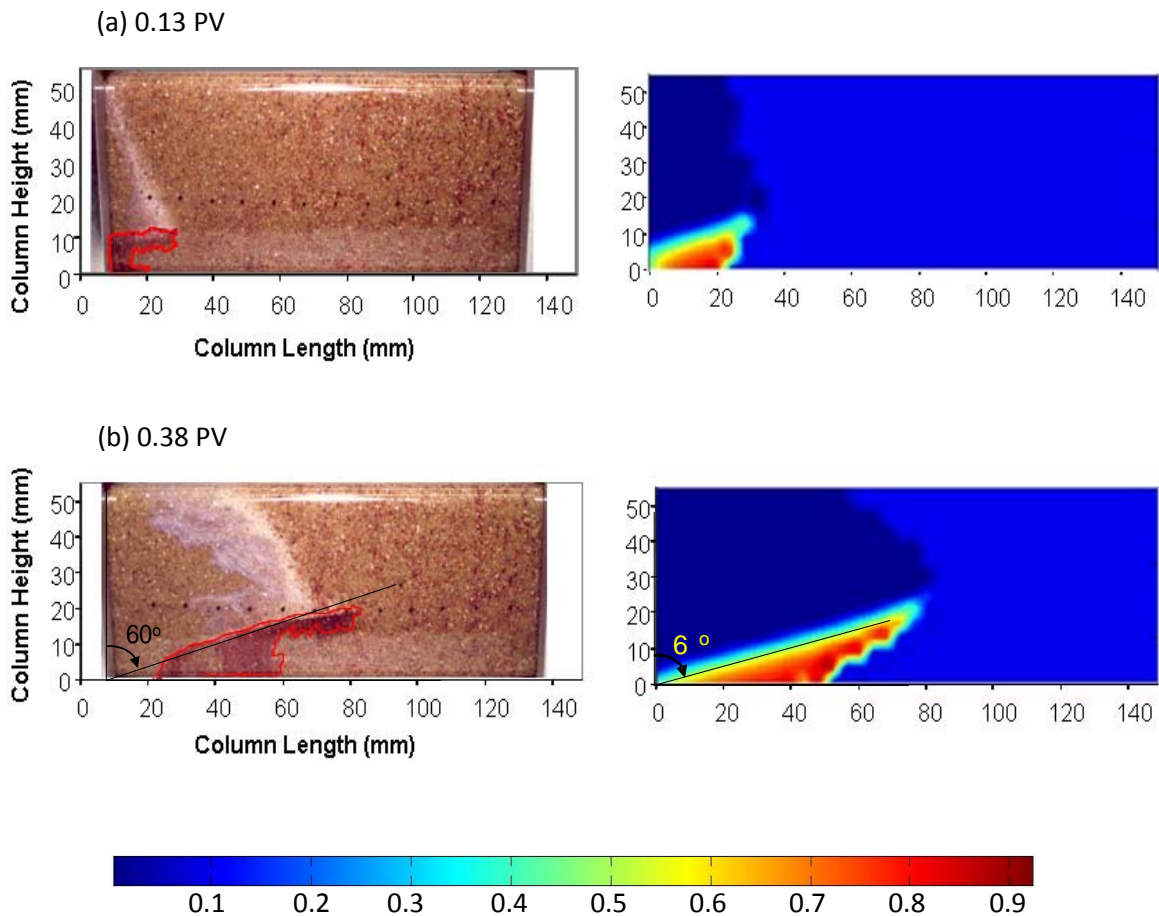
Figure III-43. Comparison of observed and simulated PCE-DNAPL saturation profiles after flushing Wurtsmith aquifer material with (a) 0.13 and (b) 0.38 pore volumes (PV) of 4% 1:1 Aerosol AY/OT at a rate of 0.96 mL/min (Experiment WS-1).

In the second Ottawa sand displacement experiment (OS-2), the flow rate was increased to 4.95 mL/min in an effort to create a more vertical advancing surfactant front (i.e., smaller bank angle). Photographs of the resulting displacement profile after injecting 0.50 and 0.68 PV of 4% Aerosol AY/OT solution are shown in Fig. III-45. Despite the increased flow rate, the surfactant solution again advanced more rapidly immediately above the 6-cm thick bank of mobile DNAPL

79

located along the lower boundary of the column. The bank of mobile DNAPL migrated steadily along the bottom of the column at an average velocity of 1.1 cm/min, an increase that was approximately proportional to the increase in applied aqueous flow rate between experiments OS-1 and OS-2 (Table III-12). Complete recovery (105% mass balance) of PCE-DNAPL was achieved after flushing with 2.0 PV of 4% Aerosol AY/OT (Table III-12).

Despite the 5-fold increase in aqueous flow rate (viscous force), the angle of the mobile DNAPL bank decreased only slightly compared to the first Ottawa sand experiment (OS-1). An 80° angle (from vertical) is superimposed on the 0.50 PV panel (Fig. III-45b), and shows that the bank angle of 78° calculated based on a force balance (Eq. 28) over-predicted the effect of increased flow rate (viscous force). The formation of relatively flat mobile DNAPL banks along a lower confining boundary during low-IFT surfactant flushing was also observed by *Willson et al.* [1999]. Together these observations suggest that the bank angle concept may only provide an initial estimate of the migration trajectory of mobilized DNAPL.
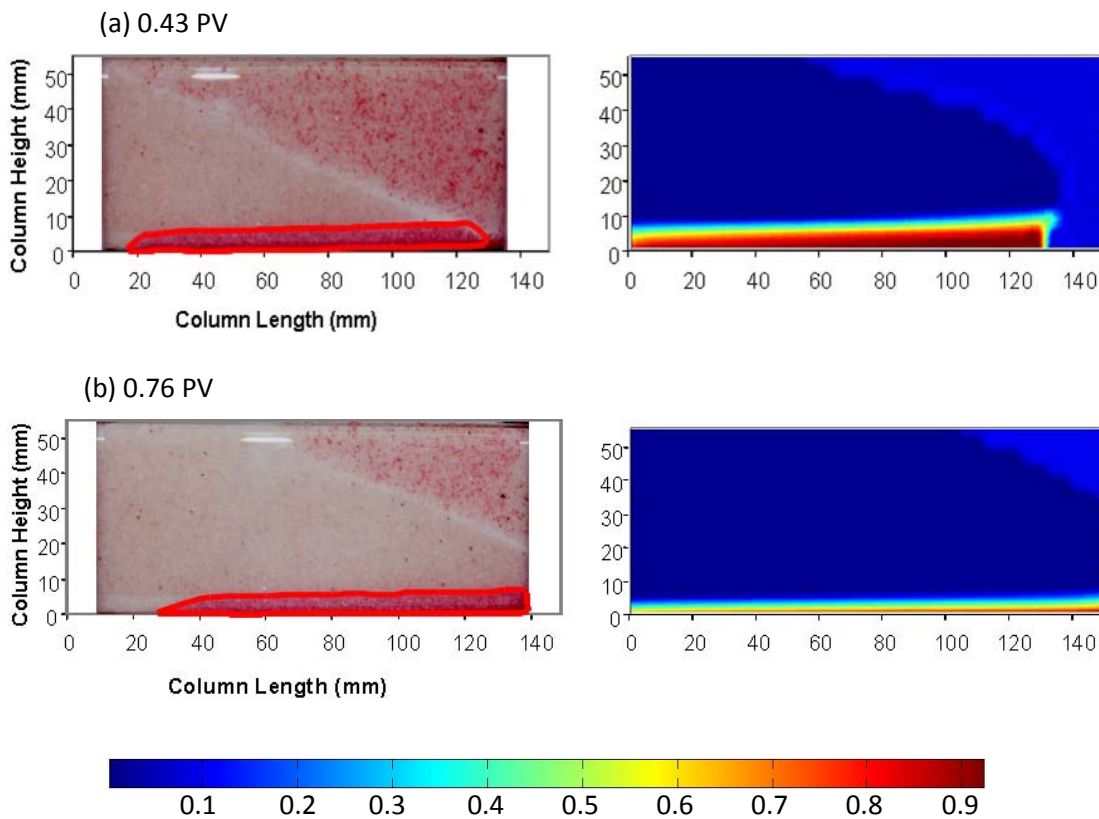
Figure III-44. Comparison of observed and simulated PCE-DNAPL saturation profiles after flushing 20-30 mesh Ottawa sand with (a) 0.43 and (b) 76 pore volumes (PV) of 4% 1:1 Aerosol AY/OT at a rate of 0.96 mL/min (Experiment OS-1).

III.4.1.3 Model Validation

The numerical model was implemented for the three low-IFT displacement experiments. The rectangular columns were discretized using a herring-bone type finite element mesh, with a 2-mm vertical and horizontal spacing. Finer discretizations did not yield substantially different results and required much longer computing time. The initial time step was set as 0.001 sec, which was later automatically adjusted based upon solution convergence history. A no-flow boundary condition was established for both aqueous phase and nonaqueous phase on the left, top and bottom boundaries of the column domain. The aqueous surfactant solution was uniformly supplied to the column inlet through a series of source terms. At the column outlet, total flow rate was set equal to aqueous phase inflow rate (incompressible assumption). The distribution of aqueous and nonaqueous flow rates at the outlet was determined by the ratio of relative permeability of the two phases. No dispersive flux conditions were enforced for all components on all boundaries in both phases, except that a constant flux boundary condition was prescribed for the aqueous phase components at the column inlet. For all three experiments, cumulative mass balance errors for the components were less than 0.5%.
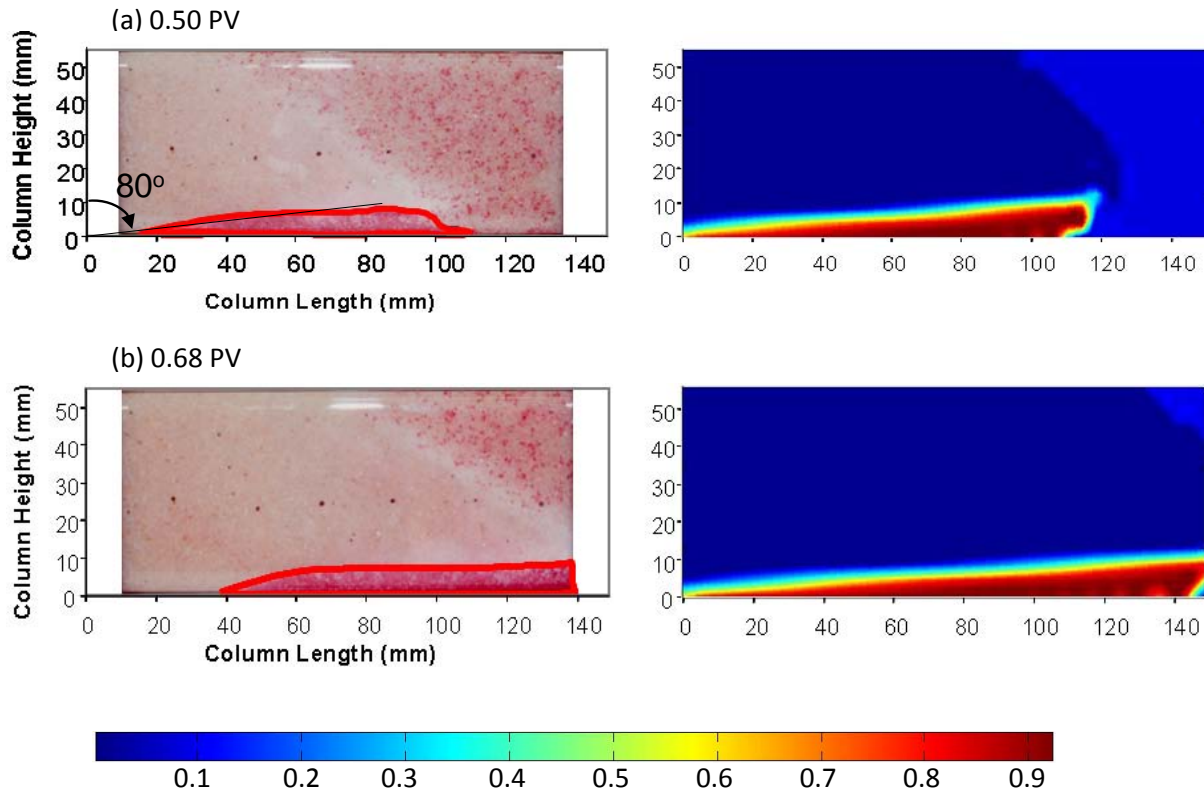
Figure III-45. Comparison of observed and simulated PCE-DNAPL saturation profiles after flushing 20-30 mesh Ottawa sand with (a) 0.50 and (b) 0.68 pore volumes (PV) of 4% 1:1 Aerosol AY/OT at a rate of 4.95 mL/min (Experiment OS-2).

The applicability of a relative permeability model to the low-interfacial tension displacement system was evaluated first by comparing experimentally-derived effluent recovery curves to simulations based on either the *Mualem* [1976] or *Burdine* [1953] models. Simulations of

cumulative PCE-DNAPL volume collected in the column effluent are shown in Fig. III-46 for experiments WS-1 and OS-2.

In both experiments, predictions based on the Mualem relative permeability model closely matched the observed effluent PCE volumes. For example, in the Wurtsmith experiment (WS-1) the Mualem model captured the initial rise of the PCE-DNAPL recovery curve and predicted a total effluent free PCE volume of 9.6 mL, which is only slightly less than the measured value of 9.92 mL (Fig. III-46a). In contrast, simulations based on the Burdine model under predicted the rate of PCE-DNAPL flow in the column, resulting in delayed breakthrough of PCE-DNAPL at the column effluent. Based upon these observations, the Mualem relative permeability model was selected for use in the simulations described below.
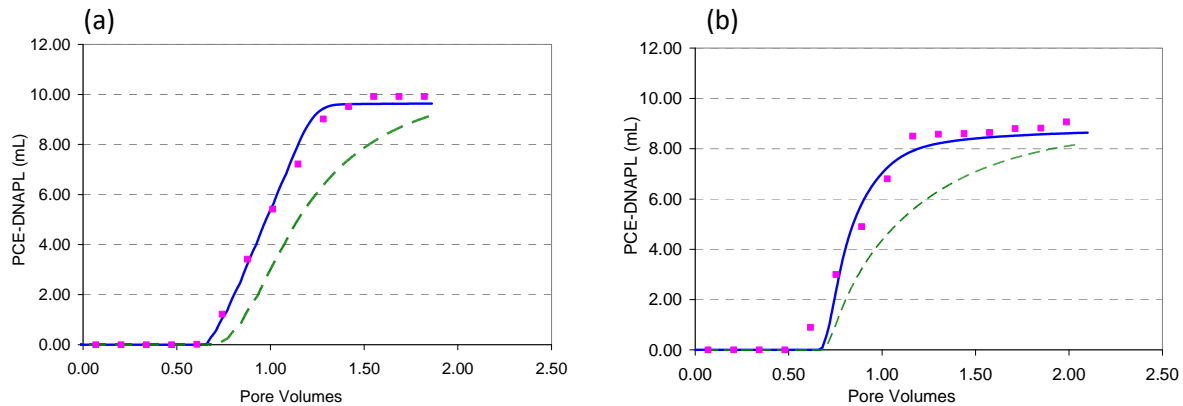
Figure III-46. Comparison of observed (data points) and simulated cumulative effluent PCE-DNAPL recovery curves for Experiments (a) WS-1 and (b) OS-2 based on the Burdine (dashed line) and Mualem (solid line) relative permeability models.

Simulated and experimentally measured PCE-DNAPL saturation profiles are compared at several time points for each column experiment in Figs. III-43, III-44 and III-45. Inspection of these Figures reveals that the formation, location and migration of the mobile DNAPL bank observed in the experiments was generally well reproduced by the numerical simulator. The angle of the simulated mobile DNAPL bank in experiment WS-1 (Fig. III-43b) at 0.38 PV was 68°, which is identical to the value estimated using Eq. 28 (Table III-12) and similar to the observed bank angle of approximately 60°. In both of the experiments conducted with Ottawa sand (OS-1 and OS-2), the numerical model accurately predicted the formation of a relatively flat mobile DNAPL bank along the bottom of the rectangular column (Figs. III-44 and II-45). This behavior is consistent with the large contribution of the gravitational force (N_B) in the higher permeability 20-30 mesh Ottawa sand ($k_e = 1.7 \times 10^{-10}$ m^2) relative to the viscous force (N_{Ca}) (Table III-12).

In the numerical simulations, the N_T was calculated at each time step for all the points within the rectangular column domain to identify the onset of PCE-DNAPL mobilization. Representative plots of the total trapping number profile in the column are provided for all three experiments after injection of 0.5 PV of the 4% Aerosol AY/OT solution. In regions of the column accessed by surfactant solution, the total trapping numbers exceeded 1×10^{-4}, which is consistent with the observed complete displacement of residual PCE-DNAPL. The boundaries between the clean region, mobile NAPL bank, and zone residual PCE-DNAPL are delineated by total trapping

numbers that are similar to the critical value required for the onset of DNAPL mobilization (i.e., 2×10^{-5} to 5×10^{-5}), and are shown as yellow regions in Fig. III-47. Thus, incorporation of N_T to describe the onset of mobilization allowed the simulator to reproduce the general shape of the mobile DNAPL bank and regions of clean soil in all three experiments. Within the mobile DNAPL banks, the simulated PCE-DNAPL saturations were greater than 0.3 and reached a maximum value of 0.9, which corresponds to the minimum residual water saturation of 0.1 (Figures II-43-II-45). These high PCE-DNAPL saturations result in low aqueous phase relative permeability, and thus, the simulated trapping number values computed in the mobile DNAPL bank are small (Fig. III-47).
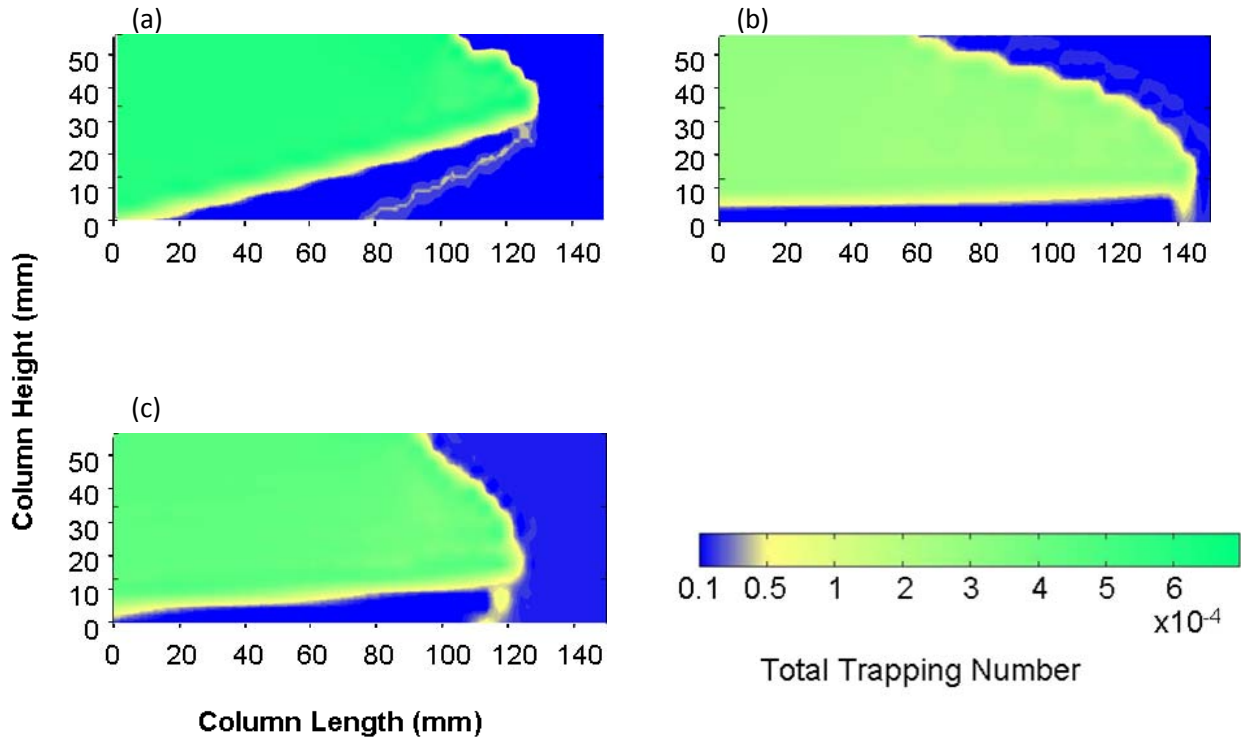
Figure III-47. Plot of the total trapping number (N_T) values after introducing 0.5 pore volumes of 4% Aerosol AY/OT into (a) Wurtsmith aquifer material at flow rate of 0.96 mL/min (WS-1), (b) 20-30 mesh Ottawa sand (OS-1) at a flow rate of 0.96 mL/min, and (c) 20-30 mesh Ottawa sand at a flow rate of 4.95 mL/min (OS-2).

To quantitatively compare simulated and observed mobile DNAPL bank migration, the centroids of PCE-DNAPL banks were calculated for each experiment and compared with the center of mass of the simulated PCE-DNAPL banks. The position of the simulated and measured x-axis centroids for the PCE banks versus the pore volumes of 4% Aerosol AY/OT introduced are presented in Fig. III-48. In all three experiments, the simulated mobile DNAPL bank migration rate closely matched the observed centroid migration values, with maximum discrepancies of 0.6, 0.7, and 1.6 cm for experiments WS-1, OS-1, and OS-2, respectively. The experimental data and numerical simulations presented here provide the first careful validation of the trapping number in a two-dimensional system.

Successful reproduction of PCE-DNAPL bank formation, migration, and surfactant transport confirm the validity of the total trapping number approach, and support the use of this approach for a priori predictions of DNAPL mobilization and implementation in multiphase flow and transport simulators used in the design of DNAPL source zone flushing technologies, such as surfactant flooding and nZVI injection.
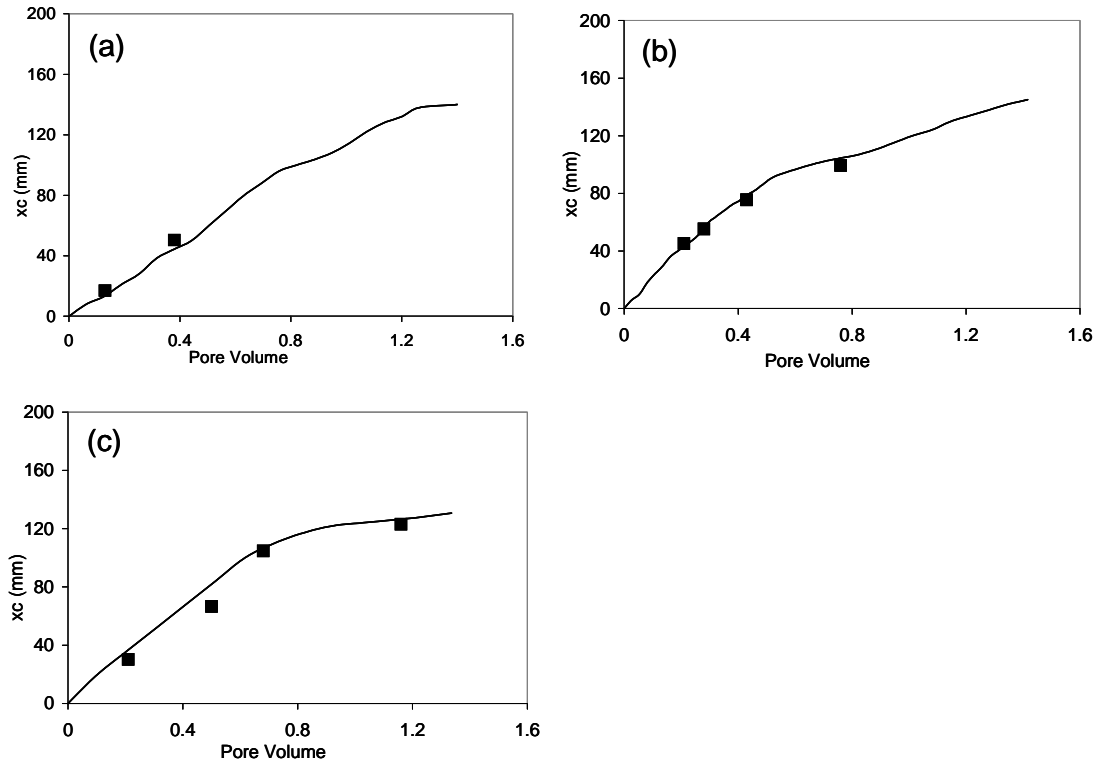
Figure III-48. Comparison of observed (square symbols) and predicted (solid lines) x-axis centroids of the PCE-DNAPL banks versus the number of pore volumes of 4% Aerosol AY/OT introduced into (a) Wurtsmith aquifer material at flow rate of 0.96 mL/min (WS-1), (b) 20-30 mesh Ottawa sand (OS-1) at a flow rate of 0.96 mL/min, and (c) 20-30 mesh Ottawa sand at a flow rate of 4.95 mL/min (OS-2).

III.4.2 nZVI Transport Modeling

Emulsion and nZVI transport experiments conducted under Task 2 were used to explore the utility of a number of mathematical modeling approaches.

III.4.2.1 Emulsion Transport Modeling

Three column experiments were simulated. Here emulsions with different formulations were introduced into columns packed with Federal Fine sand at constant flow rate of 0.86 mL/min or 0.5 mL/min. After 4 or 2.7 pore volumes, clean water was injected into the columns. In all experiments, after emulsion breakthrough, effluent emulsion droplet concentration sharply increased to a steady state plateau. After injection was terminated, the outflow concentration

rapidly decreased, followed by a prolonged elution tail. Experimental conditions are summarized in Table III-13.

Table III-13. Experimental Conditions of Emulsion Transport in Porous Media.

	A	B	C
Column length (cm)	12.50	12.8	9.83
Column diameter (cm)	4.80	4.8	4.8
Porous Media	Federal fine	Federal fine	Federal fine
Porosity	0.36	0.352	0.381
Flow rate (ml/min)	0.86	0.86	0.498
Pulse width (PV)	3.87	4	2.7
Initial concentration (wt%)	12.64	18.22	18.1
Emulsion composition	10% Tallow oil 1.14% Span 80 1.5% Tween 80	10% Tallow oil 2% Span 80 6% Tween 80 0.11% Z-Loy	10% Soy oil 2% Span 80 6.2% Tween 20 0.25% RNIP
Emulsion viscosity (cP)	1.6	2.3	2.8
Emulsion density (g/cm^3)	0.995	0.995	0.998

Continuous Time Random Walk (CTRW)

An example of emulsion breakthrough is plotted in Fig. III-49. The use of a semi-log plot here permits examination of the significant tailing observed during the water flushing period. Certain features of this breakthrough curve, i.e., its sharp rise and the extensive tailing, cannot be easily captured by a traditional advection-dispersion-reaction model that assumes equilibrium sorption. A relatively new transport modeling approach, the Continuous Time Random Walk (CTRW), was introduced by *Cortis and Ghezzehei* [2007] to simulate emulsion transport in porous media. Their model was originally applied to simulate transport data published by *Coulibaly et al.* [2006], resulting in an excellent match to the early-time sharp increase and late-time tailing behavior of those data. Motivated by that work, we investigated the potential for application of CTRW modeling theory to the experiments listed in Table III-13.

CTRW is an effective stochastic transport theory that was developed by *Berkowitz and Scher* [2001]. Its basis is the application of a continuous probability density function ψ to describe particle movement. In *Cortis and Ghezzehei* [2007], ψ was split into two distinct components: one related to the complexity of the pore space geometry, and a second term describing particle retention by means of a compound Poisson process. In the current research, a MATLAB program was developed to implement this modified CTRW model. The code was tested by successfully reproducing the modeling results published in *Cortis and Ghezzehei* [2007] and *Cortis et al.* [2006] .The program was then applied to fit the breakthrough curves of two of the emulsion transport experiments. In both simulations, a parameter γ that indicates geometrical disorder of the porous media was set to 1 to reflect a homogenous sand packing. Fitting parameters included (i) a filtration coefficient λ; (ii) a coefficient β that reflects small scale heterogeneity; and (iii) a

sticking coefficient Λ, a measurement of the average sticking time of the emulsion droplet. Fig. III-49 provides an example comparison of experimental breakthrough curve and CTRW simation results.
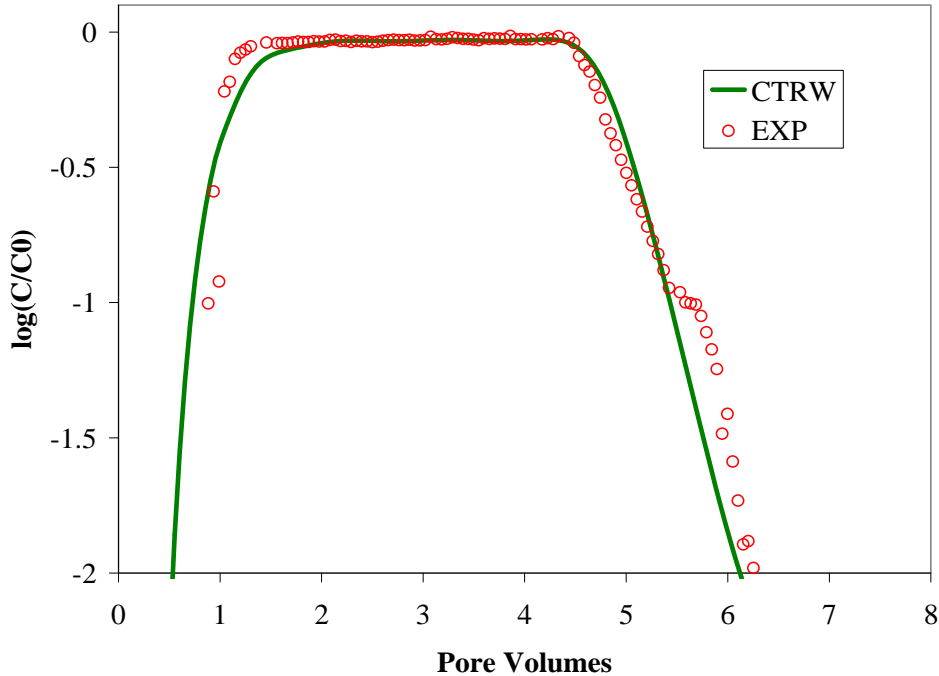
Figure III-49. Simulation of emulsion A transport in Federal Fine sand using Continuous Time Random Walk.

Inspection of the Figure reveals that the CTRW model is able to capture both the early-time sharp increase and elution tail of the emulsion breakthrough curve well. The values of the fitted filtration coefficient λ, β, and sticking coefficient Λ were 0.05 1/m, 0.2 and 0.05 respectively. Based on CTRW theory, a β value smaller than one indicates a high degree of physico-chemical surface heterogeneity at the level of the pore scale, which may be related to factors such as surface charge heterogeneity and shape, size, and surface chemistry variations of the emulsion droplets. The relatively small sticking coefficient Λ suggests that average sticking time of the emulsion droplet on the sand surface is small.

While the CTRW based approached provided reasonable simulation results for emulsion transport, it has several disadvantages. First, its application requires at least three fitting parameters for applications in homogenous media, and an additional parameter γ would be needed for heterogeneous media. Second, guidance for the prediction of CTRW model parameters is lacking, which makes it difficult to incorporate the model as a predictive module in MISER, the multiphase compositional simulator to be employed in this research. Thus, although CTRW may be used as a powerful tool to help understand the emulsion transport process, additional effort will be required to develop models that can be easily incorporated into MISER for transport prediction.

Clean-bed Filtration Theory

The clean bed filtration theory (CFT), originally developed to describe filtering of particles in water treatment, has been modified to simulate emulsion transport in several studies [e.g., *Soo and Radke,* 1985]. We tested the applicability of the CFT to model the transport of emulsions developed in this research. CFT describes the transport of colloidal particles using an advection-dispersion-reaction (retention) equation, which, in one-dimension, can be expressed as:

$$\frac{\partial C}{\partial t} + \frac{\rho_b}{\theta_w} \frac{\partial S}{\partial t} = D_H \frac{\partial^2 C}{\partial x^2} - v_p \frac{\partial C}{\partial x} \tag{29}$$

Here C is the concentration of n-C_{60} particles in solution, S is the concentration of attached or solid-phase n-C_{60} particles, t is time, x is the distance parallel to flow, ρ_b is the soil bulk density, θ_w is the volumetric water content, D_H is the hydrodynamic dispersion coefficient, and v_p is the pore-water velocity. A first-order kinetic expression is assumed to describe the (irreversible) attachment process:

$$\frac{\rho_b}{\theta_w} \frac{\partial S}{\partial t} = k_{att} C \tag{30}$$

The filtration model (Eq. 29 and 30) was applied to fit emulsion breakthrough curves of experiments A, B, and C. Fig. III-50 provides an example comparison between simulation and experimental results.
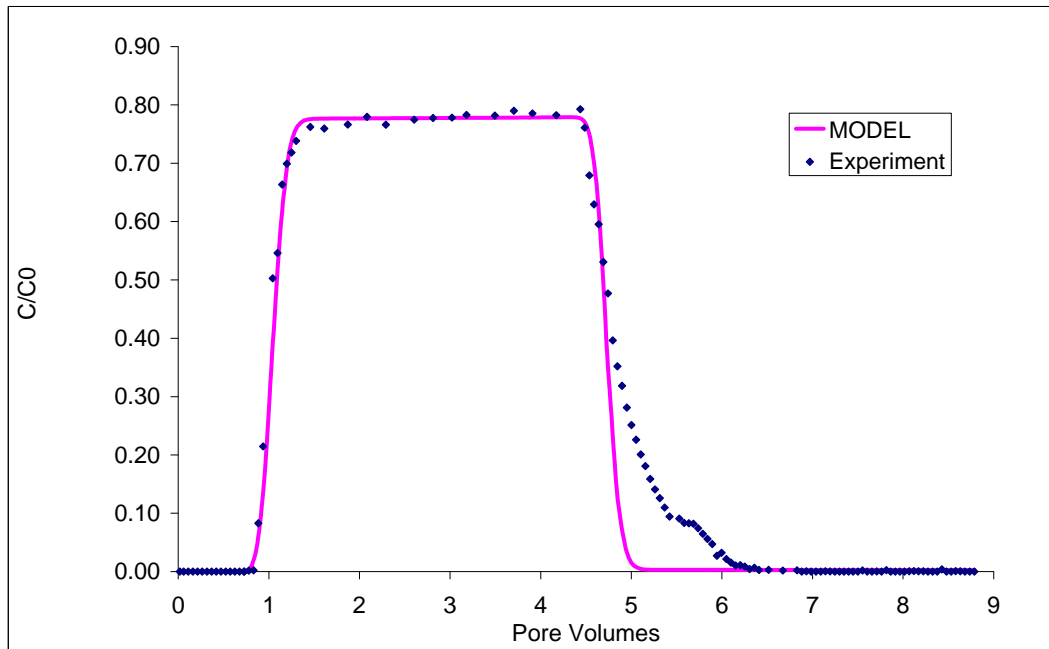
Figure III-50. Simulation of emulsion A transport in federal fine sand using filtration model.

As illustrated in Fig. III-50, the fitted CFT model can capture the rise and the plateau of the emulsion BTC, but does not reproduce the observed tailing. This discrepancy in the tailing portion of the curve could possibly be attributed to detachment, which is neglected in the traditional CFT model. When a detachment rate was incorporated into the filtration model, the simulations provided an improved fit to the breakthrough curve tailing but then failed to simulate the rapid rise in the BTC (not shown).

Modified CFT

Previous research in the PI's laboratories indicated that transport of surfactant Tween 80 in Ottawa sand may result in a Langmuir type monolayer adsorption [*Pennell et al.*, 1993]. Considering the fact that Tween was used in all three emulsion formulations, we modified the CFT model to include a (equilibrium) Langmuir adsorption term. The modified governing equation can be expressed as:

$$\frac{\partial C}{\partial t} + \frac{\rho_b}{\theta}\frac{\partial S}{\partial t} = D_h \frac{\partial^2 C}{\partial x^2} - v_p \frac{\partial C}{\partial x} - k_{att}C \qquad (31)$$

$$S = \frac{QbC}{1+bC} \qquad (32)$$

Here, Q and b are the Langmuir adsorption isotherm parameters. This model incorporates two distinct processes for emulsion attachment. One process follows the CFT and is both kinetic and irreversible. Due to the presence of surfactant, another part of the emulsion can form a monolayer surface coverage on the sand surface, which is an equilibrium (reversible) process.

In addition to the above modifications, the influence of compositional change on the flow behavior was also incorporated into the model. The viscosity and density of the fluid is considered to be a function of emulsion concentration. The permeability reduction due to attachment of the emulsion on the sand surface is also considered (based upon a change in the effective porosity). The influence of viscosity, density, and permeability on the pressure drop in the column was calculated at each time step based on Darcy's Law:

$$q = -\frac{k}{\mu}\left(\nabla P - \rho g\right) \qquad (33)$$

Eqs. 31, 32, and 33 were solved using a finite-difference method. k_{att}, Q, and b were estimated by minimizing the difference between the numerical model and the measured breakthrough curve. The fitted values for parameters k_{att}, Q, and b are listed in Table III-14. Fig. III-51 provides comparison of the experimental and simulation results for three column experiments. Fig. III-52 provides a comparison of measured and simulated pressure drop for experiment B.

Table III-14. Fitted Parameter Values for Emulsion Transport Simulation.

	K_{att} (1/h)	Q (g/gsand)	b (L/g)
A	0.199	0.004	0.075
B	1.20E-06	0.007	0.044
C	3.00E-03	0.007	0.08
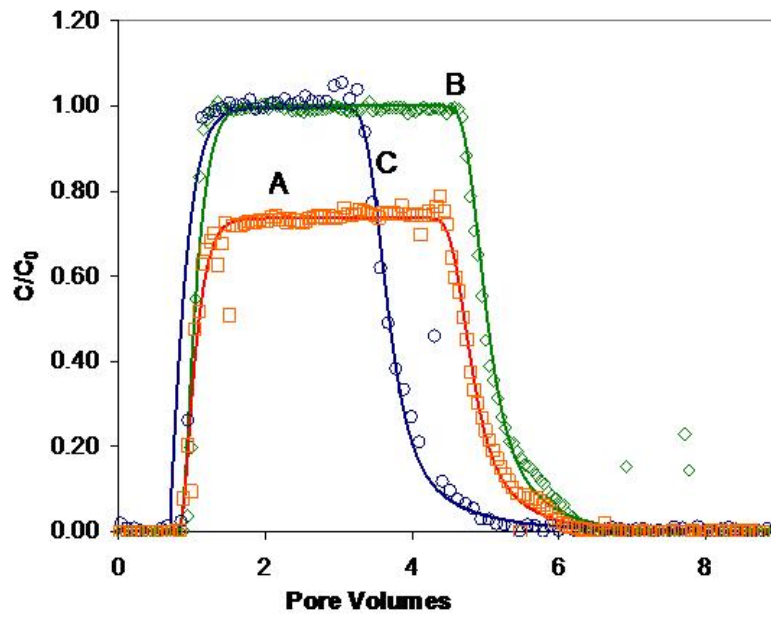
Figure III-51. Simulation of emulsion transport in federal fine sand using a modified filtration model.
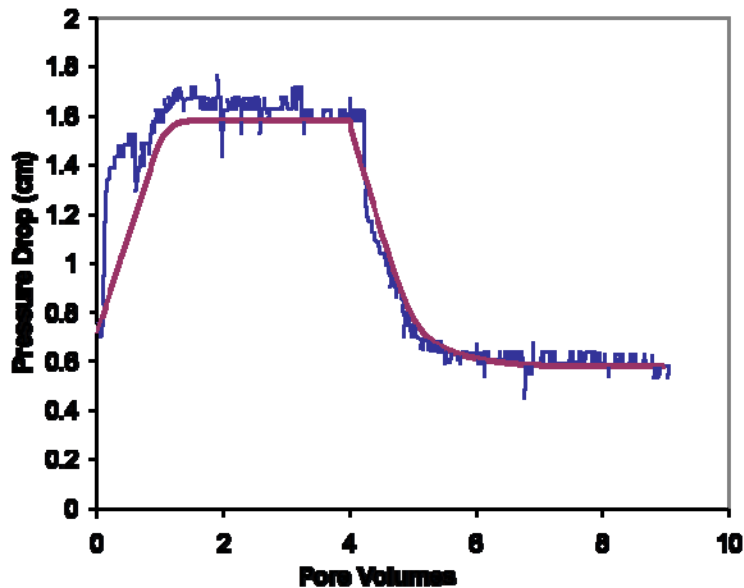
Figure III-52. Comparison of simulated and measured pressure drop for experiment B.

Examination of the Figures reveals that the modified model captures the rise, plateau and tailing of all emulsion breakthrough curves. Based upon the fitted parameter values, it appears that the emulsion attachment rate is influenced by the surfactant concentration in the formulation. A higher value of surfactant concentration is associated with a smaller the attachment rate coefficient. The tailing of the emulsion break through curves is captured well by the addition of the equilibrium Langmuir adsorption term. The similarity in magnitudes among the fitted values of the isotherm parameters for all three columns also provides further confirmation of the conceptual model. In addition, the good match between the measured and simulated pressure profiles indicates that temporal pressure drop in the column is mainly due to the influence of viscosity. Thus, injection of emulsions developed in this study is not expected to permanently reduce the permeability of the porous medium.

III.4.2.2. Simulation of RNIP transport

To elucidate the processes controlling ZVI transport, numerical simulations were conducted to simulate the RNIP transport experiments conducted in Task 2. It was observed in the experiments that RNIP particle diameters could reach 10 μm due to particle-particle aggregation. RNIP transport in Ottawa 20-30 mesh sand was only observed to occur under a high flow velocity of ca. 0.4 cm/s. In this situation, the distribution of iron in the sand column was lognormal with the greatest concentration of iron near the column inlet. CFT was applied to model the RNIP transport in this experiment. Fig. III-59 provides simulation results for the RNIP retention profile in the column. The fitted attachment rate was 5.7 1/min.
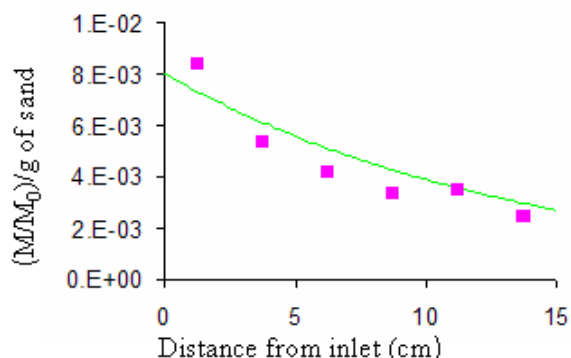
Figure III-53. Simulation of bare RNIP retention profile in column packed with 20-30 mesh sand.

To break apart the RNIP particles that aggregate in aqueous solution, the RNIP solution was sonicated before injection into the columns. Numerical simulations were also conducted to model the sonicated bare RNIP transport experiments conducted in Task 2 (see Section III.2.1). In these experiments, sonicated RNIP was introduced into the columns packed with Ottawa 20/30 mesh sand and Federal Fine sand. RNIP injection flow rates were 2.1 ml/min and 10.2 ml/min for Ottawa 20/30 mesh sand and 2.7 ml/min for Federal Fine sand. Herein, these three experiments are denoted as OTs, OTf, and FFs, respectively. Analysis of the experimental results revealed that reported mass balances, based upon comparisons of input and recovered RNIP, mass were not good (53.8~208.3%). Discussions with the experimentalists suggested that the poor mass balance was caused by difficulties in controlling and quantifying the injection concentration due to RNIP particle aggregation and settling. Since the RNIP concentration measurement for the effluent and sectioned media were believed more reliable, a constant average injection concentration was estimated based upon the total recovered mass and the volume of solution injected. Although the influent concentration likely varied over the experimental period, this simplified approach to handling the boundary condition permitted preliminary application of the simulator to explore alternative conceptual models of RNIP transport and retention behavior in columns packed with sands of different sizes and at different flow velocities.

A filtration model, based upon Eqs. 29 and 30, was employed to simulate these experiments. The best values of the attachment rate coefficient k_{att} were obtained by minimizing the sum of the squared residuals between measured and simulated retention profile data. The filtration model was able to fit the retention profiles very well with R-square values of 0.99, 0.93, and 0.98 for OTs, OTf and FFs, respectively. Corresponding fitted attachment rate coefficient values were 56.8 1/h, 48.6 1/h and 77.1 1/h. The single collector efficiency η_0, which represents the frequency of particle collision with the porous medium grain surfaces due to diffusion, sedimentation and interception, was calculated as 0.15, 0.03 and 0.10 for OTs, OTf and FFs, respectively. Calculation of the single collector efficiency (η_0) also suggested that sedimentation is the main process controlling RNIP transport in porous media, due to the high specific gravity of the iron particles.

91

III.4.2.3 Comparison of the Mobility of Emulsions, RNIP and Z-Loy

It is interesting to use modeling to compare the mobility of emulsions developed in Task 1 with that of some commercially available iron products, including RNIP and Z-Loy. Although, as indicated in the previous discussion, filtration theory failed to accurately capture all aspects of the breakthrough curves for emulsion and RNIP transport, the experimental column data suggest that attachment to the sand surface was the dominating mechanism for emulsion, RNIP and Z-Loy retention in the porous media. Thus, a comparison based on filtration theory may still be appropriate and could provide valuable insight on the relative mobility of emulsion, RNIP, and Z-Loy.

Attachment rates k_{att} for the emulsions were obtained by fitting Eqs. 31 and 32 with measured emulsion C breakthrough curves. The k_{att} value of RNIP was based on fitting the filtration model (Eqs. 29 and 30) to data from the first RNIP transport experiment presented above, where RNIP was not sonicated before injection. Note that k_{att} is presumed to be a function of particle size, hence it would be expected to increase with aggregation. The k_{att} value for Z-Loy was derived using a similar approach by fitting the model to data from a Z-Loy (Fig. III-51). Based on CFT and the fitted k_{att} values, a collision efficiency factor α can be calculated as:

$$\alpha = \frac{2}{3} \frac{d_c k_{att}}{(1-\theta_w)v_p \eta_0}$$

(34)

Here d_c is the average sand diameter, α is the attachment efficiency factor representing the fraction of particles that remain attached after collision, and η_0 is the single collector efficiency, representing the frequency of particle collision with the porous medium grain surfaces. η_0 can be estimated using the correlation:

$$\eta_0 = 2.4A_s^{1/3}N_R^{-0.081}N_{Pe}^{-0.715}N_{vdw}^{0.052} + 0.55A_s N_R^{1.675}N_A^{0.125} + 0.22N_R^{-0.24}N_G^{1.11}N_{vdw}^{0.053}$$

(35)

where A_s is the Happel correction factor, N_R is the interception number, N_{Pe} is the Peclet number, N_{vdw} is the London-van der Waals attractive forces number, N_A is the attraction number, and N_G is the gravitational number.

According to filtration theory, the attachment efficiency factor α is only influenced by the chemical interaction forces between particles and sand surfaces. The same attachment efficiency factor estimated from one column experiment should be applicable to others, if only physical conditions, such as flow rate and sand grain size, are changed. Thus, we use the α calculated based on Eqs. 34 and 35 to calculate the mobility distance, which represents the distance that particle concentration, will be reduced to 1% of the initial injection concentration:

$$L = -\frac{2d_c \ln(0.01)}{3(1-\theta_w)\alpha\eta_0}$$

(36)

Fig. III-54 presents a comparison of mobility distance for emulsion, Z-Loy and RNIP transport in porous media with grain size diameters ranged from 0.33 to 0.71 mm, representing the range

from Federal Fine sand to Ottawa 20-30 mesh sand. The inset in Fig. III-54 emphasizes the magnitude of the mobility distance of Z-Loy and RNIP. As illustrated in Fig. III-54, the emulsions developed in Task 1 possess greatly enhanced mobility compared to that of Z-Loy and RNIP.
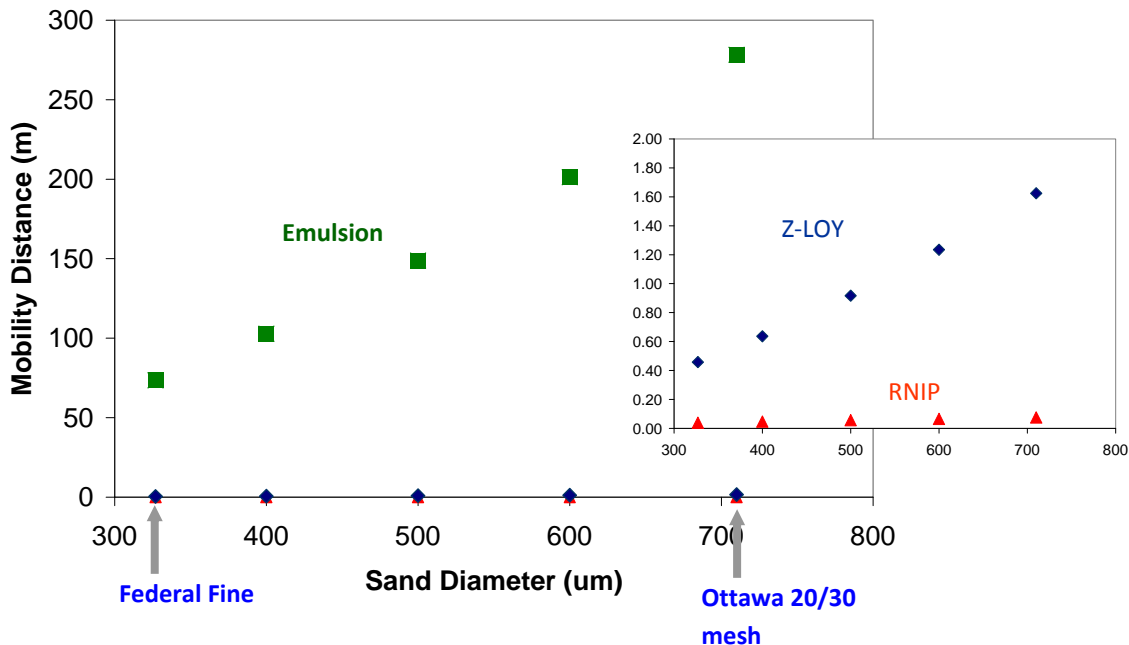
Figure III-54. Comparison of the mobility of emulsion, RNIP and Z-Loy.

III.4.3. Modeling nZVI Reactivity and Transport in DNAPL Source Zones

RNIP reactive column investigations presented in Section III.2.5 were used as the basis for the development of a nZVI source zone reactivity and transport module. Here the delivery and chemical reactivity of aqueous suspensions of nZVI particles in a two fluid phase system containing a PCE-DNAPL was modeled with a hybrid approach that accounts for the simultaneous simulation of reactive transport of ZVI particles and solutes. This simulator couples a Lagrangian Random Walk-based Particle Tracking (RWPT) method for nZVI transport with a conventional Eulerian Finite Differencing (FD) scheme for the reactive transport of solutes. Fundamental mass balance governing equations are presented in Section II.4. A complete presentation of this modeling study may be found in *Taghavy, et al*. [2010].

III.4.3.1 Mathematical Model Formulation

Reductive dechlorination reaction by ZVI was assumed to follow, as suggested by *Cundy et al*. [2008], the following general stoichiometry:

$$Fe^0 + RCl + H_2O + H^+ \rightarrow Fe^{2+} + RH + Cl^- + H_2O \tag{37}$$
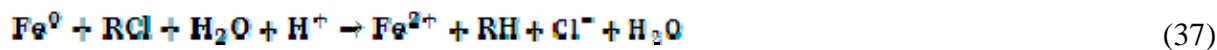
Two fluid phases are considered in the conceptual model, a flowing aqueous phase and an immobile (residual) DNAPL phase. The mathematical model consists of two phase balance

93

equations, coupled with mole balance equations for zero-valent iron and organic constituents (see equations 4-6). A component mole-balance for zero-valent iron is expressed as:

$$\frac{\partial}{\partial t}(\rho_b^{\sim}\omega_{Fe^0}^S) = -k_r \alpha_{Fe^0/PCE} C_{PCE}^W \rho_b^{\sim} \omega_{Fe^0}^S \tag{38}$$

where $\rho_b^{\sim}$ (kg/m) is the bulk density of the dry sand, $\omega_{Fe^0}^S$ (mole Fe^0/kg of dry sand) is the molar-based Fe^0 concentration; k_r (m^3/s mol) denotes the first-order PCE reduction rate constant normalized by the number of moles of Fe^0 per unit volume of aqueous phase, $\alpha_{Fe^0/PCE}$ (mol/mol) is the stoichiometric ratio of the number of moles of Fe^0 consumed to reduce 1 mole of PCE to ethene, and C_{PCE}^W (mM) is the molar-based aqueous concentration of PCE. The implemented single step reaction kinetic equation (Eq. 38) for PCE dechlorination to ethene was chosen based upon experimental measurement of ethene as the only detectable reaction product.

The nZVI particles are assumed immobile following their delivery, consistent with experimental observations described in Section III.2.5. In addition, the influence of pH on PCE dechlorination rate is neglected, consistent with experimental observations of TCE dechlorination by nZVI particles [*Liu and Lowry*, 2006]. The high buffering capacity of most soils also implies that there will be little pH change with a typical injection of nZVI [*Liu and Lowry*, 2006]. Anaerobic corrosion of iron with water was considered negligible relative to consumption of iron via the dechlorination reaction. [*Liu et al.*, 2005] Here reaction with nZVI is considered to be a surface reaction. [e.g., *Liu et al.*, 2005] Changes in the specific surface area of nZVI particles with time were neglected, consistent with the experimental observations of *Liu and Lowry* [2006]. In Eq. 38, reduction reaction kinetics are assumed to be first-order with respect to both the Fe^0 content of nanoparticles and the aqueous-phase concentration of PCE. Most studies report that the degradation of chlorinated organic compounds by Fe^0 proceeds by pseudo-first-order kinetics with respect to contaminant concentration [e.g., *Liu and Lowry,* 2006]. Although *Liu and Lowry* [2006] found that reduction of TCE was zero-order with respect to Fe^0 content over the life of the particles in their batch experiments, the Fe : TCE molar ratio they employed was very large (>1000). In DNAPL source zones, however, where the achievable Fe:TCE molar ratio would likely be lower, due to the larger contaminant mass , Fe^0 availability could become a limiting factor (the initial Fe0 : PCE molar ratio in the present study was ca. 11.4). Hence, based upon the documented evidence and the experimental conditions of our column study, the nZVI-driven dechlorination reaction was assumed first-order with respect to Fe^0 concentration and aqueous phase organic concentration, enhancing the overall reaction kinetics to the second order. (For more detail on justification of the conceptual assumptions herein, see *Taghavy et al.* [2010]).

The ADR-based component mole-balance equations for dissolved phase PCE and ethene are given as:

$$\frac{\partial}{\partial t}(\phi S_w C_{PCE}^W) + \frac{\partial}{\partial x}\left[\phi S_w \left(C_{PCE}^W V_w - D_{W_{PCE}}^h \frac{\partial C_{PCE}^W}{\partial x}\right)\right] = -k_r C_{PCE}^W \rho_b^{\bullet} \omega_{Fe^0}^S + k_f a_0 \left(C_{PCE}^{sat} - C_{PCE}^W\right) \tag{39}$$

and

94

$$\frac{\partial}{\partial t}\left(\phi S_w C_{ethene}^W\right)+\frac{\partial}{\partial x}\left[\phi S_w\left(C_{ethene}^W V_w - D_{W_{ethene}}^h \frac{\partial C_{ethene}^W}{\partial x}\right)\right] - k_r C_{CE}^W \rho_b^* \omega_{Fe^0}^* \tag{40}$$

where C_i^W (mM) is the aqueous phase organic concentration, ϕ (-) is the effective porosity of the sand taking into account the pore space occupied by the emplaced Fe^0, S_w is the aqueous phase saturation, V_w (m/s) is the interstitial velocity of the aqueous phase, and $D_{W_i}^h$ (m²/s) denotes the hydrodynamic dispersion coefficient of dissolved organic in the aqueous phase. The second term on the right-hand-side of Eq. 3 is a linear driving force expression, based on the assumption that NAPL dissolution in the aqueous phase is a rate-limited process controlled by diffusion across the stagnant water layer surrounding an entrapped NAPL droplet [*Powers et al.*, 1994]. C_{PCE}^{sol} (mM) is the molar aqueous solubility limit of pure phase PCE, k_f (m/s) and a_0 (m²/m³) are the mass transfer rate coefficient and the specific surface area of the NAPL blobs per unit volume of medium, respectively Here, $k_f a_0$ was estimated as a function of the system hydrodynamics, pore structure, and volumetric fraction of NAPL in the pore space from a dimensionless Sherwood number (Sh') correlation presented by *Powers et al.* [1994]:

$$Sh' = \frac{\hat{k} d_{50}^2}{D_L^{PCE}} = 4.13 Re'^{0.598} \delta_g^{0.673} U_{i_g}^{0.369} \left(\frac{\theta_n}{\theta_{n_0}}\right)^{0.510 + 0.114\delta_g + U_{i_g}} \tag{41}$$

in which $\hat{k}$ (1/s) is a lumped mass-transfer coefficient ($\hat{k} = k_f a_0$), d_{50} (m) is the median grain diameter, D_L^{PCE} (m²s⁻¹) is the free liquid diffusivity of PCE in water, Re' is the dimensionless Reynolds number, δ_g (-) is the normalized median sand grain diameter ($\delta_g = \frac{d_{50}}{d_M}$), where d_M (m) is taken as the diameter of a "medium" sand grain ($d_M = 5 \times 10^{-4} m$), and U_{i_g} (-) is the uniformity index of the sand.

A multiphase extension of Darcy's Law [*Abriola et al.*, 1997] is used to express the aqueous phase mass balance:

$$\frac{\partial}{\partial t}(\phi \, \hat{\rho}_w S_w) = \frac{\partial}{\partial x}\left[\hat{\rho}_w \lambda_w \left(\frac{\partial P_w}{\partial x} - \hat{\rho}_w \bar{g}\right)\right] \tag{42}$$

where $\hat{\rho}_w$ (g/m³) is the mass density of the aqueous phase, S_w (-) is the saturation of the aqueous phase, $\bar{g}$ (m/s) is the gravitational acceleration vector, and λ_w (m³ s/g) is the mobility of the aqueous phase ($\lambda_w = k \frac{k_{rw}}{\mu_w}$), where k (m²) is the intrinsic permeability of the medium, k_{rw} (-) denotes the relative permeability of the aqueous phase, and μ_w (g/m s) is the aqueous phase dynamic viscosity. Here the influence of interphase mass-transfer on the aqueous phase mass balance is neglected. For this pure phase PCE contamination, the mass balance for the NAPL phase is written in terms of moles as:

95

$$\frac{\partial}{\partial t}(\phi \, \rho_n s_n) = -k_f a_0 \left(C_{PCE}^{sol} - C_{PCE}^W \right)$$

<div align="right">(43)</div>

where ρ_n (mol m^{-3}) is the molar density of the NAPL phase. Water phase saturation is obtained by assuming that pore spaces are fully saturated with the two liquid phases ($S_w + S_n = 1$). Changes in NAPL phase density due to back-partitioning of reaction products (i.e. ethene) were neglected. The mass of organic constituents sorbed by the solid phase was assumed negligible relative to the mass existing as PCE-DNAPL and dissolved in the aqueous phase.

III.4.3.2. Mathematical Model Simulations

The numerical model, developed from the mathematical model described above was used to simulate the measured effluent concentrations. Values of the model input parameters are provided in Table III-15. Only one modeling parameter was fit to reproduce experimental results, an effective PCE reduction reaction rate constant (k_r) of 1.42 1/hr, which provided a close match to the measured effluent data (Fig. III-55). When normalized by the mass of nZVI per unit aqueous phase volume, the value of this rate constant is 3.9×10^{-3} L/hr g (equivalent to 1.70×10^{-4} L hr^{-1} m^{-2} assuming a specific surface area of 23 m^2/g for RNIP particles as reported by *Liu et al.* [2005]. These rates are approximately one order-of-magnitude smaller than the continuously mixed batch reactor (CMBR)-based dechlorination rate constant of 7.1×10^{-2} L/hr g reported by *Liu et al.* [2005] for TCE with RNIP, and one order-of-magnitude larger than the CMBR-based pseudo first-order rate constant of (4.8×10^{-4} L hr^{-1} g^{-1}) measured by *Doong and Lai* [2006] for dechlorination of PCE with micron-sized iron powder (measured specific surface area of 0.14 m^2/g). These rate data presumably reflect the inherent differences in the mixing conditions of columns and batch reactors, the variation in available reactive surface sites for different ZVI materials, and the difference in the reactivity of the PCE and TCE, thus precluding direct comparisons.
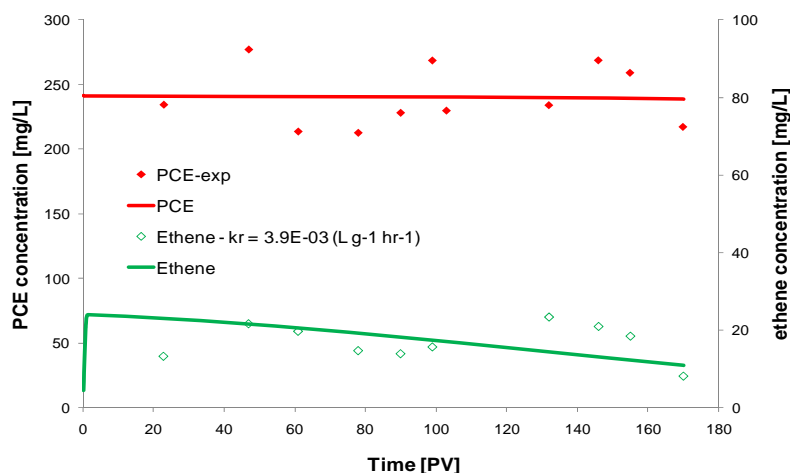
Figure III-55. Experimental and model breakthrough curves of dissolved-phase PCE and ethane.

Table III-15. Summary of experimental properties and model input parameters.

Property	Units		Source/Reference
Column porosity	-	0.354	Gravimetric measurement
Effective column length	cm	16.1	Gravimetric measurement
Column pore volume	mL	28.0	Gravimetric measurement
Darcy velocity	m/day	0.73	Gravimetric measurement
Peclet number	-	50	Estimated from bromide tracer test
Median blob diameter	mm	0.5	*Powers et al.*, 1994
Median sand grain diameter	mm	0.71	*Cho and Annable*, 2005
Uniformity Index	-	1.21	*Cho and Annable*, 2005
Sand grain density	g/cm^3	2.65	
Fe particle density	g/cm^3	7.784	*Kaye and Laby*, 1995
Viscosity of Water	$g/m^{.}s$	1.0	
Viscosity of PCE	$g/m^{.}s$	0.89	*Qin et al.*, 2007
Aqueous diffusivity of PCE	cm^2/s	$1.02{\times}10^{-5}$	*Chiao et al.*, 1994
Aqueous diffusivity of ethene	cm^2/s	$8.8{\times}10^{-6}$	
PCE-DNAPL saturation	%	5.5	Estimated by volume and weight
PCE equilibrium solubility	mg/L	250	*Pennell et al.*, 1994
Mass of iron in the column	g	40	
Initial Fe^0-content of particles	%	24	Measured by digestion in hydrochloric acid from the amount of hydrogen production
Fe^0 : PCE Stoichiometric ratio	-	4.0	
Initial Fe^0 : PCE molar ratio	-	11.4	Measured experimentally

The fitted model predictions of PCE-DNAPL saturation distribution, Fe^0 content, and dissolved species (PCE and ethene) at various times are presented in Fig. III-56. Model mass balance results indicate that, after flushing with 170 PV of aqueous solution, 7% of the initial Fe^0 mass emplaced in the column was consumed in the dechlorination of approximately 20% of the initial mass of PCE-DNAPL to ethene (measured in effluent samples), while experimental measurements showed that 40% of the initial mass of PCE-DNAPL was dissolved from the column at the aqueous solubility limit (Fig. III-56). Approximately, 40% of the initial mass of PCE-DNAPL remained in the column at the conclusion of the simulation period (i.e. 170 PV).

If only dissolution had occurred (i.e. no reaction), according to model prediction 58% of the initial mass of PCE-DNAPL would have remained in the column after a 170 PV injection of aqueous solution. At 170 PV, the model predicts the complete dissolution/transformation of PCE-DNAPL near the influent end of the column, with saturations increasing to a residual of 4.4% near the effluent (Fig. III-56a). The model also predicts that less Fe^0 consumption occurs closer to the column inlet (Fig. II-56b), consistent with near zero dissolved-phase PCE concentrations as the experiment proceeds (Fig. II-56c). The model also predicts that effluent ethene concentrations should gradually decrease over time. This decrease in concentration is attributed to two factors: (1) decrease in Fe^0 content of RNIP particles which render them less reactive over time, and (2) the gradual decrease in dissolved PCE residence time in the column

as the PCE-NAPL is gradually dissolved from the influent end of the column. The latter effect is more significant, however, as only 7% of the Fe^0 mass was estimated to be consumed during the course of experiment.

III.4.3.3. Sensitivity Analysis

A model sensitivity analysis was performed and for all simulations, the total simulation time was adjusted to allow for complete removal of contaminant mass from the domain. Different input parameters such as the emplaced nZVI concentration, the aqueous flow rate, and the emplaced nZVI zone length were varied in this analysis.   Several model outputs were examined, including a dimensionless PCE Transformation Efficiency Index (TEI), and effluent concentrations of dissolved phase PCE and ethene concentrations. The dimensionless TEI is defined here as the ratio of the total moles of reaction products (i.e. ethene) recovered in the effluent to the initial moles of emplaced PCE-DNAPL, representing the percentage of the initial contaminant mass present in the source zone that has been transformed to ethene.
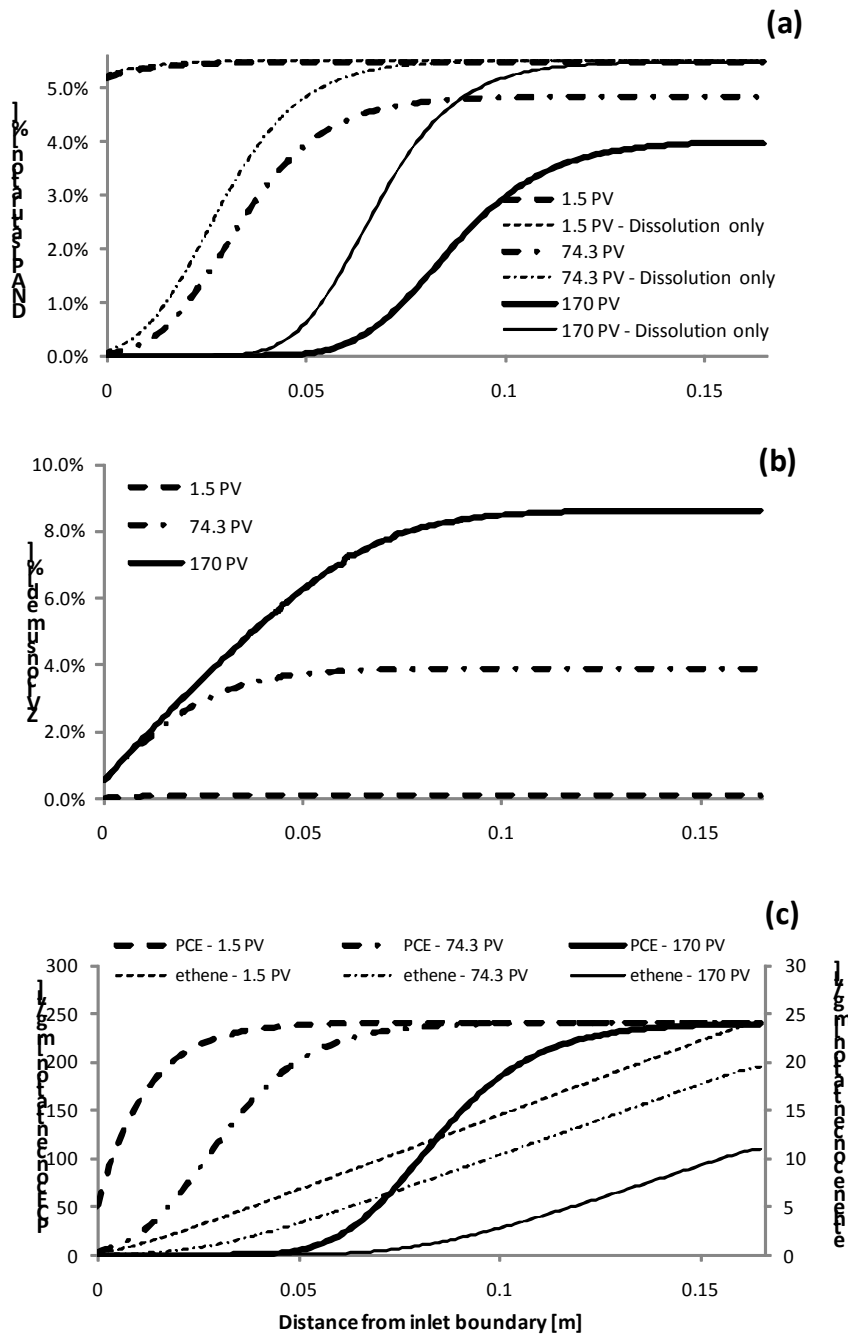
Figure III-56. Spatial distribution profiles of (a) DNAPL saturation, (b) Fe^{0} content of soil, and (c) dissolved PCE and ethene concentrations at different simulation times.

III.4.3.3.1 Sensitivity to Emplaced Iron Concentration

The emplaced nZVI concentration in the experimental system was higher than reported values from documented pilot-scale field-injection studies. In one pilot test, *Henn and Waddill* [2006] reported an average nZVI content of 10-15 g_{Fe}/kg soil over the injection field. This estimated value is more than one order of magnitude lower than that in our column experiment. *Zhang* [2003] reviewed the results from a field demonstration of nZVI injection where the average Fe^0 content was on the order of 1×10^{-2} g_{Fe}/kg soil, more than five orders of magnitude lower than the experimental column system presented in this report. To explore the sensitivity to the amount of iron emplaced, the emplaced iron concentration ($\omega_{Fe, exp}$ =283 g/kg dry soil) was varied over a one order of magnitude range (from 283 to 28.3 g_{Fe}/kg dry soil). Simulation results indicate that a decrease in emplaced iron concentration was associated with an increase in the mass of PCE-DNAPL remaining in the source zone at 170 PV, and a decrease in PCE transformation efficiency. A one order of magnitude decrease in iron concentration (from 283 to 28.3 g_{Fe}/kg dry soil) resulted in an increase in PCE-DNAPL mass remaining (from 40% to 56%), and resulted in an order-of-magnitude decline in the PCE TEI, (from 25.2% to 3.0%) (Fig. III-57). These simulations suggest that, under typical field loadings, even for very favorable emplacement conditions, much of the PCE would dissolve from the source zone, potentially migrating (untransformed) downstream to a receptor point.
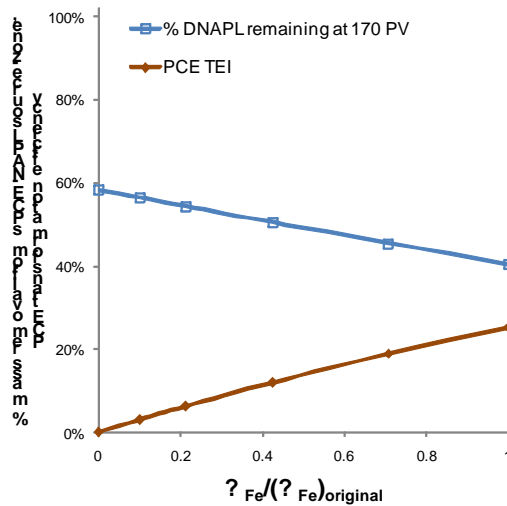
Figure III-57. Influence of initial emplaced nZVI concentration on DNAPL mass remaining in the source zone and PCE transformation efficiency.

III.4.3.3.2 Sensitivity to Flow Rate

The applied experimental volumetric flow rate resulted in a pore water velocity of 2.1 m/day, which is at the upper range of typical groundwater velocities (0.15-1.4 m/day in shallow sandy aquifers [*Kunkel and Wendland*, 1997]). Thus, the influence of pore-water velocity on treatment efficiency was explored over a two order of magnitude range (from 2.1 m/day to 0.021 m/day). The sensitivity to flow velocity can be attributed to the increase in retention time of dissolved

contaminant in the column. An increase in the residence time is associated with an increase in the reaction (contact) time and, consequently, with the production of reaction products (i.e., ethene).For an identical volume of water flushing, decreasing the flow rate to 2.5×10^{-2} mL/min resulted in an increase in the PCE TEI from 25% to 81%, and an increase in DNAPL removal (from 60% to 99.8% of the initially emplaced mass of DNAPL at 170 PV) (Fig. III-58). Further decreasing the flow rate to 2.5×10^{-3} mL/min increased the PCE TEI to 99%. Approximately, one-third of the initial mass of Fe^0 was consumed under these conditions. Although the contaminant transformation efficiency increases at lower flow rates, the time-length of DNAPL persistence also increases. The time to complete DNAPL removal increased by an approximate factor of 3 when the flow rate decreased by one order of magnitude from 2.5×10^{-2} mL/min to 2.5×10^{-3} mL/min. In addition, the sensitivity analysis indicates that regardless of the flow rate, the effluent concentrations of dissolved PCE remain >100 mg/L until significant removal of PCE-DNAPL from the source zone. Also plotted in Fig. III-58 (dotted curves), are results for simulations at a lower nZVI content (ω_{Fe} =28.3 g/kg) more representative of field test conditions. At this lower emplaced nZVI concentration, the PCE TEI increases (one order of magnitude) from 3% to 16% and then to 27% as flow rate decreases from 0.25 mL/min to 2.5×10^{-2} mL/min and then to 2.5×10^{-3} mL/min. This suggests that even with a substantial reduction in flow rate, high transformation efficiency is not expected unless the emplaced iron concentration within the DNAPL source zone is greater by orders of magnitude than the reported values from field applications of nZVI. The simulations also suggest that, under the reduced flow conditions, an ethene gas phase would evolve in the pore space, potentially resulting in significant gas accumulation sufficient to occupy a volume 12 times greater than the column pore volume.
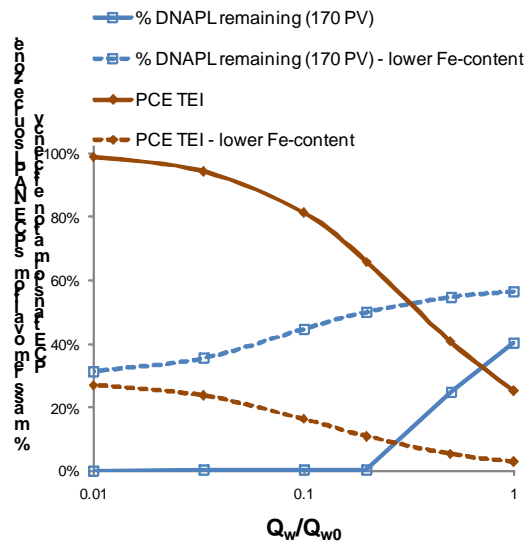
Figure III-58. Influence of flow rate on DNAPL mass remaining in the source zone and PCE transformation efficiency index. Here lower Fe content=28.3 g/kg.

III.4.3.3.3 Sensitivity to the Length and Spatial Distribution of the nZVI Zone

Maintaining the original column conditions (i.e., nZVI content, length, PCE-DNAPL saturation, flow rate, and simulation time), a second column containing nZVI at the same concentration level was placed at the effluent end of the initial column. Placement a reactive zone down-

gradient from a DNAPL source zone does not result in the enhanced dissolution of DNAPL, but does reduce the down-gradient aqueous PCE concentration eluting from the source zone. As anticipated, this resulted in a substantial enhancement of dissolved PCE transformation (see Fig. III-59). When the reactive zone was extended for 83.4cm, for the emplaced iron concentration of 283 g_{Fe}/kg, the PCE TEI was 96% (Fig. III-59). To achieve near complete conversion of PCE-DNAPL to ethene (>99%), the length of the 2nd column must be increased to 133.4cm (a 9-fold increase of the emplaced nZVI mass). Here the breakthrough PCE concentrations decreased by two orders of magnitude, while the predicted effluent concentrations of ethene tripled. Additional, these simulations reveal that a significant enhancement in the PCE conversion efficiency can be achieved only by changing the spatial distribution of the nZVI particles. This can be seen by comparing two scenarios. The first case is the original column scenario (initial 0.172 mole of Fe^0), and the second case is the increased nZVI zone length ($L_{ZVI} = 150$cm) at the lower emplaced nZVI content (initial 0.155 mole of Fe^0). The PCE TEI was found to increase significantly from 25% to 38% (i.e. >50% enhancement), when the mass of nZVI was distributed down-gradient of the source (case #2) instead of being densely packed in the DNAPL source zone (case #1).

III.4.3.3.4 Damköhler Number Analysis

A *Damköhler* number analysis was performed to find a metric for predicting the PCE TEI from the physiochemical and hydrodynamic characteristics of a system of interest. Such a metric would be beneficial in the design of nZVI-based remedial schemes for treatment of DNAPL source zones. An initial *Damköhler* type (I) (Da_I) was employed to characterize the relative importance of reaction kinetics to advection for PCE transport through the multiphase system containing entrapped PCE-DNAPL ganglia. Da_I was computed using the following expression:

$$Da_I = \frac{\hat{k} \cdot l_R}{v_w} \tag{44}$$

where $\hat{k}$ [1/s] is an effective reaction rate coefficient, l_R [m] is the average contact length of the contaminant in the reactive zone, and v_w [m/s] is the pore water velocity.

By substituting the effective reaction coefficient with the normalized PCE dechlorination rate, k_r [L/hr g] in Eq. 44, the following expression is derived:

$$Da_I = \frac{\left(k_r \cdot \dfrac{\rho_b \omega_{Fe}^s f_{Fe^0}^{init}}{\overline{\phi S_w}} \right) \cdot \left(L_{ZVI} - 0.5 L_{PCE} \right)}{\dfrac{q_w}{\phi S_w}} \tag{45}$$
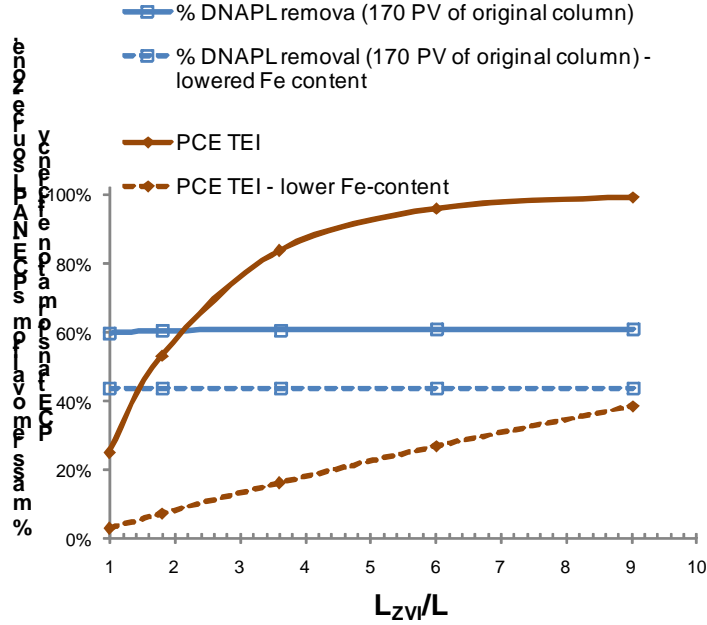
Figure III-59. Influence of downstream nZVI zone on DNAPL mass remaining in the source zone and PCE transformation efficiency index. Here lower Fe content=28.3 g/kg.

where the second term in the numerator is the initial average contact length of dissolved PCE in the reactive zone. Simplifying the terms in Eq.45 yields the following expression:

$$Da_I = k_r \rho_b f_{Fe^0}^{init} \omega_{Fe}^s \frac{L_{ZVI} - 0.5 L_{PCE}}{q_w} \tag{46}$$

Results of the *Damköhler* number analysis are presented in Fig. III-60, which reveals that Log Da_I exhibits the same relation with the PCE TEI, independent of nZVI zone length (Fig. III-60(a)). However, it is also apparent that the Da_I scaling does not work under reduced flow conditions. However, as shown in Fig. III-60(b), use of a modified *Damköhler* number $\hat{Da}_I$ resulted in a similar Log $\hat{Da}_I$-PCE TEI relationship for all of the scenarios considered. Here, $\hat{Da}_I$ is defined as:

$$\hat{Da}_I = Da_I \cdot \left(\frac{L_{ZVI}}{L_{obs}} \right)^{0.5} \tag{47}$$

where L_{obs} [m] is the distance between the upstream end of the reactive zone and the location of the observation point for PCE TEI measurement, here the length of the longest column considered in the sensitivity study (i.e. L_{obs}=1.5m). A log-linear relationship between $\hat{Da}_I$ and PCE TEI was observed within a wide PCE TEI range of values (10% - 95%) with an r^2 value of 0.988 (Fig. III-60(c)).

103
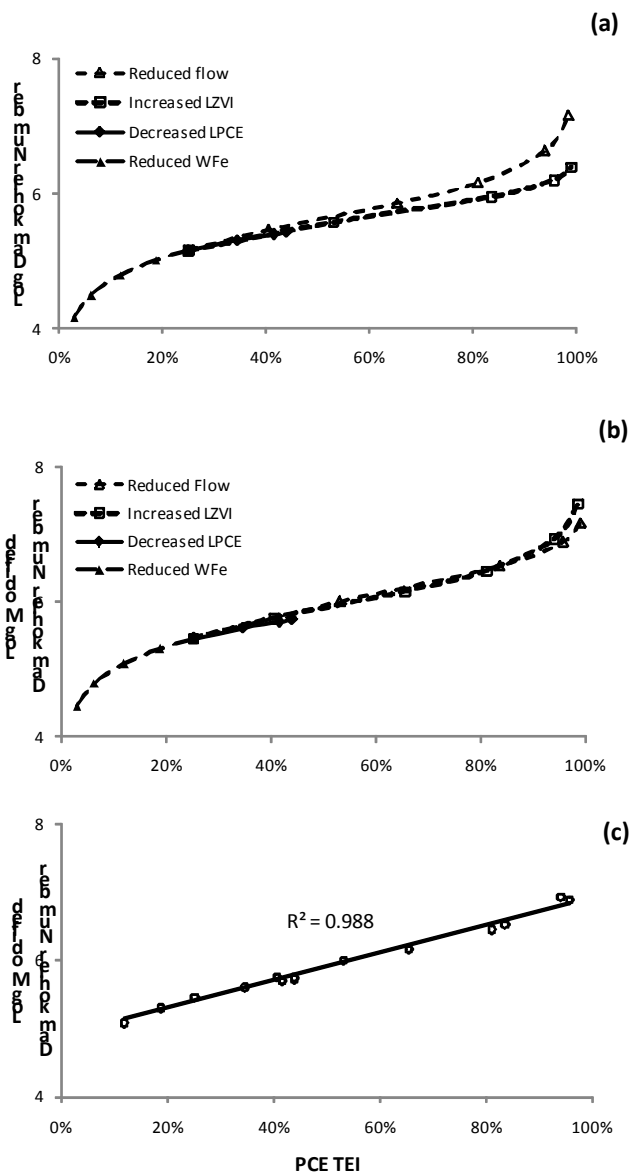
Figure III-60. Logarithmic diagrams of (a) Da_I -PCE TEI, (b) modified Da_I-PCE TEI relations, and (c) range of linearity of Log modified Da_I -PCE TEI relationship.

III.4.4. Field Scale Simulation

Preliminary efforts were also devoted to exploring the potential performance of nZVI based DNAPL remediation technologies at the field scale. Nanoscale iron reduction of TCE in DNAPL source zones is considered a promising remediation technology. Here the primary remediation mechanism is reduction of TCE in the aqueous phase, coupled with the enhancement of DNAPL dissolution by increasing the aqueous phase TCE concentration gradient. Most previous iron reactivity studies have been conducted in batch systems, and thus, dissolution enhancement has not been quantitatively evaluated. In field applications, it is also anticipated that the saturation distribution in a DNAPL source could influence the efficiency of nanoscale iron reaction. To explore these factors, hypothetical remediation scenarios were mathematically modeled to investigate the potential dissolution enhancement created by the iron reaction and its corresponding effect on source zone longevity. For these simulations, MISER was modified to include iron reaction with dissolved TCE. The reaction kinetics employed in the simulator were based on batch experiments conducted by *Liu et al.* [2005]. A diminishing sphere model proposed by *Powers* [1992] was used for calculation of the rate limited TCE dissolution.

Hypothetical remediation scenarios were selected to explore the remediation efficiency of bare RNIP in removing TCE in the aqueous phase. DNAPL source zones with a high ganglia to pool ratio (GTP), medium GTP, and low GTP were investigated. Simulation results predicted that it would require 3, 20, and 60 years to remove 98% total TCE mass (156 kg) in these source zones with GTP of 65, 1.0 and 0.17 respectively. These results suggest that the efficiency of ZVI for DNAPL remediation may be limited by interphase mass transfer processes (i.e., dissolution), if the reduction reaction can only occur in the aqueous phase. When considering dissolution only (GTP = 1.0), removal of 98% of the mass is predicted to take 216 years. Fig. III-61 provides three representative DNAPL source zones with high, medium and low GTP. Fig. III-62 presents their corresponding source zone longevity.

GTP = 65   GTP = 1.0   GTP = 0.17   TCE Saturation
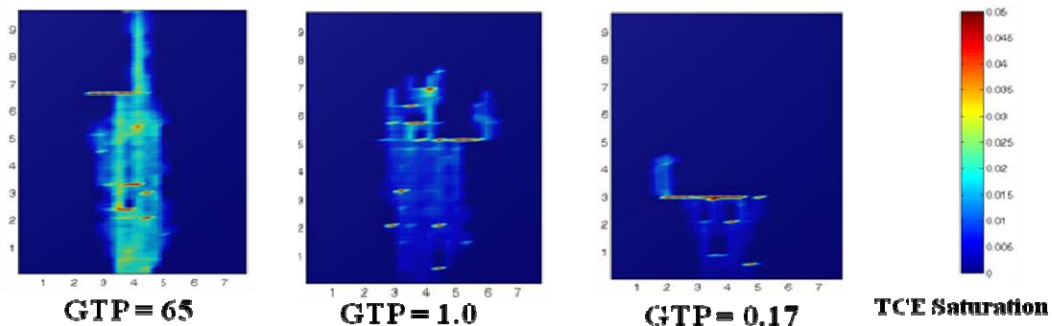
Figure III-61. Three representative DNAPL source zones with high, medium and low GTP.
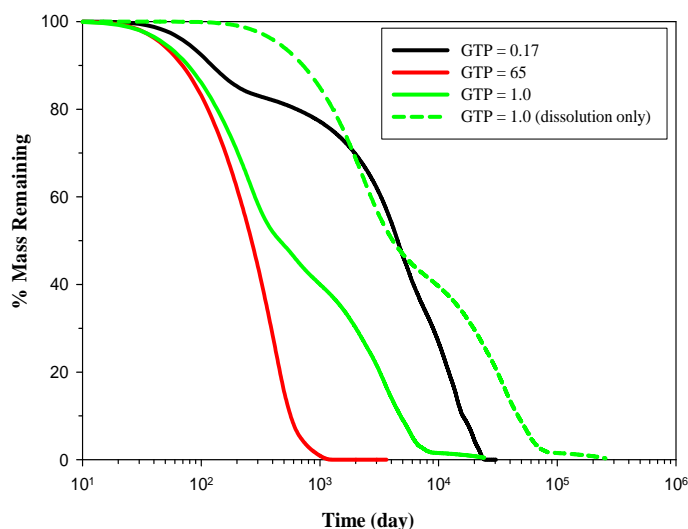
Figure III-62. Percentage of mass remaining verse time for three representative source zone with high, medium and low ganglia-to-pool ratio when using RNIP for remediation.

IV. Conclusions and Recommendations for Future Research/Implementation

The most significant findings of this research and their implications are listed in bullet form below:

Task I: Development, characterization, and refinement of nanoscale iron delivery systems

- Batch investigations of TCE reactivity in aqueous solutions of iron nanoparticles demonstrate that iron content alone is not a good predictor of TCE transformation rates. Comparisons of pseudo-first-order degradation rates observed in experiments employing RNIP and MTI iron suggest that the presence of a magnetite oxide layer on the RNIP surface plays an important role in providing enhanced TCE transformation efficiency.

- Observed surface-area normalized TCE transformation rates for Z-Loy, a commercially available iron product that contains Fe^0 supported on an aluminum ceramic core, were comparable to values obtained for solid iron particles (2.0-14.0 $x10^{-3}$ $hr^{-1}m^{-2}$).

- Development of stable oil-in-water emulsions containing coated RNIP was feasible for systems with properties favourable for transport within DNAPL zones. Emulsions developed (with soybean oil and food-grade surfactants) had mean droplet diameters between 1 and 2 μm, remained kinetically-stable for greater than 1.5 hr, and possessed densities in the range 0.996-1.00 g/mL at 22°C and dynamic viscosities between 2.4-9.3 mPa·s at 22°C. Stability of commercially available nano iron products tested (RNIP,

106

polymer-modified RNIP, and Z-Loy) was shown to be substantially inferior to the developed oil-in-water emulsions.

- One particular emulsion formulation, stabilized with gum arabic (GA), exhibits promising characteristics that suggest potential for superior *in situ* remediation treatment performance. Emulsion droplet size and kinetic stability are favorable for porous media transport, while the combination of relatively high IFT with TCE-NAPL and low viscosity suggest limited potential to mobilize DNAPL during delivery. In addition, TCE conversion in the GA emulsion system compared favorably to rates observed in aqueous suspensions of coated iron particles, while stabilizing high concentrations of nZVI.

- Experiments exploring nZVI reactivity within a TCE-NAPL phase revealed that reactions within the NAPL are as efficient, with respect to iron consumption, as reactions occurring within the aqueous phase. Observed dechlorination rates were proportional to the concentration of (soluble) water present within the NAPL. Although the amount of soluble water limited rates of TCE transformation within the NAPL, no sign of deactivation was observed over the period investigated (~5 to ~15hr), suggesting the potential for sustained reaction.

Task II: Transport and reaction of nanoscale iron in a representative porous medium

- High-concentration RNIP injection experiments suggest that RNIP particle transport is greatly influenced by particle aggregation, and is limited to relatively small travel distances for reasonable injection pressures. Observed increases in pressure in these experiments were attributed to blockage of pore throats, which occurred even in coarse sands. Only modest improvements in transport rate were observed for modified RNIP in comparison to those of bare RNIP. The addition of Tween 80 to the solution, however, substantially increased the distance and rate of RNIP transport.

- Despite Z-Loy's more favorable stability and transport parameters, high mass retention (>97%) and limited transport were observed in column injection experiments. This behavior was attributed to the substantial hydrogen gas production observed within the column, which acted to blocked pores.

- In contrast to RNIP and Z-Loy injection experiments, column experiments revealed that emulsions were transported with little retention (<0.20% wt.) in medium and fine sands at velocities attainable under typical field conditions. In addition, results of a total trapping number analysis indicate that injection of the developed iron-containing emulsions present little potential for mobilization of TCE-DNAPL entrapped within fine- and medium-grained sands at these velocities. These results suggest that encapsulation may be a promising method for field delivery of nZVI.

- Injection experiments in columns with an entrapped NAPL phase suggest that, for surfactant-stabilized RNIP suspensions, the potential exists for partial mobilization of entrapped PCE-DNAPL during RNIP delivery. Thus, site-specific evaluation of

mobilization potential becomes crucial to a successful remedial design. In addition, although emulsion injection did not act to mobilize entrapped TCE-NAPL, column experiments revealed that substantial TCE was solubilized during an emulsion flush. Thus, potential for NAPL solubilization must also be considered in field deployment of this technology.

- Column experiments employing unmodified RNIP for in situ treatment of an emplaced PCE-DNAPL source zone demonstrated substantial conversion of PCE to ethene (20%). However, even though nZVI was successfully delivered to the source zone at a high concentration (60 g/L), observed effluent concentrations of PCE persisted at or near the solubility limit throughout the duration of the experiment.

Task III: Contaminant Mass Reduction in Heterogeneous Media

- Two-dimensional aquifer cell injection experiments with unmodified and surfactant-stabilized RNIP confirmed conclusions from the column transport investigations. Cell observations demonstrated that transport was limited to a small zone around the injection point and no further migration of the nanoparticle front was observed once injection ceased.

- Similarly, aquifer cell Z-Loy injection experiments confirmed column observations. The injected Z-Loy solution failed to migrate far beyond its injection point, and subsequent to injection, flow bypassing of the injection zone was observed, potentially attributed to production of hydrogen gas and pore clogging. Although some reaction products were detected in the aquifer cell following shut in periods, most of the source zone TCE-DNAPL mass removal during the experiment was attributed to dissolution.

Task IV: Mathematical Modeling of nZVI Delivery and Reactivity in DNAPL Source Zones

- Comparison of model simulations and experimental observations confirmed the utility of the trapping number concept for the prediction of the onset, rate, and extent of NAPL mobilization. These comparisons provide the first careful validation of the trapping number in a two- (or three) dimensional system and support the use of this approach for *a priori* predictions of DNAPL mobilization during nZVI injection.

- Application of the traditional clean bed filtration theory (CFT) failed to match observed breakthrough curves from the emulsion injection experiments. However, a modified CFT model, incorporating an additional attachment process represented by a (equilibrium) Langmuir adsorption term, was able to fit the rise, plateau, and tailing of all emulsion breakthrough curves. Based upon the fitted parameter values, the emulsion attachment rate parameter is a function of the surfactant concentration in the formulation, with a smaller value associated with a higher surfactant concentration. The fitted Langmuir isotherm parameters were consistent across experiments. Observed pressure drops in the experiments were demonstrated to be associated with changes in emulsion viscosity.

- RNIP column experiment retention data were also successfully fit to a CFT model (with a constant, irreversible attachment rate). Calculation of the single collector efficiency for these experiments suggested that sedimentation was the main process controlling RNIP transport in these porous media, presumably due to the high specific gravity of the iron particles. Use of the experimentally-validated CFT model to compare emulsion, RNIP, and Z-Loy mobility suggests that RNIP and Z-Loy will only be transported on the order of centimeters to tens of centimeters in fine to medium sand, while emulsion transport distances may rang up to hundreds of meters.

- A hybrid numerical simulator adequately captured the observed PCE dissolution rates and RNIP-mediated transformation within PCE-DNAPL source zone at residual saturation. A modified Damkohler number framework was proposed to predict transformation efficiency under different flow and emplacement conditions.

- Model sensitivity studies revealed that treatment effectiveness was strongly dependent upon the flow rate and initial PCE-DNAPL mass. An increase in flow rate (column residence time) enhanced PCE transformation. The spatial distribution of nZVI emplacement was found to significantly influence PCE transformation efficiency; when the same mass of nZVI was located immediately down-gradient of the DNAPL source zone, PCE transformation efficiency increased by more than 50%.

- Preliminary field scale modeling results suggest that the efficiency of nZVI for DNAPL source zone remediation will be limited by interphase mass transfer processes (i.e., dissolution), if the reduction reaction only occurs in the aqueous phase.

Implications

- The research undertaken in this project demonstrated and quantified many processes that will tend to limit the effectiveness of aqueous slurry nZVI injection for DNAPL source zone treatment under conditions represenative of field scenarios. Although nZVI delivery and transformation of entrapped DNAPL was demonstrated in one dimensional, well-controlled laboratory experiments, extrapolation to field conditions suggests that such injection technologies will fail at this larger scale. In the field, nZVI mass delivery will likely be severely limited by such processes as particle aggregation and consequent pore clogging and hydrogen production. - In multi-dimensional systems, viscosity variations, hydrogen evolution, and pore clogging were shown to lead to flow bypassing around the injected material. These observations imply that any upstream contamination will tend to by-pass the treatment zone, further limiting treatment effectiveness. Although quantifiable, injection of these aqueous slurries can also lead to spreading (mobilization) of the DNAPL contaminant mass to previously uncontaminated areas.

- Transformation of PCE- or TCE-(?)DNAPL to ethene and ethane was demonstrated in one dimensional sand column experiments for a number of commercially available nZVI systems. However, measured reaction rates are such that unrealistically high mass loadings would be required for complete DNAPL transformation within the source zone region. In the absence of such mass loadings, substantial contaminant mass will migrate

beyond the treatment zone and reach down-gradient receptors. Furthermore, even if in source mass emplacement were successful at sufficiently large nZVI loadings, this research suggests that transformation of the DNAPL will be controlled by dissolution, resulting in treatment times on the order of decades or longer

- This research demonstrated that delivery characteristics can be substantially improved, if the nZVI particles are stabilized with a surfactant or encapsulated in an emulsion. A number of emulsion formulations produced in this research were shown to be stable and capable of transporting high nZVI mass loadings large distances in the subsurface. The process of emulsification or surfactant stabilization, however, tended to reduce chloroethene transformation rates in the aqueous phase. Furthermore, when surfactant-stabilized or emulsified formulations are injected into a source zone, substantial DNAPL mass was removed by dissolution (or solubilization) and carried downgradient. In any field application of this technology, this would necessitate fluid capture and treatment.

Recommendations for Future Work

- A model sensitivity analysis conducted in this research suggested that injected RNIP mass may be more effective *in situ* if it is placed immediately downstream of the DNAPL source zone. Thus, further research should be conducted to explore the potential use of RNIP injection as a barrier technology.

- The research results presented here suggest that emulsification and injection of nZVI may offer promise as a secondary treatment technology or 'polishing step', once the bulk of the DNAPL mass has been removed by more aggressive treatment technologies. It is likely that the biodegradable formulations and co-generation of hydrogen associated with the nZVI systems would act to stimulate *in situ* microbial activity, creating a synergy between chemical and biological transformation processes. Further research will be required to explore this hypothesis.

- The research demonstrated that DNAPL dissolution will limit the extent and rate of DNAPL transformation by nZVI as long as the reaction proceeds in the aqueous phase. On the other hand, reaction rates within the DNAPL phase were found to be limited by the solubility of water. These results suggest that future research should explore the possibility of engineering reactions *in situ* which could modify DNAPL composition, acting to maximize the effectiveness of the iron particles.

- The GA emulsion developed in this work is the most promising in terms of its stability and ability to transport large nZVI loadings. Future research should be conducted to explore the transport and reactivity behavior of this emulsion formulation in larger scale systems.

V. Literature Cited

Abriola, L.M., Lang, J., and Rathfelder, K. (1997). *Michigan Soil Vapor Extraction Remediation (MISER) Model: A Computer Program to Model Soil Vapor Extraction and Bioventing of Organic Chemicals in Unsaturated Geological Material* (US-EPA Publication Ref. 600/R-97/099). Cincinnati, OH: Environmental Protection Agency.

Adamson, A.W., and Gast, A.P. (1997). *Physical Chemistry of Surfaces.* New York, NY: Wiley Interscience.

Alessi, D., and Li, Z. (2001). Synergistic effect of cationic surfactants on perchloroethylene degradation by zero-valent iron. *Environmental Science and Technology*, 35, 3713-3717.

Arnold, W.A., Roberts, A.L. (2000). Pathways and kinetics of chlorinated ethylene and chlorinated acetylene reaction with Fe(O) particles. *Environmental Science and Technology,* 34, 1794–1805.

Bashtovoy, V.G., Berkovsky, B.M., and Vislovich, A.N. (1987). *Introduction to Thermomechanics of Magnetic Fluids*. New York: Hemisphere Publishing Corporation.

Becher, P. (2001). *Emulsions: theory and practice.* Washington D.C.: Krieger.

Berge, N.D., and Ramsburg, C.A. (2009). Oil-in-water emulsions for encapsulated delivery of reactive iron particles. *Environmental Science and Technology,* 43(13), 5060-5066.

Berge, N.D., and Ramsburg, C.A. (2010). Iron-Mediated Trichloroethene Reduction within Non-Aqueous Phase Liquid. *Journal of Contaminant Hydrology,* 118(3-4), 105-116.

Berkowitz, B., and Scher, H. (2001). The role of probabilistic approaches to transport theory in heterogeneous media. *Transport in Porous Media,* 42(1-2), 241-263.

Binks, B.P., and Fletcher, P.D.I. (2001). Particles adsorbed at the oil-water interface: A theoretical comparison between spheres of uniform wettability and "Janus" particles. *Langmuir*, 17, 4708-4710.

Borden, R.C. (2007). Effective distribution of emulsified edible oil for enhanced anaerobic bioremediation. *Journal of Contaminant Hydrology*, 94, 1-12.

Burdine, N.T. (1953). Relative Permeability Calculations From Pore Size Distribution Data. *Transactions Of The American Institute Of Mining And Metallurgical Engineers,* 198, 71-78.

Burris, D.R., Delcomyn, C.A., Deng, B., Buck, L.E., and Hatfield, K. (1998). Kinetics of tetrachloroethylene-reductive dechlorination catalyzed by vitamin B. *Environmental Toxicology and Chemistry,* 17(9), 1681-1688.

Chiao, F.F., Currie, R.C., and McKone, T.E. (1994). *Intermedia transfer factors for contaminants found at hazardous waste sites: Tetrachloroethylene (PCE).* California Department of Toxic Substances Control, available at: http://www.dtsc.ca.gov/AssessingRisk/Upload/pce.pdf.

Cho, J., and Annable, M.D. (2005). Characterization of pore scale NAPL morphology in homogeneous sands as a function of grain size and NAPL dissolution. *Chemosphere*, 61, 899-908.

Clausen, C.M., Filipek, L.B., Geiger, C.L., and Clausen, C.A. (2002). Kinetic studies of nanoscale and microscale zero valent iron emulsions. *American Chemical Society, Division of Environmental Chemistry, Preprints of Extended Abstracts 223rd National Meeting*, 42(1), 62-66.

Cortis, A., and Ghezzehei, T.A. (2007). On the transport of emulsions in porous media. *Journal of Colloid and Interface Science,* 313(1), 1-4.

Cortis, A., Harter, T., Hou, L.L., Atwill, E.R., Packman, A.I., and Green, P.G. (2006). Transport of Cryptosporidium parvum in porous media: Long-term elution experiments and continuous time random walk filtration modeling. *Water Resources Research,* 42(12).

Coulibaly, K.M., and Borden, R.C. (2004). Impact of edible oil injection on the permeability of aquifer sands. *Journal of Contaminant Hydrology*, 71, 219-237.

Coulibaly, K.M., Long, C.M., and Borden, R.C. (2006). Transport of edible oil emulsions in clayey sands: One-dimensional column results and model development. *Journal of Hydrologic Engineering,* 11(3), 230-237.

Crocker, J.J., Berge, N.D., and Ramsburg, C.A. (2008). Encapsulated delivery of reactive iron particles using oil-in-water emulsions. *Groundwater Quality 2007 Conference Proceedings,* Fremantle, Western Australia, December 2-6, 2007.

Cundy, A.B., Hopkinson, L., and Whitby, R.L.D. (2008). Use of iron-based technologies in contaminated land and groundwater remediation: A review. *Science of the Total Environment*, 400, 42-51.

Damodaran, S. (2005). Protein stabilization of emulsions and foams. *Journal of Food Science,* 70, R54-R66.

Demond, A.H., and Lindner, A.S. (1993). Estimation of Interfacial-Tension between Organic Liquids and Water. *Environmental Science and Technology,* 27(12), 2318-2331.

Denkov, N.D., Petsev, D.N., and Danov, K.D. (1995). Flocculation of deformable emulsion droplets: I. droplet shape and line tension effects. *Journal of Colloid and Interface Science*, 176, 189-200.

Derjaguin, B.V. (1989). *Theory of Stability of Colloids and Thin Films*. New York, NY: Consultants Bureau.

Dickinson, E., Galazka, V.B., and Anderson, D.M.W. (1991). Emulsifying behaviour of gum arabic. Part 2: Effect of the gum molecular weight on the emulsion droplet-size distribution. *Carbohydrate Polymers,* 14, 385-392.

Dickinson, E. (2003). Hydrocolloids at interfaces and the influence on the properties of dispersed systems. *Food Hydrocolloids, 17(1),* 25-39.

Doong, R., and Lai, Y. (2005). Dechlorination of tetrachloroethylene by palladized iron in the presence of humic acid. *Water Research,* 39, 2309-2318.

Doong, R., and Lai, Y. (2006). Effect of metal ions and humic acid on the dechlorination of tetrachloroethylene by zerovalent iron. *Chemosphere*, 64, 371-378.

Dries, J., Bastiaens, L., Springael, D., Agathos, S.N., and Diels, L. (2004). Competition for Sorption and Degradation of Chlorinated Ethenes in Batch Zero-Valent Iron Systems. *Environmental Science and Technology,* 38, 2879-2884.

Elliot, D.W., and Zhang, W. (2001). Field Assessment of Nanoscale Bimetallic Particles for Groundwater Treatment. *Environmental Science and Technology,* 35, 4922-4926.

Fernandez, P., Andre, V., Rieger, J., and Kuhnle, A. (2004). Nano-emulsion formation by emulsion phase inversion. *Colloids and Surfaces A: Physiochem. Eng. Aspects,* 251(1-3), 53-58.

Fu, J., Li, B., and Wang, Z. (1986). Estimation of fluid-fluid interfacial tensions of multicomponent mixtures. *Chemical Engineering Science,* 41, 2673-2679.

Garrido, N.M., Queimada, A.J., Jorge, M., Macedo, E.A., and Economou, I.G. (2009). 1-octanol/water partition coefficients of n-alkanes from molecular simulations of absolute solvation free energies. *Journal of Chemical Theory and Computation*, 5, 2436-2446.

Geiger, C.L., Clausen, C.A., Brooks, K., Coon, C., Huntley, C., Filipek, L., DeVor, R., Krug, T., O'Hara, S., Major, D., and Quinn, J. (2003). Remediation of DNAPLs using emulsified zero-valent iron: laboratory and field results. *American Chemical Society, Division of Environmental Chemistry, Preprints of Extended Abstracts 225rd National Meeting*, 43(1), 939-944.

Gossett, J.M. (1987). Measurement of Henry's law constants for C1 and C2 chlorinated hydrocarbons. *Environmental Science and Technology*, 21, 202-208.

Gunstone, F.D. (2004). *The Chemistry of Oils and Fats--Sources, Composition, Properties and Uses*. Florida: Blackwell Publishing Ltd.

Henn, K.W., and Waddill, D.W. (2006). Utilization of Nanoscale Zero-Valent Iron for Source Remediation - A case study. *Remediation Journal,* 16, 16706-16707.

Holland, P.M., and Rubingh, D.N. (1992). *Mixed surfactant systems*. Washington, D.C.: American Chemical Society.

Imhoff, P.T., and Miller, C.T. (1997). Dissolution fingering during the solubilization of nonaqueous phase liquids in saturated porous media 1. *Water Resources Research,* 33(9), 2205-2205.

Ivanov, I.B., Danov, K.D., and Kralchevsky, P.A. (1999). Flocculation and coalescence of micron-size emulsion droplets. *Colloids and Surfaces A*, 152, 161-182.

Jawitz, J.W., Sillan, R.K., Annable, M.D., Rao, P.S.C., and Warner, K. (2000). In-situ alcohol flushing of a DNAPL source zone at a dry cleaner site. *Environmental Science and Technology,* 34(17), 3722–3729.

Johnson, T.L., Scherer, M.M., and Tratnyek, P.G. (1996). Kinetics of halogenated organic compound degradation by iron metal. *Environ. Science and Technology*, 30, 2634-2640.

Kaye, G.W.C., and Laby, T.H. (1995). *Tables of physical and chemical* constants (16th Edition). Longman: London.

Kibbey, T.C.G., Ramsburg, C.A., and Pennell, K.D., 2002. Implications of alcohol partitioning behavior for the in situ density modification of entrapped dense nonaqueous phase liquids. *Environmental Science and Technology,* 36, 104–111.

Kim, H., Hong, H., Lee, Y., Shin, H., and Yang, J. (2008). Degradation of Trichloroethylene by Zero-Valent Iron Immobilized in Cationic Exchange Membrane. *Desalination,* 223, 212-220.

Kirschling, T.L., Gregory, K.B., Minkley, E.G., Lowry, G.V., and Tilton, R.D. (2010). Impact of nanoscale zero valent iron on geochemistry and microbial populations in trichloroethylene contaminated aquifer materials. *Environmental Science and Technology*, 44, 3474-3480.

Klokkenburg, M., Vonk, C., Claesson, E.M., Meeldijk, J.D., Erne, B.H. and Philipse, A.P. (2004). Direct Imaging of zero-field dipolar structures in colloidal dispersions of synthetic magnetite. *Journal of the American Chemical Society,* 126(51), 16706-16707.

Köber, R., Schlicker, O., Ebert, M., and Dahmke, A. (2002). Degradation of chlorinated ethylenes by Fe0: inhibition processes and mineral precipitation. *Environmental Geology*, 41, 644-652.

Kralchevsky, P.A., and Nagayama, K. (2000). Capillary interactions between particles bound to interfaces, liquid films and biomembranes. *Advances in Colloid and Interface Science*, 85, 145-192.

Kunkel, R., Wendland, F. (1997). WEKU - a GIS-supported stochastic model of groundwater residence times in upper aquifers for the supraregional groundwater management. *Environmental Geology*, 30, 1-9.

Li, Z., Jones, H.K., Bowman, R.S., and Helferich, R. (1999). Enhanced reduction of chromate and PCE by palletized surfactant-modified zeolite/zerovalent iron. *Environmental Science and Technology*, 33, 4326-4330.

Li, T., and Farrell. J. (2000). Reductive dechlorination of trichloroethene and carbon tetrachloride using iron and palladized-iron cathodes. *Environmental Science and Technology*, 34, 173-179.

Li, Y., Abriola, L., Phelan, T.J., Ramsburg, C.A., and Pennell, K. (2007). Experimental and numerical validation of the total trapping number for prediction of DNAPL mobilization. Environmental Science and Technology, 41, 8135-8141.

Lide, D.R. (2008). *Handbook of Chemistry and Physics* (88th Edition). Boca Raton, FL: CRC Press.

Lien, H.L. and Zhang, W.X. (2001). Nanoscale Iron Particles for Complete Reduction of Chlorinated Ethenes. *Colloids Surfaces A: Physicochemical Engineering Aspects,* 191(1-2), 97-105.

Lien, H.L., Zhang, W.X., (2007). Nanoscale Pd/Fe bimetallic particles: catalytic effects of palladium on hydrodechlorination. *Applied Catalysis B: Environmental,* 77, 110–116.

Lin, C.J., and Lo, S.L. (2005). Effects of iron surface pretreatment on sorption and reduction kinetics of trichloroethylene in a closed batch system. *Water Resources.,* 39(6), 1037-46.

Liu, Y.Q., Choi, H., Dionysiou, D., and Lowry, G.V. (2005). Trichloroethene hydrodechlorination in water by highly disordered monometallic nanoiron. *Chemistry of Materials,* 17(21), 5315-5322.

Liu, Y., and Lowry, G.V. (2006). Effect of Particle Age (Fe0 Content) and Solution pH on nZVI reactivity: H2 Evolution and TCE dechlorination. *Environmental Science and Technology,* 40(19), 6085-6090.

Liu, Y., Phenrat, T., and Lowry, G.V. (2007). Effect of TCE concentration and dissolved groundwater solutes on nZVI-promoted TCE dechlorination and H2 evolution. *Environmental Science and Technology,* 41(22), 7881-7887.

Loraine, G.A. (2001). Effects of alcohols, anionic and nonionic surfactants on the reduction of PCE and TCE by zero-valent iron. *Water Resources*, 35, 1453-1460.

Lowry, G.V., and Reinhard, M. (2000). Pd-catalyzed TCE dechlorination in groundwater: Solute effects, biological control and oxidative catalyst regeneration. *Environmental Science and Technology*, 34, 3217-3223.

Lowry, G.V. (2004). Nanoscale ZVI for DNAPL source zone treatment: targeted delivery and iron longevity. *SERDP/ESTCP Partners in Environmental Technology Technical Symposium & Workshop*, Technical Session No. 4A.

Lunn, S.R.D., and Kueper, B.H. (1999). Manipulation of density and viscosity for the optimization of DNAPL recovery by alcohol flooding. *Journal of Contaminant Hydrology,* 38(4), 427–445.

Martel, K.E., Martel, R., Lefebvre, R., and Gélinas, P.J. (1998). Laboratory study of solutions used for mobility control during in situ NAPL recovery. *Ground Water Monitoring and Remediation,* 18(3), 103–113.

Matheson, L.J., and Tratnyek, P.G. (1994). Reductive Dehalogenation of Chlorinated Methanes by Iron Metal. *Environmental Science and Technology,* 28, 2045-2053.

Mayer, A.S., Zhong, L.R., and Pope, G.A. (1999). Measurement of mass-transfer rates for surfactant-enhanced solubilization of nonaqueous phase liquids. *Environmental Science and Technology,* 33(17), 2965-2972.

Meyer, D.E., Hampson, S., Ormsbee, L., and Bhattacharyya, D. (2009). A study of groundwater matrix effects on the destruction of trichloroethylene using Fe/Pd nanoaggegates. *Environmental Progress and Sustainable Energy,* 28(4), 507–518.

Mualem, Y. (1976). New Model For Predicting Hydraulic Conductivity Of Unsaturated Porous-Media. *Water Resources Research,* 12(3), 513-522.

Nakauma, M., Funami, T., Noda, S., Ishihara, S., Al-Assaf, S., Nishinari, K., and Phillips, G.O. (2008). Comparison of sugar beet pectin, soybean soluble polysaccharide, and gum arabic as food S19 emulsifiers. 1. Effect of concentration, pH, and salts on the emulsifying properties. *Food Hydrocolloids*, 22, 1254-1267.

Nurmi, J.T., Tratnyek, P.G., Sarathy, V., Baer, D.R., Amonette, J.E., Pecher, K.H., Wang, C., Linehan, J.C., Matson, D.W., Penn, R.L., and Driessen, M.D. (2005). Characterization and Properties of Metallic Iron Nanoparticles: Spectroscopy, Electrochemistry, and Kinetics. *Environmental Science and Technology,* 39, 1221-1230.

Okuda, I., McBride, J.F., Gleyzer, S.N., and Miller, C.T. (1996). Physicochemical transport processes affecting the removal of residual DNAPL by nonionic surfactant solutions. *Environmental Science and Technology*, 30, 1852–1860.

Orth, W.S., and Gillham, R.W. (1996). Dechlorination of Trichloroethene in Aqueous Solution Using Fe(0). *Environmental Science and Technology,* 30(1), 66-71.

Pennell, K.D., Abriola, L.M., and Weber, W.J. (1993). Surfactant-enchanced solubilization of residual dodecane in soil columns. 1 Experimental Investigation. *Environmental Science and Technology,* 27(12), 2332-2340.

Pennell, K.D., Jin, M., Abriola, L.M., and Pope, G.A. (1994). Surfactant enhanced remediation of soil columns contaminated by residual tetrachloroethylene. *Journal of Contaminant Hydrology*, 16, 35-53.

Pennell, K.D., Pope, G.A., and Abriola, L.M. (1996). Influence of viscous and buoyancy forces on the mobilization of residual tetrachloroethylene during surfactant flushing. *Environmental Science and Technology,* 30(4), 1328-1335.

Petsev, D.N., Denkov, N.D., and Kralchevsky, P.A. (1995). Flocculation of deformable emulsion droplets: II. interaction energy. *Journal of Colloid and Interface Science,* 176(1), 201-213.

Phelan, T.J. (2004). Subsurface Compositional Simulation Incorporating Solute-Chemistry Dependent Interfacial Properties. (Doctoral Dissertation). University of Michigan, Ann Arbor, MI.

Phenrat, T., Saleh, N., Sirk, K., Tilton, R.D., and Lowry, G.V. (2007). Aggregation and Sedimentation of Aqueous Nanoscale Zerovalent Iron Dispersions. *Environmental Science and Technology,* 41(1), 284-290.

Phenrat, T., Saleh, N., Sirk, K., Kim, H.J., Tilton, R.D., and Lowry, G.V. (2008). Stabilization of aqueous nanoscale zerovalent iron dispersions by anionic polyelectrolytes: adsorbed

anionic polyelectrolyte layer properties and their effect on aggregation and sedimentation. *Journal of Nanoparticle Research*, 10, 795–814.

Phenrat, T., Liu, Y.Q., Tilton, R.D., and Lowry, G.V. (2009). Adsorbed polyelectrolyte coatings decrease Fe(O) nanoparticle reactivity with TCE in water: conceptual model and mechanisms. *Environmental Science and Technology*, 43, 1507-1514.

Popplewell, J., Rosensweig, R.E., and Siller, J.K. (1995). Magnetorheology of ferrofluid composites. *Journal of Magnetism and Magnetic Materials*. 149(1-2), 53-56.

Powers, S. E. (1992). Dissolution of nonaqueous phase liquids in saturated subsurface systems. (Doctoral Dissertation). University of Michigan, Ann Arbor, MI.

Powers, S.E., Abriola, L.M., and Weber, W.J. (1994). An experimental investigation of non-aqueous phase liquid dissolution in saturated subsurface systems: Transient mass transfer rates. *Water Resources Research*, 30, 321-332.

Qin, S.X., Huang, G.H., Chakma, A., Chen, B., and Zeng, G.M. (2007). Simulation-based process optimization for surfactant-enhanced aquifer remediation at heterogeneous DNAPL contaminated sites. *Science for the Total Environment*, 381, 17-37.

Quinn, J., O'Hara, S., Krug, T., Geiger, C., and Clausen, C. (2004). Evaluating the distribution of emulsified zero-valent iron for four different injection techniques. In Gavaskar, A.R. and Chen, A.S.C. (Eds.), *Proceedings of the Fourth International Conference on Remediation of Chlorinated and Recalcitrant Compounds* (Paper 5B-08).

Quinn, J., Geiger, C., Clausen, C., Brooks, K., Coon, C., O'Hara, S., Krug, T., Major, D., Yoon, W., Gavaskar, A., and Holdsworth, T. (2005). Field demonstration of dDNAPL dehalogenation using emulsified zero-valent iron. *Environmental Science and Technology,* 39(5), 1309-1318.

Ramsburg, C.A., and Pennell, K.D. (2002). Density-Modified Displacement for DNAPL Source Zone Remediation: Density Conversion and Recovery in Heterogeneous Aquifer Cells. *Environmental Science and Technology,* 36(14), 3176-3187.

Ramsburg, C.A., Pennell, K.D., Kibbey, T.C.G., and Hayes, K.F. (2003). Use of a surfactant-stabilized emulsion to deliver n-butanol for density modified displacement of trichloroethene-NAPL. *Environmental Science and Technology*, 37, 4246-4253.

Ramsburg, C.A., Abriola, L.M., Pennell, K.D., Löffler, F.E., Gamache, M., Amos, B.K., and Petrovskis, E.A. (2004). Stimulated Microbial Reductive Dechlorination following Surfactant Treatment at the Bachman Road Site. *Environmental Science and Technology,* 38(22), 5902-5914.

Range, G.M., and Klapp, S.H.L. (2005). Density-functional study of model bidisperse ferrocolloids in an external magnetic field. *Journal of Chemical Physics,* 122(22), 6.

Roeder, E., Brame, S.E., and Falta, R.W. (1996). Swelling of DNAPL by cosolvent flooding to allow its removal as an LNAPL. In Reddi, L.N. (Ed.), *Non-Aqueous Phase Liquids (NAPLs) in Subsurface Environment: Assessment and Remediation*. New York: ASCE.

Ruiz, N.S., Seal, J., and Reinhart, D. (2000). Surface chemical reactivity in selected zero-valent iron samples used in groundwater remediation. *Journal of Hazardous Materials*, B80, 107-117.

Saleh, N., Phenrat, T., Sirk, K., Dufour, B., Ok, J., Sarbu, T., Matyiaszewski, K., Tilton, R.D., and Lowry, G.V. (2005a). Adsorbed triblock copolymers deliver reactive iron nanoparticles to the oil/water interface. *Nano Letters 5,* (12), 2489–2494.

Saleh, N., Sarbu, T., Sirk, K., Lowry, G.V., Matyjaszewski, K., Tilton, R.D. (2005b). Oil-in-water emulsions stabilized by highly charged polyelectrolytegrafted silica nanoparticles. Langmuir 21 (22), 9873–9878.

Salou, M., Siffert, B., Jada, A. (1998). Study of the stability of bitumen emulsions by application of DLVO theory. *Colloids Surfaces A*, 142, 9-16.

Sangster, J. (1997). Octanol-Water Partition Coefficients: Fundamentals and Physical Chemistry. New York, NY: Wiley.

Schreier, C.G., and Reinhard, M. (1994). Transformation of Chlorinated Organic Compounds by Iron and Manganese Powders in Buffered Water and in Landfill Leachate. *Chemosphere,* 29, 1743-1753.

Schrick, B., Blough, J.L., Jones, A.D., and Mallouk, T.E. (2002). Hydrochlorination of Trichloroethylene to Hydrocarbons using Bimetallic Nickel-Iron Nanoparticles. *Chemical Materials,* 14, 5140-5147.

Schrick, B., Hydutsky, B.W., Blough, J.L., and Mallouk, T.E. (2004). Delivery vehicles for zerovalent metal nanoparticles in soil and groundwater. *Chemical Materials,* 16, 2187-2193.

Shin, H., Choi, H., Kim, D., and Baek, K. (2008). Effect of Surfactant on Reductive Dechlorination of Trichloroethylene by Zero-Valent Iron. *Desalination,* 223, 299-307.

Song, H., and Carraway, E.R. (2008). Catalytic hydrodechlorination of chlorinated ethenes by nanoscale zero-valent iron. *Applied Catalysis B*, 78, 53-60.

Soo, H., and Radke, C.J. (1985). Flow of dilute, stable liquid and solid dispersions in underground porous-media. *Aiche Journal,* 31(11), 1926-1928.

Su, C., and Puls, R.W. (1999). Kinetics of trichloroethene reduction by zerovalent iron and tin: Pretreatment effect, apparent activation energy, and intermediate products. *Environmental Science and Technology*, 33, 163-168.

Suchomel, E.J., Ramsburg, C.A., and Pennell, K.D. (2007). Evaluation of trichloroethene recovery processes in heterogeneous aquifer cells flushed with biodegradable surfactants. *Journal of Contaminant Hydrology*, 94, 195-214.

Taghavy, A., Costanza, J., Pennell, K.D., and Abriola, L.M. (2010). Effectiveness of nanoscale zero-valent iron for treatment of a PCE-DNAPL source zone. *Journal of Contaminant Hydrology,* 118(3-4), 128-142.

Támara, M.L., and Butler, E.C. (2004). Effects of Iron Purity and Groundwater Characteristics on Rates and Products in the Degradation of Carbon Tetrachloride by Iron Metal. *Environmental Science and Technology,* 38(6), 1866–1876.

Tan, C-T. (1998). Beverage flavor emulsion - a form of emulsion liquid membrane microencapsulation. In Contis, E.T., Ho, C.T., Mussinan, C.J., Parliment, T.H., Shahidi, F., and Spanier, A.M. (Eds.), *Food Flavors: Formation, Analysis, and Packaging Influences (*Vol. 40, 29-42*).* Amsterdam, The Netherlands: Elsevier.

Taylor, T.P., Pennell, K.D., Abriola, L.M., and Dane, J.H. (2001). Surfactant enhanced recovery of tetrachloroethylene from a porous medium containing low permeability lenses - 1. Experimental studies. *Journal Of Contaminant Hydrology,* 48(3-4), 325-350.

Taylor, T.P., Rathfelder, K.M., Pennell, K.D., Abriola, L.M. (2004). Effects of ethanol addition on micellar solubilization and plume migration during surfactant enhanced recovery of tetrachloroethene. *Journal of Contaminant Hydrology*, 69, 73-99.

Tee, H.T., Grulke, E., and Bhattacharyya, D. (2005). Role of Ni/Fe nanoparticle composition on the degradation of trichloroethylene from water. *Industrial and Engineering Chemistry Research,* 44, 7062–7070.

Tratnyek, P.G., Scherer, M.M., Deng, B., and Hu, S. (2001). Effects of natural organic matter, anthropogenic surfactants, and model quinones on the reduction of contaminants by zero-valent iron. *Water Resources Research,* 18, 4435–4443.

Van Genuchten, M.T. (1980). A Closed-Form Equation For Predicting The Hydraulic Conductivity Of Unsaturated Soils. *Soil Science Society Of America Journal,* 44(5), 892-898.

Vincent, B., Edwards, J., Emmett, S., and Jones, A. (1986). Depletion flocculation in dispersions of sterically-stabilized particles (soft spheres). *Colloids Surfaces*, 18, 261-281.

Voillier, E., Inglett, P.W., Hunter, K., Roychoudhury, A.N., and Van Cappellen, P. (2000). The Ferrozine Method Revisited: Fe(II)/Fe(III) determination in natural waters. *Applied Geochemistry,* 15, 785-790.

Wang, J., and Farrell, J. (2003). Investigating the role of atomic hydrogen on chloroethene reactions with iron using Tafel analysis and electrochemical impedance spectroscopy. *Environmental Science and Technology*, 37, 3891-3896.

Wang, W., Zhou, M., Jin, Z., and Li, T. (2010). Reactivity characteristics of poly(methyl methacrylate) coated nanoscale iron particles for trichloroethylene remediation. *Journal of Hazardous Materials,* 173, 724-730.

Wang, C.B., and Zhang, W.X. (1997). Synthesizing nanoscale iron particles for rapid and complete dechlorination of TCE and PCBs. *Environmental Science and Technoogy*, 31, 2154-2156.

Wilkin, R.T., Puls, R.W., and Sewell, G.W. (2003). Long-term performance of permeable reactive barriers using zero-valent iron: Geochemical and microbiological effects. *Ground Water*, 41, 493-503.

Willson, C.S., Hall, J.L., Miller, C.T., and Imhoff, P.T. (1999). Factors affecting bank formation during surfactant-enhanced mobilization of residual NAPL. *Environmental Science and Technology,* 33(14), 2440-2446.

Xiu, Z., Jin, Z., Li, T., Mahendra, S., Lowry, G.V., and Alvarez, P.J.J. (2010). Effects of nano-scale zero-valent iron particles on a mixed culture dechlorinating trichloroethylene. *Bioresource Technology*, 101, 1141-1146.

Yan, L., Thompson, K.E., Valsaraj, K.T., and Reible, D.D. (2003). In-situ control of DNAPL density using polyaphrons. *Environmental Science and Technology*, 37, 4487-4493.

Zhan, J., Sunkara, B., Lynn, L., John, V.T., He, J., McPherson, G.L., Piringer, G. and Lu, Y. (2009). Multifunctional colloidal particles for in-situ remediation of chlorinated hydrocarbons. *Environmental Engineering Science,* 43, 8616-8621.

Zhang, P., Tao, X., Li, Z., and Bowman, R.S. (2002). Enhanced perchloroethylene reduction in column systems using surfactant-modified zeolite/zero-valent iron pellets. *Environmental Science and Technology*, 36, 3597-3603.

Zhang, W. (2003). Nanoscale iron particles for environmental remediation: An overview. *Journal of Nanoparticle Research*, 5, 323-332.

VI. Appendices

Appendix B

Articles in Peer-Reviewed Journals

Berge, N.D., and Ramsburg, C.A. (2009). Oil-in-water emulsions for encapsulated delivery of reactive iron particles. *Environmental Science and Technology*, 43(13), 5060-5066.

Berge, N.D., and Ramsburg, C.A. (2010). Iron-Mediated Trichloroethene Reduction within Non-Aqueous Phase Liquid. *Journal of Contaminant Hydrology*, 118(3-4), 105-116.

Crocker, J.J., Berge, N.D., and Ramsburg, C.A. (2008). Encapsulated Delivery of Reactive Iron Particles using Oil-in-Water Emulsions. In Trefrey, M.G. (Ed.), *GQ07: Securing Groundwater Quality in Urban and Industrial Environments*, IAHS Publication No. 324, 242-249.

Li, Y., Abriola, L.M., Phelan, T.J., Ramsburg, C.A., and Pennell, K.D. (2007). Experimental and Numerical Validation of the Total Trapping Number for Prediction of Entrapped DNAPL Mobilization. *Environmental Science and Technology*, 41(23), 8135-8141.

Long, T. and C.A. Ramsburg. (2011). Encapsulation of nZVI Particles Using a Gum Arabic Stabilized Oil-in-Water Emulsion. *Journal of Hazardous Materials*, *in press*, doi:10.1016/j.jhazmat.2011.02.084

Taghavy, A., Costanza, J., Pennell, K.D., and Abriola, L.M. (2010). Effectiveness of Nano-scale Zero-valent Iron for Treatment of a PCE-DNAPL Source Zone. *Journal of Contaminant Hydrology*, 118, 128-142.

Conference or Symposium Abstracts

Abriola, L.M., Pennell, K.D., Ramsburg, C.A., Berge, N.D., Costanza, J., Li, Y. and Taghavy, A. (2007). Delivery of reactive iron particles for treatment of DNAPL source zones. *SERDP/ESTCP Partners in Environmental Technology Technical Symposium & Workshop*, Washington, D.C., December 4 – 6, 2007.

Abriola, L.M., Pennell, K.D., Ramsburg, C.A., Berge, N.D., Costanza, J., and Li, Y. (2008). Assessment of Reactive Iron Particle Delivery Approaches for Treatment of DNAPL Source Zones. *SERDP/ESTCP Partners in Environmental Technology Technical Symposium & Workshop*, Washington, D.C., December 4 – 6, 2008.

Abriola, L.M., Pennell, K.D., Ramsburg, C.A., Chen, M., Costanza, J., Long, T., Kanel, S.R., Taghavy, A., Oyewale, S., and Merriam**,** K.L. (2010). Assessment of Reactive Iron Particle Delivery Approaches for Treatment of DNAPL Source Zones. *SERDP/ESTCP Partners in Environmental Technology Technical Symposium & Workshop*, Washington, D.C., November 30 - December 2, 2010.

Abriola, L.M., Pennell, K.D., Ramsburg, C.A., Chen, M., Long, T., Kanel, Costanza, J., Taghavy, A., Oyewale, S., and Merriam, K.L. (2009). Assessment of reactive iron particle delivery approaches for treatment of DNAPL source zones. *SERDP/ESTCP Partners in Environmental Technology Technical Symposium & Workshop*, Washington, D.C., December 4 – 6, 2009.

Berge, N.D., and Ramsburg, C.A. (2008). Trichloroethene Reduction within a Nonaqueous Phase Liquid using Zero Valent Iron. *American Geophysical Union Fall Meeting*, San Francisco, CA, December 15-19, 2008.

Berge, N.D., Crocker, J.J., and Ramsburg, C.A. (2007). Encapsulated delivery of reactive iron particles for source zone remediation using oil-in-water Emulsions. *Groundwater Quality 2007 Conference,* Fremantle, Western Australia, December 2-6, 2007.

Berge, N.D., Li, Y., Abriola, L.M., and Ramsburg, C.A. (2008). Subsurface Transport of Reactive Iron Particles Encapsulated within Oil-in-Water Emulsions. *American Geophysical Union Joint Assembly*, Fort Lauderdale, FL, May 27-30, 2008.

Berge, N.D., Taghavy, A., and Ramsburg, C.A. (2007). Development and assessment of oil-in-water emulsions for encapsulation of reactive iron particles for subsurface delivery. *American Geophysical Union Fall Meeting*, San Francisco, CA, December 10-14, 2007.

Crocker, J.J., Berge, N.D., and Ramsburg, C.A. (2007). Transport of Oil-in-Water Emulsions Designed to Deliver Reactive Iron Particles in Porous Media. *American Geophysical Union Joint Assembly*, Acapulco, Mexico, May 22-25, 2007.

Kanel, S.R., Costanza, J., and Pennell, K.D. (2009). Catalytic reduction of tetrachloroethene dense non-aqueous phase liquid by different types of reactive iron nano particles. *237th ACS National Meeting & Exposition*, Salt Lake City, UT, March 22-26, 2009.

Taghavy A., Costanza, J., Pennell, K.D., and Abriola, L.M. (2009). Simulating the reactive transport of organic solutes and zero valent iron nano particles in 1-D column experiments. *AGU Fall meeting*, Paper Number: H43B-1018.

Appendix C

Intellectual Property Patents

Ramsburg, C.A. and Berge, N.D. *Iron-mediated Trichloroethene Reduction within Nonaqueous Phase Liquids*. International Application filed 16 December 2009, Serial No. PCT/US2009/068184 Tufts University Office for Technology Licensing and Industry Collaboration.

Long, T. and Ramsburg, C.A. *Gum Arabic Encapsulation of Reactive Particles for Enhanced Delivery during Subsurface Restoration*. United States provisional patent application 07 December 2010, Serial No. 61/420,607, Tufts University Office for Technology Licensing and Industry Collaboration.